UNIVERSITY OF CALIFORNIA SAN DIEGO

Ultrafast magnetic control in a spin-orbit coupled iridate

A dissertation submitted in partial satisfaction of the
requirements for the degree
Doctor of Philosophy

in

Physics

by

Gufeng Zhang

Committee in charge:

Professor Richard Averitt, Chair
Professor Yeshaiahu Fainman
Professor Eric Fullerton
Professor Oleg Shpyrko
Professor Congjun Wu

2020

The dissertation of Gufeng Zhang is approved, and it is acceptable in quality and form for publication on microfilm and electronically:

_____

_____

_____

_____

_____

Chair

University of California San Diego

2020

DEDICATION

To my parents and family.

EPIGRAPH

Let there be light:

and there was light.

TABLE OF CONTENTS

LIST OF FIGURES

LIST OF TABLES

ACKNOWLEDGEMENTS

I still remember the time I first entered UCSD campus in 2013. That was a summer night, cool and refreshing, like in yesterday. Now I have spent more than six years here and almost finished this physics journey. Everything around has been so familiar that I never notice until the time of leaving. Time is never enough to say thank you to everyone who has helped me.

First I would like to thank my advisor, Dr. Richard Averitt, without whom I could never advance my Ph.D. As a physicist, Rick is extremely knowledgeable. I always learnt a lot from him every time we discussed about physics. As a mentor, his hands-off management style gives us a lot of freedom to have ideas by ourselves as a researcher more than a student. We have all been very self-motivated and have ownership of our projects. As a person, Rick is always calm, supportive and encouraging, making the challenging and sometimes suffering Ph.D. life enjoyable.

I would like to thank Dr. Jingdi Zhang, who is both my friend and second mentor. I joined the lab when Jingdi started his posdoc. I learnt almost all the hands-on experimental details from him. His insight and passion to physics always motivate me. We can't pick up techniques so fast and build the new optical lab without him.

I feel fortunate to have worked with my fellow colleges, Kevin, Peter, Dylan and Jacob. We joined the group around the same time, and built everything together from scratch. We built our friendship through helping and supporting each other.

I would like to thank my committee members: Prof. Congjun Wu, Prof. Oleg Shpyrko, Prof. Shaya Fainman, and Prof. Eric Fullerton for supporting my thesis and giving me advice. Special thank to Prof. Wu, my first year advisor, for the guidance to the condensed matter physics.

I am grateful to my parents for their unselfish support through all my life. Although they are ten thousands miles away, they are right near my heart. I couldn't imagine what I will be without them.

I might be the luckiest person in the world to have my wife Chenwen Lin. We met ten

years ago, experienced all the ups and downs in life together and finally got married in the U.S.. Although we were at long-distance relationship most of the time in the U.S., her support is priceless and helped me get through all the obstacles these years. Our 1-year old daughter Luna is the best gift for us and for my Ph.D.

Chapter 4 is about a paper in preparation, discussing about ultrafast magnetic control in Sr_2IrO_4. Authors include Gufeng Zhang, Xiang Chen, Urban F.P. Seifert, Jingdi Zhang, Kevin Cremin, Leon Balents, Stephen D. Wilson and Richard D. Averitt. The thesis author is the primary author of this chapter.

VITA

2012	B. S. in Physics, University of Science and Technology of China
2012-2013	Research Assistant, Fudan University
2013-2015	Graduate Teaching Assistant, University of California San Diego
2015-2020	Graduate Research Assistant, University of California San Diego
2020	Ph. D. in Physics, University of California San Diego

PUBLICATIONS

Xiao-Guang Li, **Gu-Feng Zhang**, Guang-Fen Wu, Hua Chen, Culcer Dimitrie, Zhen-Yu Zhang, "Proximity effects in topological insulator heterostructures", *Chinese Physics B*, 22 (9), 097306, 2013.

Gufeng Zhang, Xiaoguang Li, Guangfen Wu, Jie Wang, Dimitrie Culcer, Efthimios Kaxiras, Zhenyu Zhang "Quantum phase transitions and topological proximity effects in graphene nanoribbon heterostructures", *Nanoscale*, 6 (6), 3259-3267, 2014

Gu-Feng Zhang, Yi Li, Congjun Wu, "Honeycomb lattice with multiorbital structure: Topological and quantum anomalous Hall insulators with large gaps", *Physical Review B*, 90 (7), 075114, 2014

Jingdi Zhang, Xiaoguang Zhao, Kebin Fan, Xiaoning Wang, **Gu-Feng Zhang**, Kun Geng, Xin Zhang, Richard D Averitt, "Terahertz radiation-induced sub-cycle field electron emission across a split-gap dipole antenna", *Applied Physics Letters*, 107 (23), 231101, 2015

Kebin Fan, Jingdi Zhang, Xinyu Liu, **Gu-Feng Zhang**, Richard D Averitt, Willie J Padilla, "Phototunable Dielectric Huygens' Metasurfaces", *Advanced Materials*, 30 (22), 1800278, 2018

A Ron, S Chaudhary, **G Zhang**, H Ning, E Zoghlin, SD Wilson, RD Averitt, G Refael, D Hsieh, "Ultrafast enhancement of ferromagnetic spin exchange induced by ligand-to-metal charge transfer", *arXiv:1910.06376*, 2019

Alexander S McLeod, Jingdi Zhang, MQ Gu, Feng Jin, **G Zhang**, Kirk W Post, XG Zhao, Andrew J Millis, WB Wu, James M Rondinelli, Richard Douglas Averitt, Dimitri N Basov, "Multi-messenger nanoprobes of hidden magnetism in a strained manganite", *Nature materials*, 19 (4), 397-404, 2019

Gu-Feng Zhang, Xiang Chen, Urban F.P. Seifert, Jingdi Zhang, Kevin Cremin, Leon Balents, Stephen D. Wilson, Richard D. Averitt, "Ultrafast magnetic control in a spin-orbit coupled iridate", *in preparation*, 2020

ABSTRACT OF THE DISSERTATION

Ultrafast magnetic control in a spin-orbit coupled iridate

by

Gufeng Zhang

Doctor of Philosophy in Physics

University of California San Diego, 2020

Professor Richard Averitt, Chair

The development of ultrafast spectroscopy gives us access to the time dimension to study the dynamics of condensed matter systems. Different from conventional condensed matter experimental techniques, the pump-probe technique allows us not only to study the relaxation of nonequilibrium to equilibrium states, but also the possibility to selectively control the properties of a material using ultrafast light. In my thesis, I will introduce the fundamental of optics in the first chapter. Second chapter consists of the experimental set-ups I developed and built during my Ph.D.: Terahertz time-domain spectroscopy (THz-TDS), broadband THz source from two-color laser-induced gas plasma, intensive mid-infrared pump Kerr rotation probe and data acquisition (DAQ) system. The third chapter is the background of spin-orbit coupled Mott insulator Sr_2IrO_4,

and the last chapter includes my work of ultrafast magnetic control in Sr_2IrO_4: we study the magnetic dynamics of the $J_{eff} = 1/2$ Mott state using strong mid-Infrared 9 μm (below the charge gap), and near-infrared 1.3 μm (above the charge gap) circularly polarized excitations, and monitor the pump induced Kerr signal. For both pump wavelength, the 2D in-plane B_{2g} coherent magnon oscillation of frequency $\sim$ 0.5 THz was observed in the pump-induced Kerr rotation signal. The circularly polarized 9 μm pumps of opposite helicities excite oscillations of opposite phase, while 1.3 μm pumps excite oscillations of same phase. The quadratically scaling of the fluence dependent magnon amplitude for the 9 μm pump indicates a novel photon-two-magnon coupling mechanism for the magnon generation. The directly excitation (9 μm) of the spin spectrum without photodoping electrons permits extremely efficient magnon generation, almost ten times better than the resonant 1.3 μm pump.

Chapter 1

Optical fundamentals

1.1 Overview

Optical spectroscopy is a powerful experimental technique to study the optical properties of quantum materials [3, 4]. Elementary excitations have various energy scales from terahertz to x-rays that require appropriate wavelength of light to probe. Ultrafast spectroscopy, which is the focus of this thesis, measures the dynamics of optical properties of a material using ultrafast pulsed lasers. An intense pump pulse excites a material to nonequilibrium states, and another probe pulse reaching the material at different time delays detects its relaxation to equilibrium states[1]. It is crucial to access various wavelength of light for both pump and probe pulses to investigate different elementary excitations of interest. Utilizing nonlinear optical process due to the intense peak electric field of a pulsed light, we can convert the fundamental pulses (usually 800 nm for regenerative amplifier laser) to other wavelength.

[1] Relaxation to equilibrium states is not always the destiny of an excited state. Metastable states excited by pulsed lasers in 1T-TaS_2 [5] and strained manganite films [6] have been reported.

1.2 Nonlinear optics

Nonlinear optics is the phenomena that the optical properties of materials are modified by intense light [7]. The first example of nonlinear optics was the discovery of second-harmonic generation [8]. We start with the polarization of a material $P(t)$:

$$P(t) = \varepsilon_0 \chi^{(1)} E(t), \tag{1.1}$$

where $E(t)$ is the applied external electric field, ε_0 is the permittivity of the vacuum, and $\chi^{(1)}$ is the linear susceptibility. For linear optics, the polarization is proportional to the applied field. However, for an intense electric field, Eq. 1.1 can be generalized to:

$$\begin{aligned} P(t) &= \varepsilon_0[\chi^{(1)}E(t) + \chi^{(2)}E^2(t) + \chi^{(3)}E^3(t) + ...] \\ &= P^{(1)}(t) + P^{(2)}(t) + P^{(3)}(t) + ... \end{aligned} \tag{1.2}$$

where $\chi^{(n)}$, $P^{(n)}(t)$ is the nth order nonlinear susceptibility and nth order nonlinear polarization. We note that Eq.(1.2) only applies for a medium that is lossless so the polarization response is instantaneous. We mainly focus on the second-order nonlinear susceptibility $\chi^{(2)}$ that occurs only in noncentrosymmetric crystals.

1.2.1 Second harmonic generation

Assuming a laser pulse with electric field $E(t) = Ee^{-i\omega t} + c.c.$, the polarization response of a material is:

$$\begin{aligned} P^{(2)}(t) &= \varepsilon_0 \chi^{(2)}(t) E^2(t) \\ &= 2\varepsilon_0 \chi^{(2)} EE^* + (\varepsilon_0 \chi^{(2)} E^2 e^{-2i\omega t} + c.c.) \end{aligned} \tag{1.3}$$

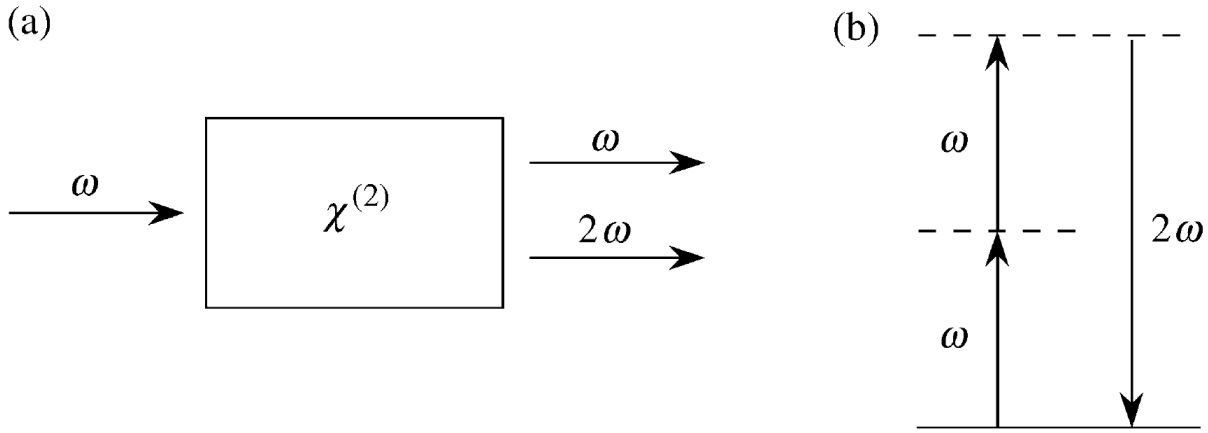

Figure 1.1: From [7]. (a) Diagram of second-harmonic generation. (b) Energy-level diagram of second-harmonic generation.

Eq.(1.3) consists of a zero-frequency term and an electric field of twice the frequency. Fig.(1.1) shows the diagrams of SHG, where a intensive fundamental beam goes through the medium, generating second-harmonic beam. The SHG of 400 nm from fundamental 800 nm laser using β-Barium borate (BBO) is used extensively in a modern ultrafast optics lab.

1.2.2 Sum-, difference-frequency generation and optical rectification

Consider an electric field with two different frequencies:

$$E(t) = E_1\, e^{-i\omega_1 t} + E_2\, e^{-i\omega_2 t} + c.c. \tag{1.4}$$

The second-order nonlinear polarization is:

$$\begin{aligned} P^{(2)}(t) &= \varepsilon_0 \chi^{(2)}(t) E^2(t) \\ &= \varepsilon_0\, \chi^{(2)} [(E_1^2\, e^{-2i\omega_1 t} + E_2^2\, e^{-2i\omega_2 t} + 2E_1 E_2 e^{-i(\omega_1+\omega_2)t} \\ &+ 2E_1 E_2^* e^{-i(\omega_1-\omega_2)t} + c.c.) + 2(|E_1|^2 + |E_2|^2)] \end{aligned} \tag{1.5}$$

One can express Eq.(1.5) in the form of different frequency components:

$$P(2\omega_1) = \varepsilon_0 \chi^{(2)} E_1^2 e^{-2i\omega_1 t} \quad (SHG) \tag{1.6a}$$

$$P(2\omega_2) = \varepsilon_0 \chi^{(2)} E_2^2 e^{-2i\omega_2 t} \quad (SHG) \tag{1.6b}$$

$$P(\omega_1 + \omega_2) = 2\varepsilon_0 \chi^{(2)} E_1 E_2 e^{-i(\omega_1+\omega_2)t} \quad (SFG) \tag{1.6c}$$

$$P(\omega_1 - \omega_2) = 2\varepsilon_0 \chi^{(2)} E_1 E_2^* e^{-i(\omega_1-\omega_2)t} \quad (DFG) \tag{1.6d}$$

$$P(0) = 2\varepsilon_0 \chi^{(2)} (|E_1|^2 + |E_2|^2) \quad (OR) \tag{1.6e}$$

where SFG stands for sum frequency generation, DFG: difference frequency generation, and OR: optical rectification.

DFG is the mechanism of generating mid-infrared light from the frequency difference of near-infrared beams (section 2.4), and optical rectification is crucial for generating terahertz (THz) radiation (section 2.3).

1.2.3 Phase matching

In the case of a second-order nonlinear process involving ω_1, ω_2 and ω_3 light, both energy and momentum conservation need to be satisfied:

$$\omega_3 = \omega_1 + \omega_2 \tag{1.7a}$$

$$\mathbf{k}_3 = \mathbf{k}_1 + \mathbf{k}_2 \tag{1.7b}$$

The momentum conservation condition is sometimes called *phase matching*. Taking the simplest case where all the beams are collinear as an example, Eq.(1.7b) becomes scalar. The

wavevector mismatch is $\Delta k = k_1 + k_2 - k_3$, yielding the phase matching condition:

$$\frac{n_3\omega_3}{c} = \frac{n_2\omega_2}{c} + \frac{n_1\omega_1}{c} \tag{1.8}$$

This gives $n_3 = (n_1\omega_1 + n_2\omega_2)/\omega_3$. It is easy to show that for normal dispersion (where n increases monotonically with ω), Eq.(1.7a) and Eq.(1.8) cannot be fulfilled at the same time. However, the use of birefringent materials can solve this problem. Birefringence is where the refractive index depends on the polarization of the beam. The classification of type I and type II in uniaxial crystals is summarized in Table (1.2.3).

	Positive uniaxial ($n_e > n_o$)	Negative uniaxial ($n_e < n_o$)
Type I	$n_3^o\omega_3 = n_1^e\omega_1 + n_2^e\omega_2$	$n_3^e\omega_3 = n_1^o\omega_1 + n_2^o\omega_2$
Type II	$n_3^o\omega_3 = n_1^o\omega_1 + n_2^e\omega_2$	$n_3^e\omega_3 = n_1^e\omega_1 + n_2^o\omega_2$

Uniaxial crystals have a particular optical axis. Light with polarization perpendicular to it is called ordinary polarization and experiences refractive index n_o. All other polarizations are called extraordinary and experience refractive index $n_e(\theta)$, where θ is the angle between the optical axis and wavevector **k**:

$$\frac{1}{n_e(\theta)^2} = \frac{\sin^2\theta}{n_e^2} + \frac{\cos^2\theta}{n_o^2} \tag{1.9}$$

where n_e and n_o are the principal extraordinary and ordinary refractive indexes at ω_3. Taking the type-I phase matching as an example:

$$n_e(\theta)\omega_3 = n_o(\omega_1)\omega_1 + n_o(\omega_2)\omega_2 \tag{1.10}$$

The phase matching angle is given by:

$$\theta = \arcsin\left[\frac{n_e}{n_e(\theta)}\sqrt{\frac{n_o^2 - n_e^2(\theta)}{n_o^2 - n_p^2}}\right] \tag{1.11}$$

1.3 Magneto-optical Kerr effect (MOKE)

Magneto-optical (MO) spectroscopy is a powerful method to investigate the spin phenomena in magnetic materials. Various methods including Magneto-optical Kerr effect/Faraday effect, magnetic-induced second-harmonic generation have been widely used [9]. Time-resolved magneto-optical spectroscopy with femtosecond laser pulses enables the study of spin dynamics.

Taking a simple example where the magnetization is along the z-axis, the permittivity tensor of a magneto-optic material is:

$$\varepsilon = \begin{pmatrix} \varepsilon_1 & \varepsilon_{xy} & 0 \\ -\varepsilon_{yx} & \varepsilon_1 & 0 \\ 0 & 0 & \varepsilon_2 \end{pmatrix} \tag{1.12}$$

where ε_{ij} are complex. The diagonal terms are even under time-reversal transformation (flip the magnetization), while the off-diagonal terms flip sign, leading to a nonzero magneto-optical effect. The off-diagonal terms indicate that left hand circularly polarized (LCP) and right hand circularly polarized (RCP) lights propagate differently in a material [10].

The complex MOKE Voigt vector is defined as:

$$\Theta_k = \theta_k + i\eta_k \tag{1.13}$$

where real part θ and imaginary part η are Kerr rotation and Kerr ellipticity, respectively. For the first-order estimation, the off-diagonal components are proportional to the magnetization. For

time-resolved experiments, the time-dependent Voigt vector is:

$$\Theta(t) = N(t) + f(t)M(t) \tag{1.14}$$

where $N(t)$ is the non-magnetic response, $f(t)$ are the Fresnel coefficients, and $M(t)$ is the time-dependent magnetization. To eliminate the non-magnetic response, one can measure the difference of response of two opposite magnetization directions:

$$\Delta\Theta(t) = [\Theta(M(t)) - \Theta(-M(t))]/2 \tag{1.15}$$

However, for ultrafast experiments, both the Fresnel factor and magnetization are time-dependent:

$$\Delta\Theta(t) = f \cdot \Delta M(t) + \Delta f(t) \cdot M \tag{1.16}$$

$$\frac{\Delta\Theta(t)}{\Theta(t)} = \frac{\Delta M(t)}{M(t)} + \frac{\Delta f(t)}{f(t)} \tag{1.17}$$

The pump-induced magneto-optical signal (Eq.(1.17)) no longer reflects the real spin dynamics due to the time-dependent Fresnel factor. However, in inverse Faraday effect $M(0) \propto \vec{E}(\omega) \times \vec{E}^*(\omega)$ the induced magnetization can be flipped by changing the helicity of the pump polarization (LCP $\leftrightarrow$ RCP). By subtracting the dynamics of opposite helicities of polarization one can remove the contribution of the time-dependent Fresnel term. Another way is to compare the Kerr rotation and ellipticity dynamics. Eq.(1.17) can be expressed as real and imaginary part according to Eq.(1.13):

$$\frac{\Delta\theta}{\theta_0} = \frac{\Delta M(t)}{M_0} + \frac{\Delta f'(t)}{f'_0} \tag{1.18a}$$

$$\frac{\Delta\eta}{\eta_0} = \frac{\Delta M(t)}{M_0} + \frac{\Delta f''(t)}{f''_0} \tag{1.18b}$$

where $f'(t)$, $f''(t)$ are the real and imaginary part of the Fresnel factor $f(t)$. If the response only

has magnetic contribution, dynamics of Kerr rotation and ellipticity should be exactly the same.

One example is using degenerate pump-probe to study ultrafast magneto-optics in Nickel [11]. The dynamics of Kerr rotation and ellipticity start to overlap after 0.5 ps, when the temporal profile starts to represent purely spin dynamics. This is due to "dichroic bleaching", where the probe light sees a highly nonequilibrium joint density of state induced by the same wavelength of pump. The spin dynamics can be depleted by the high excitation states.

Chapter 2

Techniques of Ultrafast Spectroscopy

2.1 Introduction

As the Nobel Physics laureate Philip Anderson stated for condensed matter physics: *more is different* [12]. There are numerous elementary excitations which are unique in condensed matter systems including phonons, magnons, density waves (charge density wave, spin density wave), plasmons, excitons, interband transitions, superconductivity, etc. Optical spectroscopy plays an important role in studying these phenomena through measuring changes in a material's optical properties in a non-contact fashion. With a more intense electromagnetic field, we can strongly modify, and even control, manipulate excited states in a non-equilibrium manner [13, 14].

The selection of the wavelength of electromagnetic field depends on the energy of the elementary excitation that is of interest. Fig.(2.1) shows some elementary excitations and their corresponding energy/time scale. In our lab, we have access to most of the energy range in Fig.(2.1). In this chapter, I will introduce the basic concepts of ultrafast pump-probe experiment followed by the experimental set-ups that I have designed and built during my Ph.D..

During the course of my PhD studies, I was involved in building an optical lab from scratch. The experimental light sources that will be covered in this chapter includes high sensitivity

Terahertz time-domain spectroscopy (THz-TDS) using ZnTe (0.2-2.6 THz), Broadband THz-TDS from two-color laser-induced gas plasma (0.4-23 THz), intensive mid-infrared pump (4 - 17 μm), and visible Noncollinear optical parametric amplifier (NOPA) (0.55 - 0.75 μm). Lastly, a novel data acquisition system that digitizes all the experimental signal is introduced.

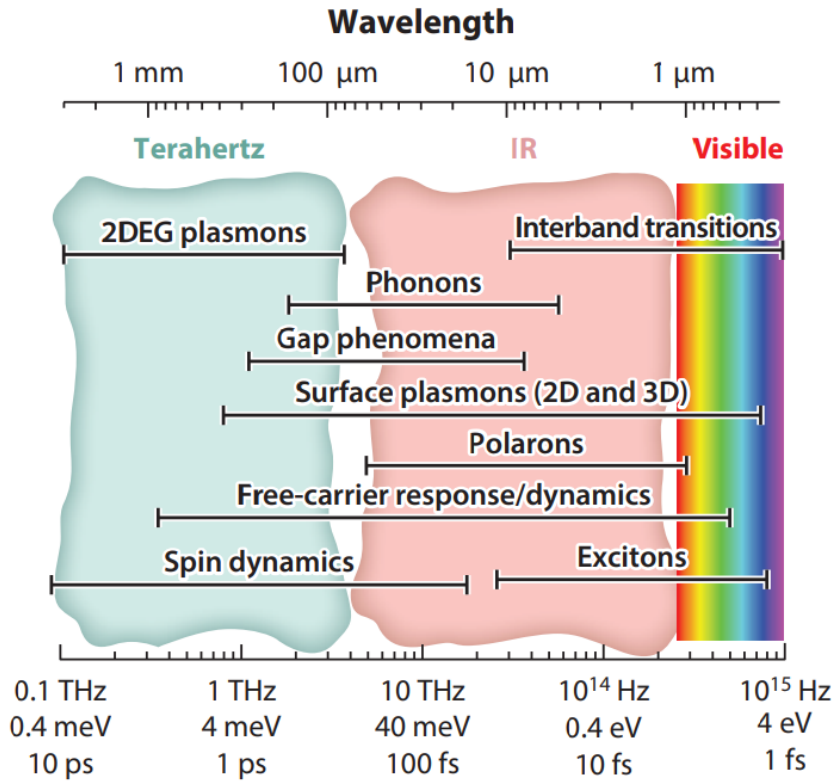

Figure 2.1: Figure from [15]. Elementary excitations and corresponding energy and timescale.

2.2 Pump-probe spectroscopy

Conventional optical spectroscopy is a very broad topic [16]. The optical properties of a material can be obtained by observing the amplitude or polarization change after transmission/reflection from it. Techniques of this kind include Fourier-transform infrared spectroscopy (FTIR), ellipsometry, magneto-optical spectroscopy and so on. With the development of ultrafast femtosecond (fs) lasers, pulsed light with typical time scale of tens to hundreds femtosecond

enables pump-probe spectroscopy [17]. In the simplest scenario of a pump-probe experiment, a stronger pump is used to excite the sample to an excited non-equilibrium state, followed by a weaker probe beam monitoring the pump-induced change in optical properties. Measuring the pump-induced change in optical properties as a function of pump-probe delay time gives us information about the relaxation of of the excited state to equilibrium. Phenomena like charge relaxation, electron-phonon coupling that happen in femtosecond to picosecond or even nanosecond can be captured by this technique. Various energy combinations of pump/probe beam can be chosen depending on the energy of interest of the sample.

The dynamics of pump-probe spectroscopy can be interpreted as [3]:

$$\frac{\Delta R}{R}(t) = \frac{\partial \ln(R)}{\partial \varepsilon_1}\Delta\varepsilon_1(\omega,t) + \frac{\partial \ln(R)}{\partial \varepsilon_2}\Delta\varepsilon_2(\omega,t). \tag{2.1}$$

Taking the reflection measurement as an example, ΔR is the pump-induced reflectively. $\Delta\varepsilon_1$ and $\Delta\varepsilon_2$ are the real and imaginary part of the dielectric function at certain probe energy ω, respectively. The pump-probe signal reflects the pump-induced change in both real and imaginary optical constants.

Besides the conventional two-beam pump-probe spectroscopy, more pump beams can be used to observe or control dynamics of the excited states [18]. One example is the enhancement and suppression of coherent spin waves [18] by varying the time delay between two pump pulses. As shown in Fig.(2.2)(a), strong THz pump drives magnon oscillation in NiO, which is captured by Faraday rotation probe. By varying the time delay of a third THz pump, the enhancement/suppression of the oscillation is realized (Fig.(2.2)(b)(c)).

2.3 Terahertz time-domain spectroscopy (THz-TDS)

THz-TDS is a very powerful optical technique to study condensed matter systems. It covers frequency range from 0.1 to multiple tens of THz [19, 20, 21]. A lot of interesting

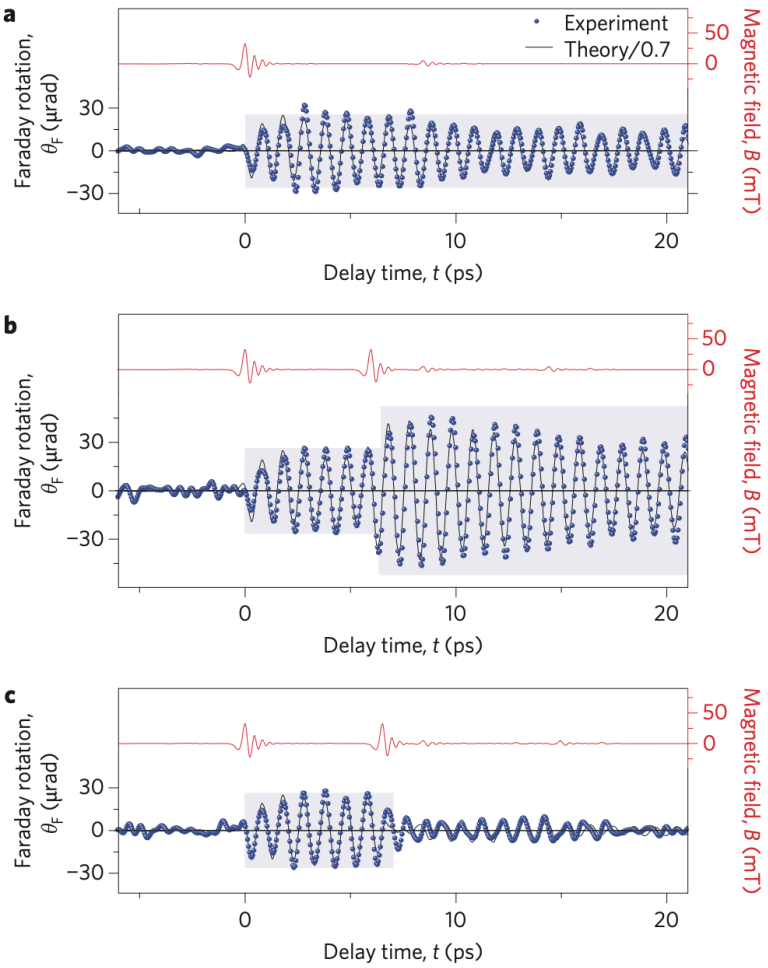

Figure 2.2: Figure from [18]. (a) Coherent magnon oscillation on antiferromagnet NiO using femtosecond THz pump Faraday rotation probe. (b) Enhancement of magnon oscillation after excitation by two THz pump pulses with time separation of 6 ps. (c) Suppression of magnon oscillation after excitation by two THz pump pulses with time separation of 6.5 ps.

condensed matter phenomena show up in this frequency regime including Drude response, Josphson plasma resonance, phonon, magnon, gap phenomena, etc. Since the frequency range usually covers the low-energy Drude response that converges to DC-conductivity σ_0, THz-TDS can be treated as a non-contact way to measure quasi-DC conductivity of a material. The Drude model is shown in Eq.(2.2)

$$\sigma(\omega) = \frac{\sigma_0}{1 - i\omega\tau} \tag{2.2}$$

where $\sigma_0 = ne^2\tau/m$ is the DC-conductivity, τ is the scattering time, and n is the carrier density.

Another important advantage of THz-TDS over other static optical techniques is that the direct measurement of time-domain electric field contains both amplitude and phase information rather than just intensity, thus no Kramers–Kronig relation is needed to extract the real and imaginary parts of optical constants.

There are two main parts in THz-TDS: THz generation and THz detection. THz generation and detection methods fall in three major categories :

- Photoconductive antenna [22, 23]
- THz crystals. Generation: ZnTe, GaP, $LiNbO_3$, etc. Detection: ZnTe, GaP, GaSe, etc [24, 25, 26].
- Two-color laser-induced gas plasma [20, 27]

Each method in the categories listed above can typically be used for generation and detection. Once THz light is generated, in principle any detection scheme can be used. For example, we used GaP and GaSe crystals to detect broadband THz generated from two-color laser-induced gas plasma.

I will mainly focus on the methods that I have implemented in the group: THz generation using ZnTe crystal and two-color laser-induced gas plasma, THz detection using crystals (ZnTe, GaP, GaSe).

2.3.1 THz generation: optical rectification

The THz generation mechanism for the crystals mentioned above is optical rectification (see Section 1.2). Consider two electric fields $E_1 = E_0 \cos \omega_1 t$ and $E_2 = E_0 \cos \omega_2 t$, the second-

order nonlinear electric polarization:

$$P_2^{nl} = \chi_2 E_1 E_2 = \frac{1}{2}\chi_2 E_0^2[\cos(\omega_1+\omega_2)t + \cos(\omega_1-\omega_2)t]. \tag{2.3}$$

The second-order nonlinear electric polarization consists of a difference frequency part P_2^d proportional to $\cos(\omega_1-\omega_2)t$ and a sum frequency part P_2^s proportional to $\cos(\omega_1+\omega_2)t$. The optical rectification is described by the difference frequency part P_2^d. The generation pulse we used is the fundamental light from a powerful regenerative amplifier laser (Spectra-Physics Spitfire XP) with central wavelength of 800 nm and bandwidth of 27 nm, which is broad enough to generate different frequency $(\omega_1-\omega_2)$ light in THz regime.

2.3.2 THz detection: electro-optic (EO) sampling

The THz detection schematic is shown in Fig.(2.3). An ultrashort optical sampling (gate) pulse overlaps with THz pulse on the detection crystal. Due to the Pockels effect, the change of birefringence of the detection crystal is proportional to the THz electric field. The transient THz electric field experienced by the detection crystal is quasi-static at a given time delay, which can be read out through the polarization change of the sampling pulse. The initial polarization of the optical sampling pulse is linear. Without the THz pulse, it becomes circularly polarized. After the Wollanston prism, the amplitude of the s- and p-polarized beams are the same. Detection by a balanced photo-diode pair results in a null signal. On the other hand, if the THz field is incident on the EO crystal at the same time of the sampling pulse, its ellipticity deviation from linear polarization can be read out from the balanced photo-detector. Crucially, the measured signal is proportional to the terahertz electric field.

It is crucial that the pulse duration of the optical sampling pulse needs to be much shorter (several to a hundred fs) than the THz (ps) pulse, such that by increasing the time delay between the THz and the sampling pulse, a time-domain THz trace can be captured.

The selection of EO crystal depends on the detection frequency range and sensitivity. As shown in table 2.1, ZnTe and GaP cannot be used to detect THz frequency higher than their lowest optical phonons (5.4 THz and 10.96 THz), while ZnTe has much better detection sensitivity thanks to its higher electrooptical coefficient. On the other hand, we use GaSe to detect THz of frequency higher than 7.1 THz.

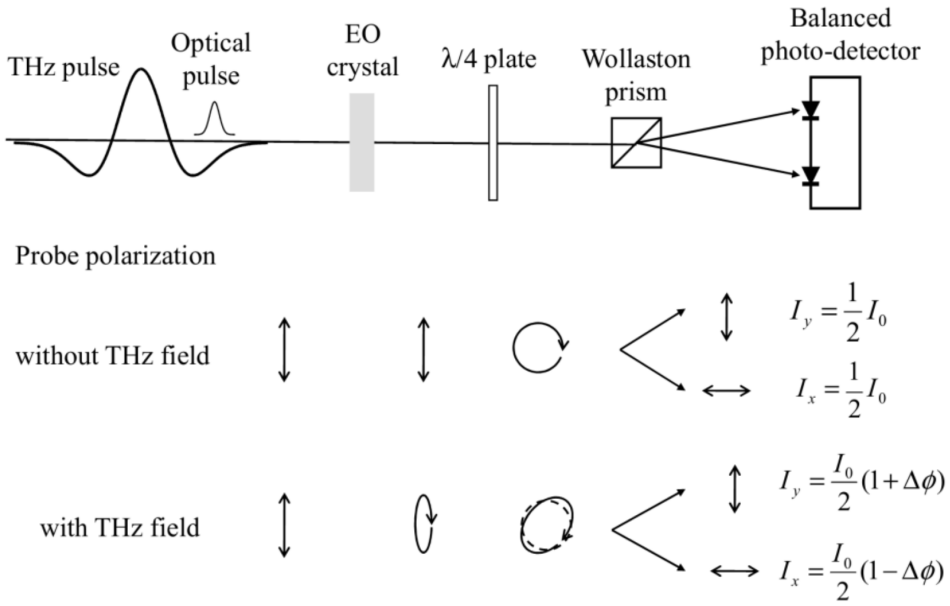

Figure 2.3: From [28]. The schematic of EO sampling: how to read out THz electric field by measuring the birefringence change of the optical sampling pulse.

Table 2.1: Physical properties of some commonly used THz detectors.

Material	lowest optical phonon (THz)	Electrooptic Coefficient (pm/V)
ZnTe	5.4	3.9
GaP	10.96	0.97
GaSe	7.1	14.4

2.3.3 THz-TDS data analysis

To extract the optical parameters from THz-TDS, both the sample and reference scans are required. Here I only consider the case of a transmission experiment, reflection can be derived

similarly. A common case is to measure a thin film with known thickness on a thick substrate. The thin file is the sample, and the bare substrate is the reference. Another case is a bulk sample, and air is used as reference.

Practically, temporal profile scans of THz pulses transmitted through sample (reference) are recorded as $E_{sig}(t)(E_{ref}(t))$. After appropriate zero padding, windowing, and Fourier transform, the THz spectrum of the sample (reference) in the frequency domain $E_{sig}(\omega)$ ($E_{ref}(\omega)$) is obtained. Their ratio yields the complex transmission coefficient:

$$T(\omega) = \frac{E_{sig}(\omega)}{E_{ref}(\omega)}. \tag{2.4}$$

Substrate parameter extraction

Let's first consider extracting optical parameters of a thick substrate with thickness d and refractive index n_2. In this case, the substrate is the sample and air is the reference. The Fabry-Perot term can be neglected since it will be separated from the main pulse in time domain.

The schematic is shown in Fig.(2.4) and we obtain

$$E_{sub}(\omega) = t_{12}P_2t_{21} = t_{12}t_{21}\exp[i\frac{\omega d}{c}n_2\cos\theta_2]. \tag{2.5}$$

where t_{12}, t_{21} are the transmission coefficient of THz light propagating from medium 1 to 2 and medium 2 to 1, respectively. Assuming the incident light is p-polarized, and according to Fresnel's equation:

$$t_{21}^p = t_{12}^p = \frac{2n_1\cos\theta_1}{n_1\cos\theta_2 + n_2\cos\theta_1}. \tag{2.6}$$

and $P_2 = \exp[i\frac{\omega d}{c}\cos n_2\theta_2]$ is the phase factor from the propagation inside medium 2.

Similarly, $E_{air} = P_1 = \exp[i\frac{\omega d}{c}n_1\cos\theta_1]$. For normal incidence and $n_1 = 1$, the total

transmission coefficient yields:

$$T(\omega) = \frac{E_{sub}(\omega)}{E_{air}(\omega)} = t_{12}t_{21}exp[i\frac{\omega d}{c}(n_2\cos\theta_2 - n_1\cos\theta_1)] \\ = \frac{4}{(\widetilde{n}_2+1)^2}\exp[i\frac{\omega d}{c}(\widetilde{n}_2-1)]. \tag{2.7}$$

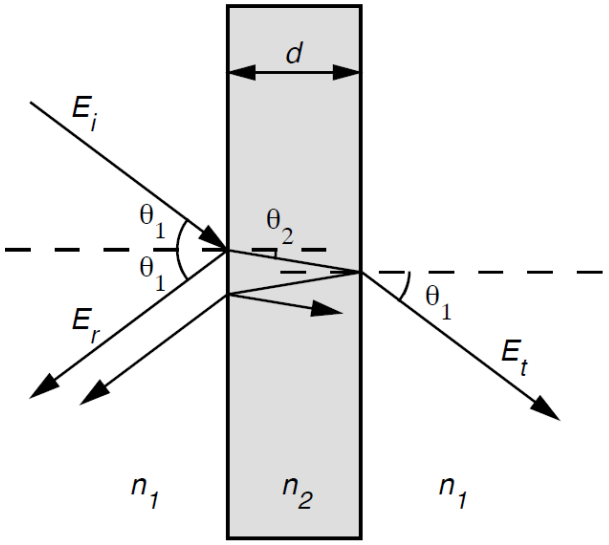

Figure 2.4: From [29]. Schematic of THz light transmitted through a substrate of thickness d and refractive index n_2.

Thin film on thick substrate

For a thin film on a thick substrate (Fig.(2.5)), a Fabry-Perot term F needs to be considered for the thin film. The THz pulse gets multi-reflection in the thin film and superimposed with propagation phase factor P_2:

$$FP_2 = \frac{\exp[i\frac{\omega d}{c}n_2\cos\theta_2]}{1 + r_{12}r_{21}\exp[2i\frac{\omega d}{c}n_2\cos\theta_2]}. \tag{2.8}$$

where r_{12} is the reflection coefficient.

Assuming the THz electric field after transmission through the film and substrate is E_{sig},

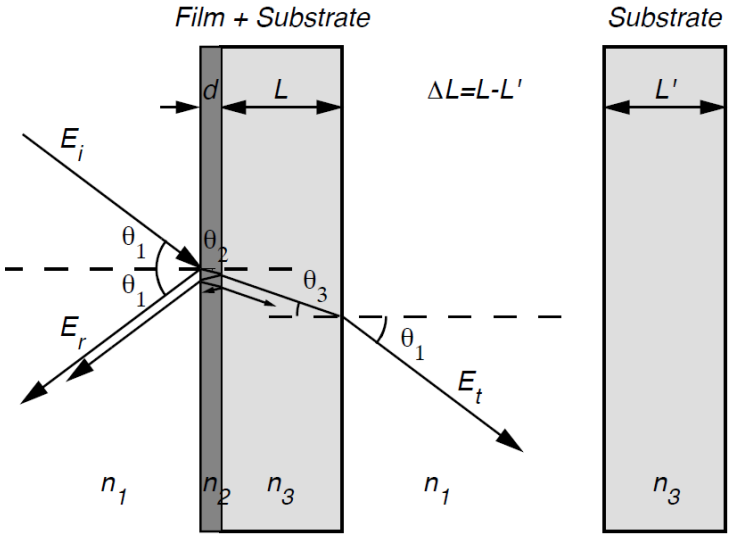

Figure 2.5: From [29]. Schematic of THz light transmitted through a substrate of thickness d and refractive index n_2.

and its reference is a bare substrate with transmitted electric field E_{ref}.

$$\begin{aligned} E_{sig}(\omega) &= t_{12}FP_2t_{23}P_3t_{31} \\ &= \frac{t_{12}t_{23}\exp[i\frac{\omega d}{c}n_2\cos\theta_2]}{1+r_{12}r_{21}\exp[2i\frac{\omega d}{c}n_2\cos\theta_2}\exp[i\frac{\omega L}{c}n_3\cos\theta_3]t_{31}. \end{aligned} \tag{2.9}$$

$$\begin{aligned} E_{ref}(\omega) &= P_1t_{13}P_3't_{31}P_{\Delta L} \\ &= \exp[i\frac{\omega d}{c}n_1\cos\theta_1]t_{13}\exp[i\frac{\omega L'}{c}n_3\cos\theta_1]t_{13}\exp[i\frac{\omega\Delta L}{c}n_1\cos\theta_1]. \end{aligned} \tag{2.10}$$

where ΔL is the thickness difference between the sample substrate and bare substrate. The transmission coefficient can be calculated and simplified for normal incidence and $n_1 = 1$ as

$$T(\omega) = \frac{E_{sig}(\omega)}{E_{ref}(\omega)} = \frac{\frac{2(n_3+1)}{(n_2+1)(n_2+n_3)}\exp[i\frac{\omega d}{c}(n_2-1)]}{1+\frac{(n_2-1)(n_3-n_2)}{(n_2+1)(n_3+n_2)}\exp[2i\frac{\omega d}{c}n_2]}\exp[i\frac{\omega\Delta L}{c}(n_3-1)]]. \tag{2.11}$$

Without losing generalization, we assume the phase factor from the thin film is negligible,

$\frac{\omega d}{c} n_2 \ll 1$ and $n_2 \gg n_3 > 1$. The transmission coefficient can be further simplified to

$$T(\omega) = \frac{1+n_3}{1+n_3+Z_0\sigma(\omega)d} \exp[i\frac{\omega\Delta L}{c}(n_3-1)]. \tag{2.12}$$

where $Z_0 = \sqrt{\frac{\mu_0}{\varepsilon_0}}$ is the impedance of free space.

The complex conductivity can thus be derived as

$$\sigma(\omega) = [\frac{\exp[\frac{i\omega\Delta L}{c}(n_3-1)]}{T(\omega)} - 1]\frac{1+n_3}{Z_0 d}. \tag{2.13}$$

Eq.(2.13) is the most frequently used equation to extract the conductivity of a materials from THz-TDS measurements.

Dynamical conductivity extraction

For optical-pump THz-probe experiments, the conductivity is modified by a pump pulse. To extract the pump-induced conductivity change $\Delta\sigma$, we do the derivative of Eq.(2.13) with respective to the transmission coefficient $T(\omega)$:

$$\frac{d\sigma(\omega)}{dT(\omega)} = -\frac{(1+n_3)\exp[\frac{i\omega\Delta L}{c}(n_3-1)]}{Z_0 d}\frac{1}{T^2(\omega)}. \tag{2.14}$$

If $dT(\omega)$ is relatively small compared with $T(\omega)$, we can estimate the pump-induced conductivity change to be

$$\begin{aligned}\Delta\sigma(\omega,\tau) &= -\frac{(1+n_3)\exp[\frac{i\omega\Delta L}{c}(n_3-1)]}{Z_0 d}\frac{\Delta T(\omega)}{T^2(\omega)} \\ &= -\frac{(1+n_3)\exp[\frac{i\omega\Delta L}{c}(n_3-1)]}{Z_0 d}\frac{E_{ref}}{E_{sig}^2}\Delta E(\omega,\tau).\end{aligned} \tag{2.15}$$

In this equation, τ is the pump-probe delay time, and ΔE is the pump induced signal change. Eq.(2.15) indicates the linear relation between the pump-induced conductivity change and pump-induced signal change.

2.3.4 High sensitivity THz-TDS using ZnTe

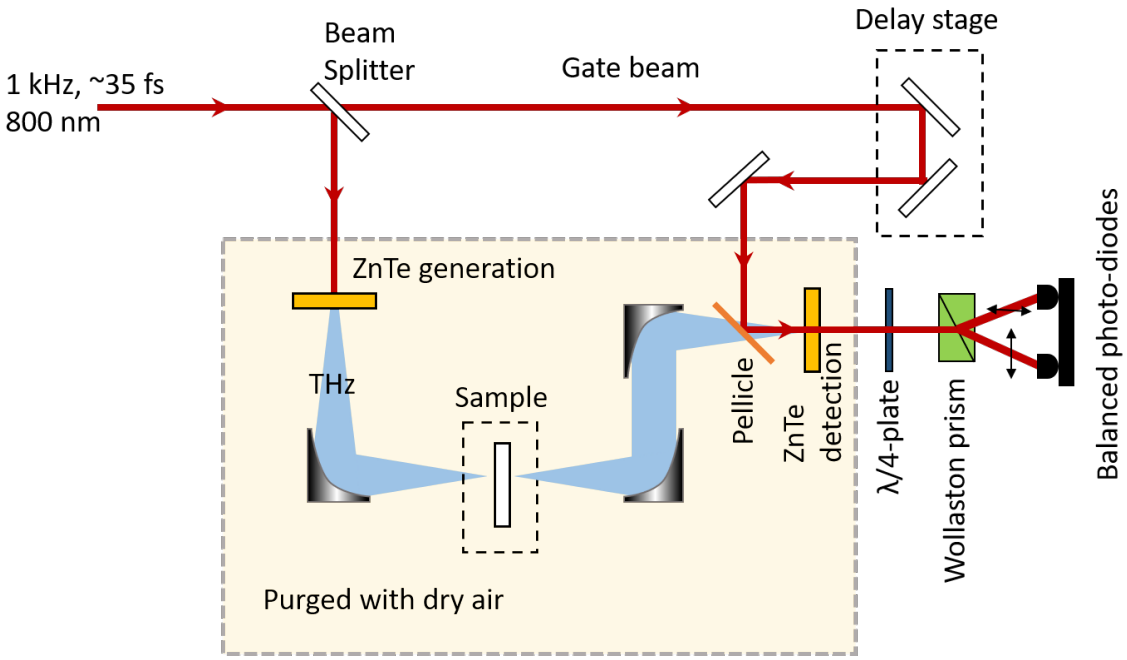

Figure 2.6: Schematic of the high-sensitivity THz-TDS transmission set-up. THz is generated and detected using ZnTe crystal.

The THz-TDS set-up using ZnTe as generation and detection crystal has the advantage of high sensitivity (up to 10k signal-to-noise ratio) and robustness. The generation pulse is the near-IR light from a powerful regenerative amplifier laser (Spectra-Physics Spitfire XP) with central wavelength of 800 nm, pulse duration of 35 fs, and repetition rate of 1 kHz. The beam splitter separates the input beam into a strong generation beam and a weak gate beam (used to EO sample the THz pulse). The THz is generated after the ZnTe crystal, and is focused onto the sample using an off-axis parabolic (OAP) mirror. The typical THz beam size on the sample has a diameter of ~ 3 mm. After transmitting through the sample, the THz light is collimated and refocused on the detection ZnTe crystal, overlaped with the near-IR gate beam (reflected by the pellicle beamsplitter). The THz signal at a certain THz-gate time delay can be futher read out by the EO sampling process. By varying the time delay of the gate beam, a full time-domain THz trace can be captured.

The schematic of the high-sensitivity THz-TDS transmission set-up is shown in Fig.(2.6). In principle, any kind of pump beam can be added to the system for pump-THz-probe experiment.

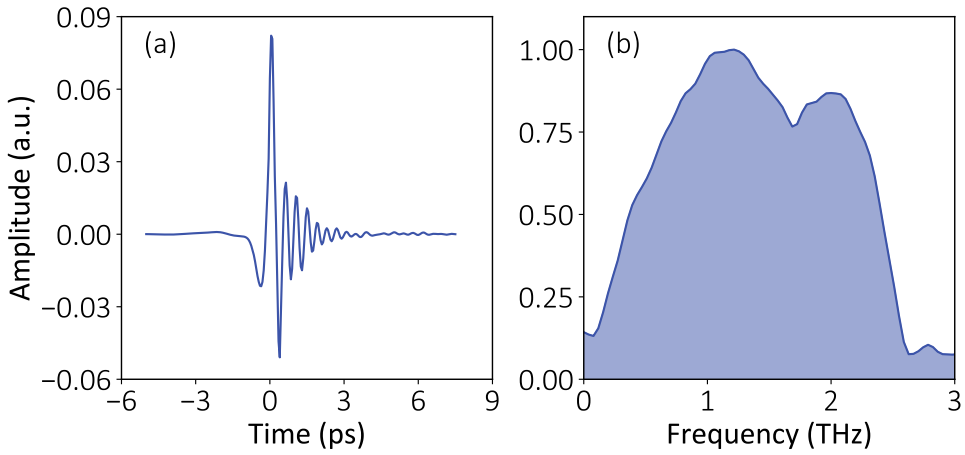

Figure 2.7: The typical THz time-domain scan (a) and frequency spectrum (b) for ZnTe THz-TDS system.

The typical time-domain THz trace is shown in Fig.(2.7)(a), with its Fourier amplitude spectrum shown in Fig.(2.7)(b). The spectrum ranges from 0.1 THz to 2.6 THz, and with detection signal to noise up to 10,000.

An example of using ZnTe based THz-TDS setup to measure the THz conductivity of V_2O_3 is shown in appendix A. The THz conductivity and hysteresis of V_2O_3 captured by THz-TDS is consistent with the results from conventional conductivity measurements, elaborating the first-order nature of its metal-to-insulator transition around 150 K.

2.3.5 Broadband THz-TDS from two-color laser-induced gas plasma

Overview

THz-TDS systems based on THz generated from crystals and photo-conductive antenna have the advantage of robustness and high-sensitivity, but the THz electric field is weak and the bandwidth is limited to 3 THz. The last two decades have witnessed the development of intense THz pulse generated from $LiNiO_3$ [30, 31, 32] and organic crystals (OH1 [33, 34], DSTMS

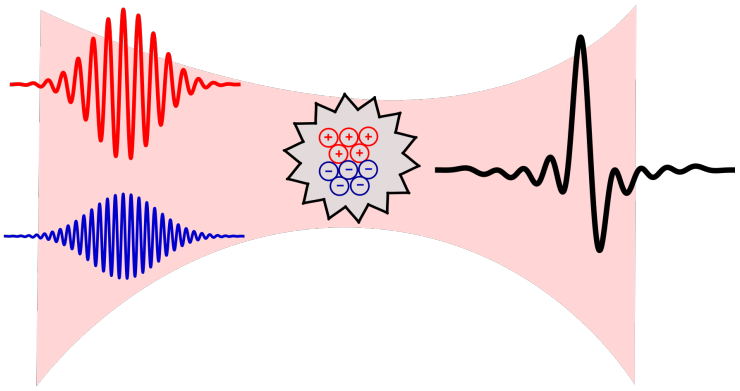

Figure 2.8: 800 nm fundamental beam and its second-harmonic 400 nm beam are focused into gas to generate plasma.

[35, 36, 37], DAST [38]) up to electric field of MV/cm, which facilitates the application of nonlinear THz optics and spectroscopy [39]. However, its spectrum is still limited to below 3 THz, lacking in THz generation techniques from 3 to 20 THz.

The development of two-color laser-induced gas plasma source fills this gap. It can be used as a versatile tool for both intense and broadband THz generation [20, 27, 40]. The bandwidth depends on the pulse duration of the generation and detection. For a 35 fs pulse, it extends from 0.1 to 23 THz. Such a broadband spectrum enables the time domain measurement of of numerous intriguing phenomena (phonons, magnons, gaps, plasma edge). On the other hand, the THz electric field strength from the plasma source can be tens to hundreds of kV/cm, making it usable for nonlinear THz spectroscopy, remote THz sensing [41, 42] etc.

Generation

The most common way to generate the gas plasma is by focusing a 800 nm fundamental pulse (ω) with its second-harmonic (2ω) into gas molecules. The polarization and power of the generated THz are determined by the relative phase difference (ϕ) between ω and 2ω beams[1], their polarization, and the plasma filament length [43, 44]. More specifically, if both ω and 2ω are linear polarized, the polarization of THz is also linear and follows the polarization of 2ω [45].

[1] Caused by different speed of light of ω and 2ω in air.

However, the THz generation efficiency is about one order of magnitude larger if ω and 2ω are parallel than they are perpendicular. The THz intensity follows a sinusoidal relation with respect to ϕ. If both ω and 2ω beams are circularly polarized, when the relative phase ϕ change, the polarization of THz rotates while keeping it intensity the same [45]. When ω beam is circularly polarized while 2ω is linearly polarized, THz polarization and ellipticity can be fully controlled by ϕ and the length of a plasma filament [44].

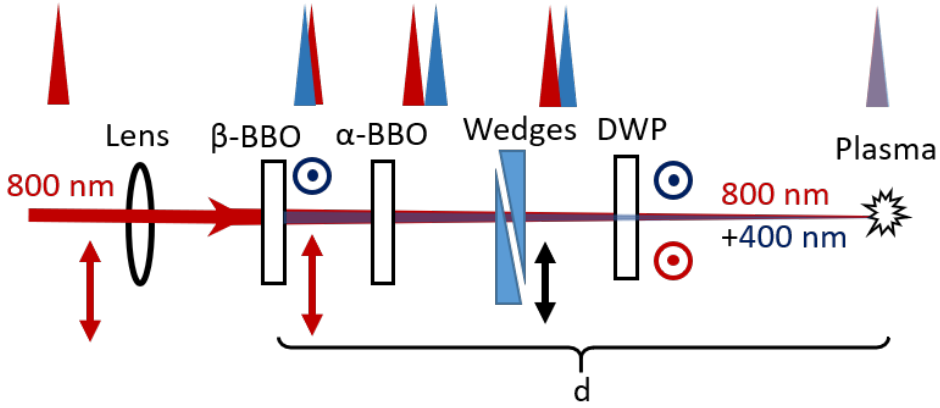

Figure 2.9: Schematic of the plasma generation setup. BBO, Beta Barium Borate crystal; DWP, Dual-waveplate. d: distance from BBO to the plasma. The polarization and relative phase of 800 nm amd 400 nm pulese are shown in red and blue.

The relative phase ϕ between ω and 2ω beams needs to be controlled precisely to tune the intensity and polarization of THz beam. Fig.(2.9) shows the generation part of the plasma setup. As depicted in the figure, p-polarized 800 nm together with its second-harmonic s-polarized 400 nm generated from β-BBO are focused into gas to form plasma filament. The simplest way to control relative phase ϕ is to adjust the position of β-BBO since the speed of light of ω and 2ω is different [43]. The relative phase difference is $\Delta\phi = \omega(n_\omega - n_{2\omega})\Delta d/c$, where c is speed of light in vacuum, Δd is the change of the BBO position and n_ω and $n_{2\omega}$ are the refractive indices in the air.

However, changing the position of BBO is not accurate enough to precisely tune the relative phase. The combination of a birefringent plate (α-BBO) and wedges provide attosecond

phase control accuracy [45, 46]. After the β-BBO crystal, the ω beam is ahead of 2ω. The α-BBO acts as a birefringent plate to delay ω after 2ω beam. The wedge pair can convert the coarser mechanical stage step to very fine steps in optical delay through the reltaion $\Delta\phi = \omega(n_\omega - n_{2\omega})\Delta l \tan\theta/c$, where Δl is the lateral displacement of mechanical stage, n is the refractive index of the wedge, and θ is the wedge angle. Finally the ω and 2ω beams can be adjusted to arrive at exactly the same time to maximize the generation efficiency of the plasma.

Detection

The THz time domain signal can be detected by THz-field-induced second harmonic (TFISH) [47], air-biased coherent detection (ABCD) with the addition of heterodyning detection [48] or EO sampling. In our setup, we choose the EO sampling method, using GaP crystal to detect 0.1-7.5 THz and GaSe crystal for 7.5-23 THz.

Generation mechanism

The generation mechanism of broadband THz from plasma filament has been under debate for a long time. The first proposed scenario is optical rectification by four-wave mixing [20]:

$$E_{THz}(t) \propto \chi^{(3)} E_{2\omega}(t) E^*_{\omega}(t) E^*_{\omega}(t) \cos\phi \tag{2.16}$$

where ϕ is the relative phase between the fundamental (ω) and second-harmonic (2ω) beams. The THz frequency is determined by difference frequency $E_{THz} = E_{2\omega} - 2E_{\omega}$, and its power scales with $P_1 P_2^2$ (Eq.(2.16)), where P_1 and P_2 are powers of the two pulses. Although experiments support the scaling relation [49], other research indicates that the third order nonlinearity $\chi^{(3)}$ either from thermal or ponderomotive effect is too small to explain the strong THz field strength [50].

Besides common laser frequency ratios (ω_2/ω_1 = 1:2), THz can also be generated effectively from uncommon ratios (ω_2/ω_1 = 1:4, 2:3 and 3:4) [51, 52]. The THz field strength

shows similar scaling behavior with different frequency ratios, suggesting another mechanism that four-wave mixing. A plasma current model (field ionization) was proposed as an alternative [50, 53], where the THz generation includes two processes [52]:

- Net-current formation from field ionization, shorter than laser pulse duration

$$\mathbf{J}_0 = -en_e\mathbf{v}_0 = \frac{e^2 n_e \mathbf{A}_L(\psi_0)}{m_e c} \tag{2.17}$$

  where $v_0 = -e\mathbf{A}_L(\psi_0)/m_e c$ is the electron velocity, $\mathbf{A}_L$ is the laser vector potential, ψ_0 is the electron creation position.

- Radiation generation while current is modified by the plasma

$$(\nabla^2 - \frac{1}{c^2}\frac{\partial^2}{\partial t^2} - \frac{\omega_p^2}{c^2})\mathbf{A}_{THz} = -\frac{4\pi\mathbf{J}_0}{c} \tag{2.18}$$

  where $\omega_p = \sqrt{4\pi e^2 n_e/m_e}$ is the plasma oscillation frequency.

Particle-in-cell simulation [52, 54] are consistent with the high-efficiency generation laser frequency ratio. It is also shown both in simulation and experiments that the THz generation efficiency decreases with the increasing laser frequency and scales linearly with the laser wavelength [54, 55]. For example the THz generation efficiency from two-color laser plasma for 1800 nm is 30 times stronger than that for 800 nm [55].

Experimental layout

The experimental layout for the two-color laser-induced gas plasma source is shown in Fig.(2.10). The input is a 35 fs, 2 mJ, p-polarized 800 nm fundamental pulse from regenerative amplifier. 99% of the power is used for the plasma generation, and the remaining serves as gate beam to EO sample the THz. The generation beam is focused by a 6-inch lens through a 100 μm type-I β-BBO crystal to generate second-harmonic which is s-polarized. A 45 μm thick

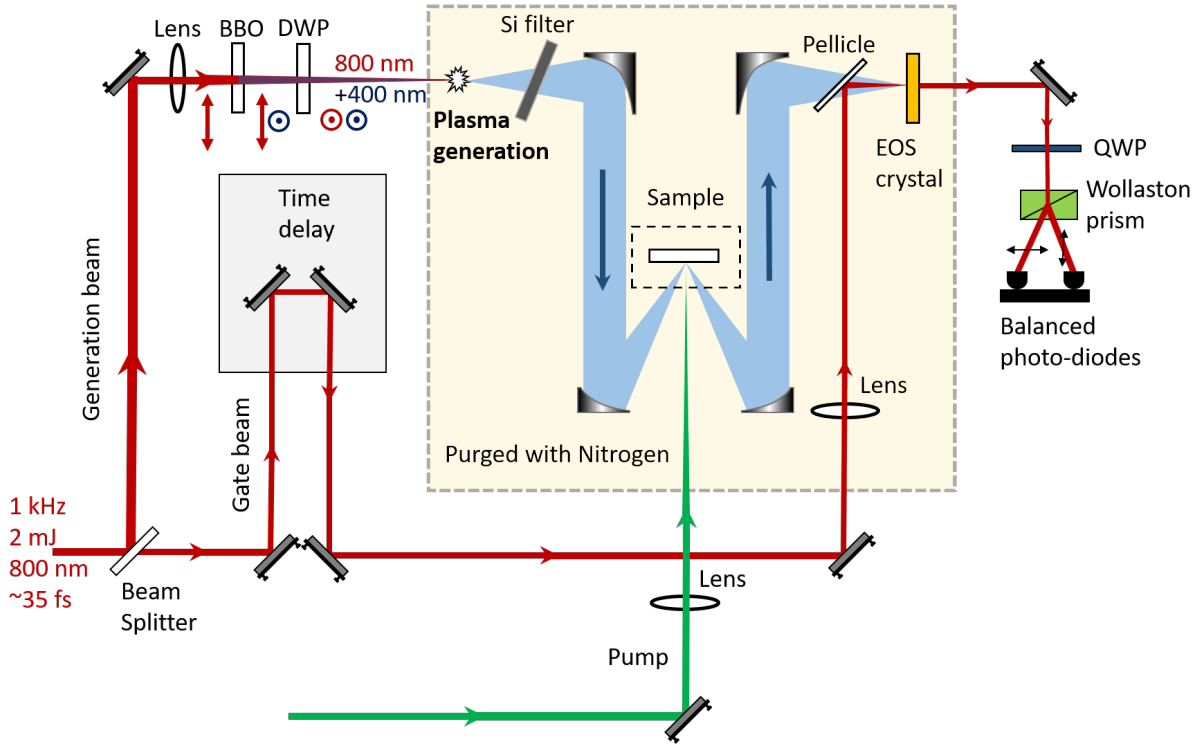

Figure 2.10: Schematic of the two-color laser-induced gas plasma THz-TDS. BBO, β-Barium Borate crystal; DWP, Dual-waveplate; QWP, Quarter-waveplate.

dual-waveplate is used to rotate the polarization of 800 nm by $\pi/2$ to match the polarization of its second-harmonic. This is to maximize the THz generation efficiency [46]. For simplicity, we don't use the phase compensator (α-BBO + wedges). 800 nm and 400 nm beams are then focused into nitrogen gas to generate plasma, followed by the radiation of broadband THz. The advantage of using nitrogen purged box is that first the THz generation efficiency in nitrogen is very good [56], and second it eliminates THz absorption from water vapor. After the generation of broadband THz, a silicon wafer is used to block the residual laser beams. The THz is then collimated by a 4-inch focal length off-axis parabolic mirror (OAP), focused on the sample, and then recollimated, refocused on the EO sampling crystal for detection. We use different EO crystals to detect different spectra range: 300 μm $\langle 110 \rangle$ GaP for 0.3-7.5 THz and 90 μm z-cut GaSe for 7.5-23 THz. The beam size of the gate beam needs to be small enough to match the THz beam on the EOS crystal to avoid any smearing of temporal resolution. This is also crucial

to achieve good detection bandwidth and sensitivity.

The broadband THz source from plasma filament covers the spectrum from 0.3 to 23 THz, which makes the detection of a lot more fundamental excitations like phonon, magnon, charge gaps in condensed matter system available [48, 57, 58, 59]. This can be used either as a broadband THz-TDS spectrometer in reflection, or a pump-broadband THz-probe setup with the addition of a pump beam. Currently we use the 2.4 μm idler beam from an optical parametric amplifier (OPA) as a pump beam.

Time domain signal and spectrum

The THz time domain signal is EO sampled by different crystals: GaP for 0.1 - 7.5 THz and GaSe for 7.5 - 23 THz. As shown in Fig.(2.11)(a), same THz time domain signal is sampled by different crystals: The GaP detection is the red curve while the GaSe is the blue curve. The signal-to-noise ratio for GaP is around 1000:1 and for GaSe is around 300:1. The spectrum in Fig.(2.11)(b) shows that the full spectrum from 0.1 to 23 THz is covered by using two EO sampling crystals. For a given experiment, we can choose the one (or both) whose spectrum is of interest to achieve the best detection performance.

2.4 Mid-infrared-pump optical/Kerr rotation-probe

The mid-infrared (mid-IR) wavelength from $\sim 5\ \mu m$ to $\sim 17\ \mu m$ covers the range of a lot of interesting condensed matter phenomena like phonons, magnons, charge gaps. The generation of such intense mid-infrared beam [60] makes the research of nonlinear light-matter interaction possible. Examples include high-harmonic generation in semiconductors and 2D materials [14, 61, 62, 63, 64, 65], control of electronic phase in mangnite via direct vibration modes excitations [66], and photo-induced superconductivity through nonlinear phononics [67, 13].

Here we use intense mid-IR pulses as pump and 800 nm optical beam as probe, which

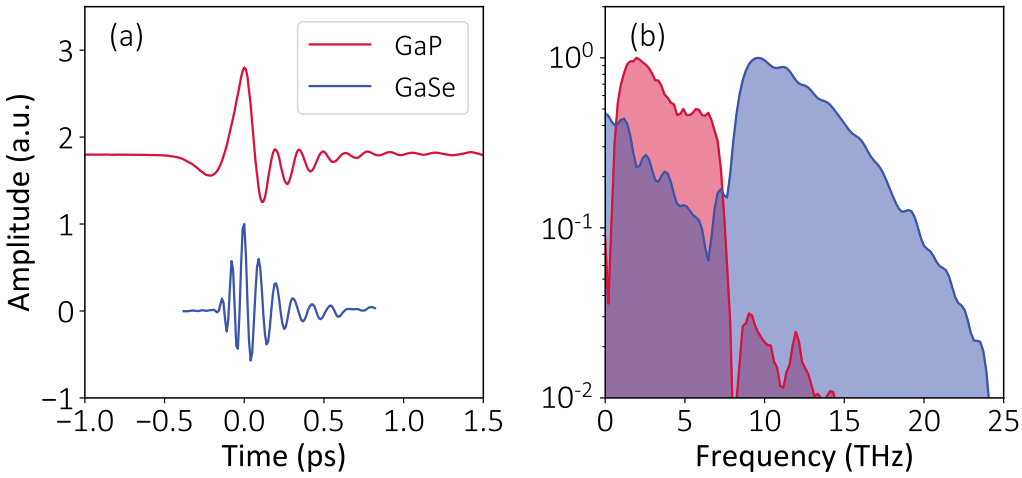

Figure 2.11: (a) The time domain signal (red curve is displaced for clarification) and (b) corresponding spectrum of THz generated from two-color laser plasma detected by GaP (red) and GaSe (blue) crystal.

can either be reflectivity ($\Delta R/R$) or Kerr rotation ($\Delta\theta$). The experimental scheme is shown in Fig.(2.12). Two beams of 800 nm, $\sim$ 100 fs, 1.9 mJ, 1 kHz repetition rate from a Ti:sapphire regenerative amplifier (Spitfire Ace) are input into TOPAS-Twins, which consists of two 2-stage OPAs seeded with the same white light to guarantee passive stable carrier envelope phase (CEP). Each OPA is tunable: signal from 1160 - 1600 nm and idler from 1600 – 2600 nm. The maximum power of signal is $\sim$ 330 mW at $\sim$ 1.2 μm. We focus two signal outputs into 0.6 mm GaSe to generate intense CEP stable mid-IR beam. The generation mechanism is type-II difference frequency generation (DFG) in GaSe, where the mid-IR frequency is determined by the energy difference and phase matching condition of the two near-IR beams. The mid-IR generation efficiency can be affected by the beam sizes of the two near-IR beams on GaSe crystal. We notice that there is saturation of how much mid-IR can be generated per area, the beam size of the two near-IR pulses on the GaSe crystal needs to be chosen to maximize the generation efficiency by adjusting the focusing lens. Too small of beam size limits the mid-IR generation by the saturation, and too big of beam size yields unsatisfactory generation efficiency.

The mid-IR power reaches the maximum of 13 mW around 9 μm with the combined

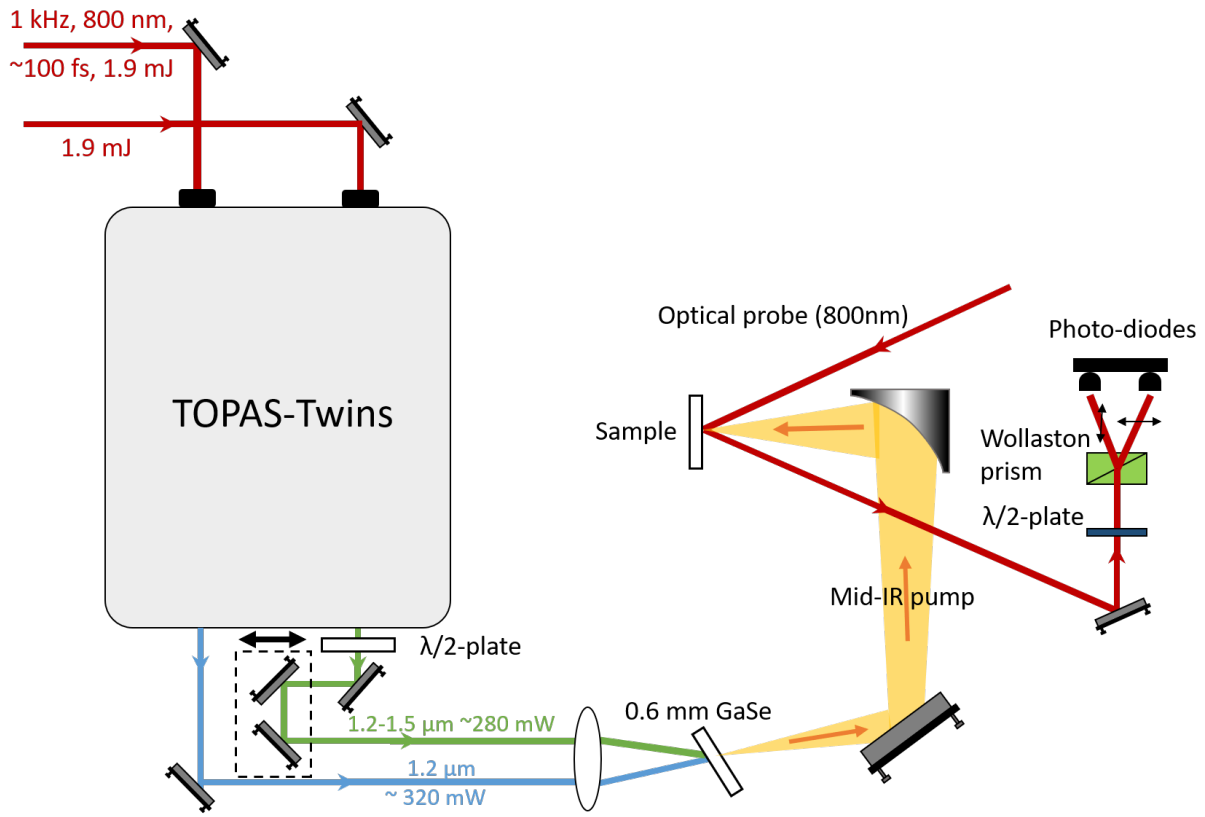

Figure 2.12: Experimental scheme of mid-IR pump Kerr rotation probe.

power of near-IR beams to be $\sim$ 580 mW, yielding a 2.2% generation efficiency. By focusing such intense mid-IR down to $\sim$ 60 μm, we can get electric field strength up to $\sim$ 70 MV/cm. The mid-IR wavelength can be tuned from 5 μm to 17 μm (see Fig.(2.13)). We fix one of the near-IR wavelength at 1.2 μm, adjust the other wavelength and rotate the angle of GaSe crystal for correct phase matching condition.

The reflected probe pulse (800 nm) propagates through a half-wave plate and a Wollaston prism, hitting on two identical photodiodes. The pump-induced polarization rotation can be measured by the imbalance of the photocurrent ΔI of the two photodiodes, and the magneto-optical Kerr signal $\Delta I/2I$ (2I is the sum of the photocurrents) is recorded at different time delays between the pump and probe pulses.

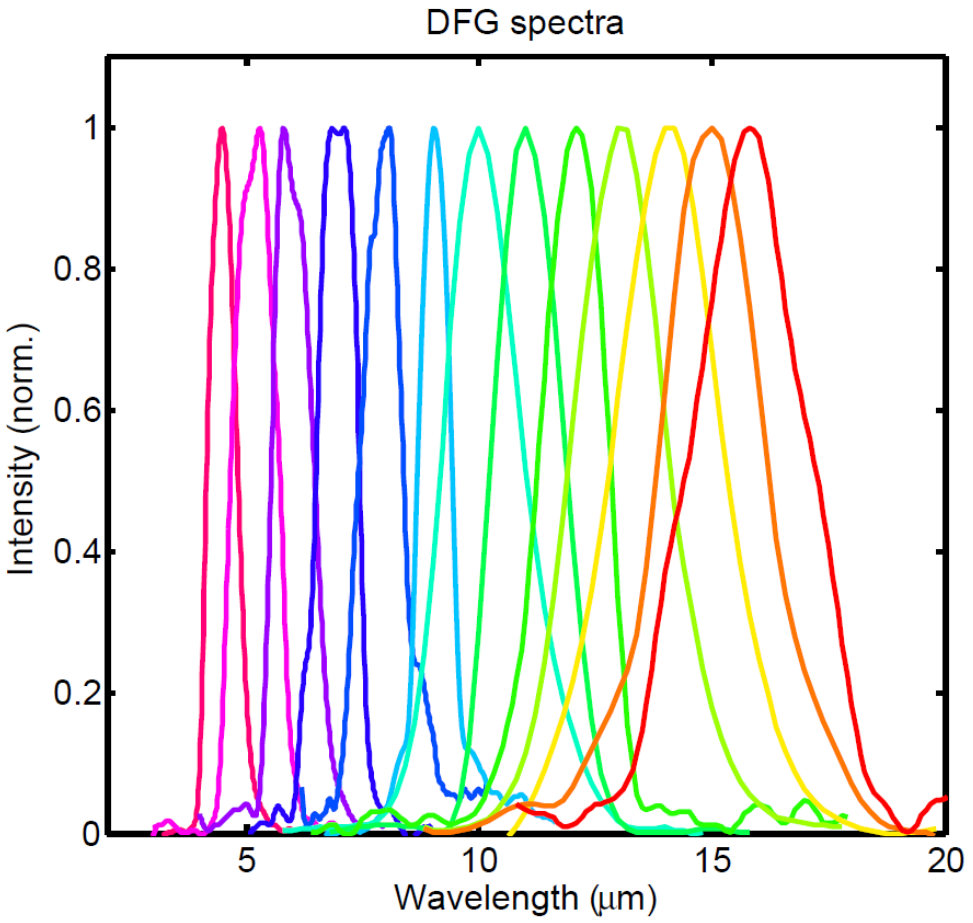

Figure 2.13: Normalized spectra of mid-IR from DFG measured by monochromator.

2.5 Data acquisition (DAQ) system

The extraction of very weak pump-probe signals is challenging. Lock-in amplifier has been the standard equipment since the 1930's to extract signal from noisy background by locking the detection frequency to the modulation frequency of the signal. However, pulsed lasers experience shot-to-shot noise and long-term drift during the measurement, making the signal analysis more complicated. A more straightforward way to overcome this is to record each pulse by the data acquisition (DAQ) system. The DAQ system digitizes all the signals from photodiode pulse by pulse, allowing real time noise reduction, and it has competitive signal to noise performance as the lock-in amplifier [68]. Also various post data analysis methods can be implemented.

We implemented the DAQ on the our 1 kHz regenerative amplifier laser system. The DAQ card is PXIe-5122 from National Instrument with 100 MHz maximum sampling rate, 100 MHz bandwidth, and 14-bit analog digitization. The sampling rate is enough to digitize the signal on most of the photodiodes with bandwidth smaller than $\sim$ 10 MHz. We mainly focus on the THz-TDS and pump-THz-probe experiments using 1 MHz bandwidth Newport 2307 balanced photodiodes.

2.5.1 DAQ for THz-TDS

A typical temporal sequence of data taking for THz-TDS experiments is shown in Fig.(2.14). The repetition rate of the gate pulse is 1 kHz, and the THz pulse is chopped at 500 Hz, which means the gate beam sees the THz on the detection crystal every other millisecond (ms). The DAQ is triggered by a 500 Hz TTL signal from frequency dividing the laser TTL signal [2]. The signal on the balanced photodetector for each pulse is fully digitized by DAQ, which enables further post analysis of the signal pulse by pulse. The temporal sequence is divided into

[2]The reason for not using the TTL signal from the optical chopper is that it's not stable enough to trigger the DAQ.

millisecond, as shown in Fig.(2.14) in sections 1, 2, 3. At the first millisecond, since both the gate and THz beams are on the detection crystal, the signal on the balanced photodiode is proportional to the instantaneous THz electric field plus some background, as shown in the black signal in the third row. We select a boxcar integration time window (orange dotted rectangle) that covers only the signal to obtain the integrated signal[3] (blue and red shaded region) without adding the noise tail. At the second millisecond, the THz is blocked by the chopper, and only the gate beam on the detection crystal, yielding a balanced output. The integrated signal is thus a background. The THz signal from the first two milliseconds is calculated by $E_{THz} = A_2 - A_1$, where A_1, A_2 is the integrated signal of the first and second millisecond.

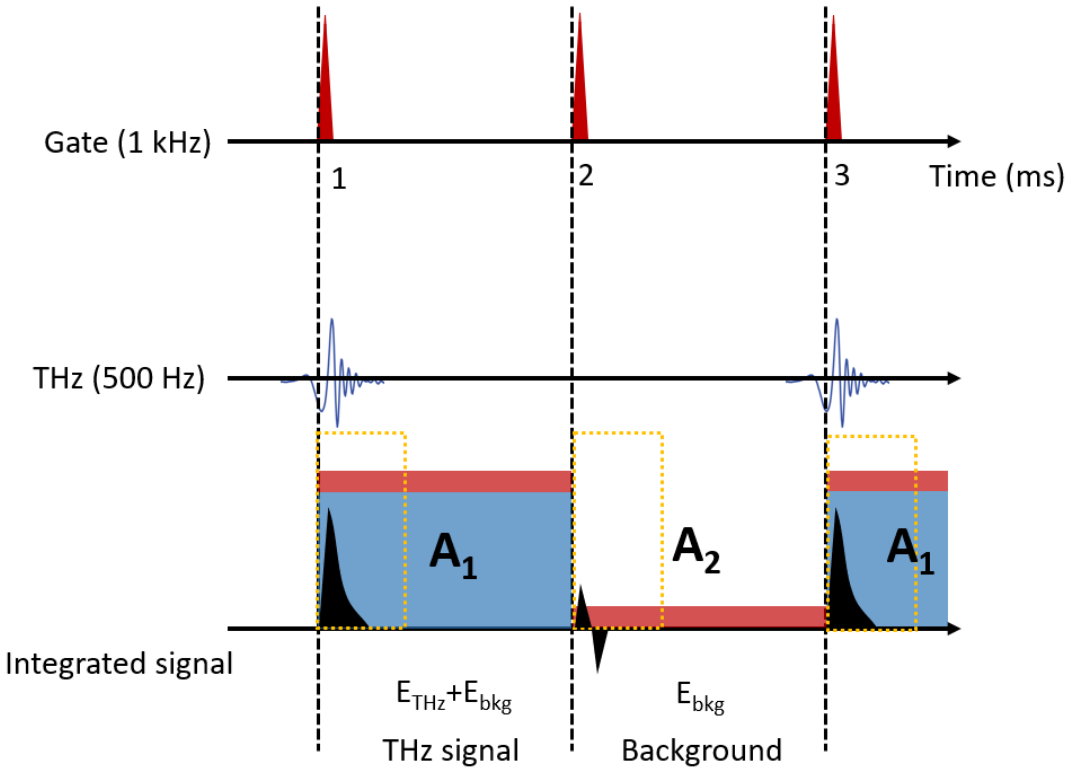

Figure 2.14: Temporal sequence of data taking for THz-TDS experiments using DAQ. Red pulse: gate beam, 1 kHz; blue pulse: THz probe, 500 Hz. The black signal at the third row is the balanced photodetector signal digitized by DAQ. The orange rectangle shows the boxcar window that sums over the desired data points to get the integrated signal for each millisecond shown in blue shaded square (THz signal) and red shaded rectangle (background).

[3]By summing over all the data points in the selected time window.

The connection diagram of DAQ for THz-TDS experiment is shown in Fig.(2.15).

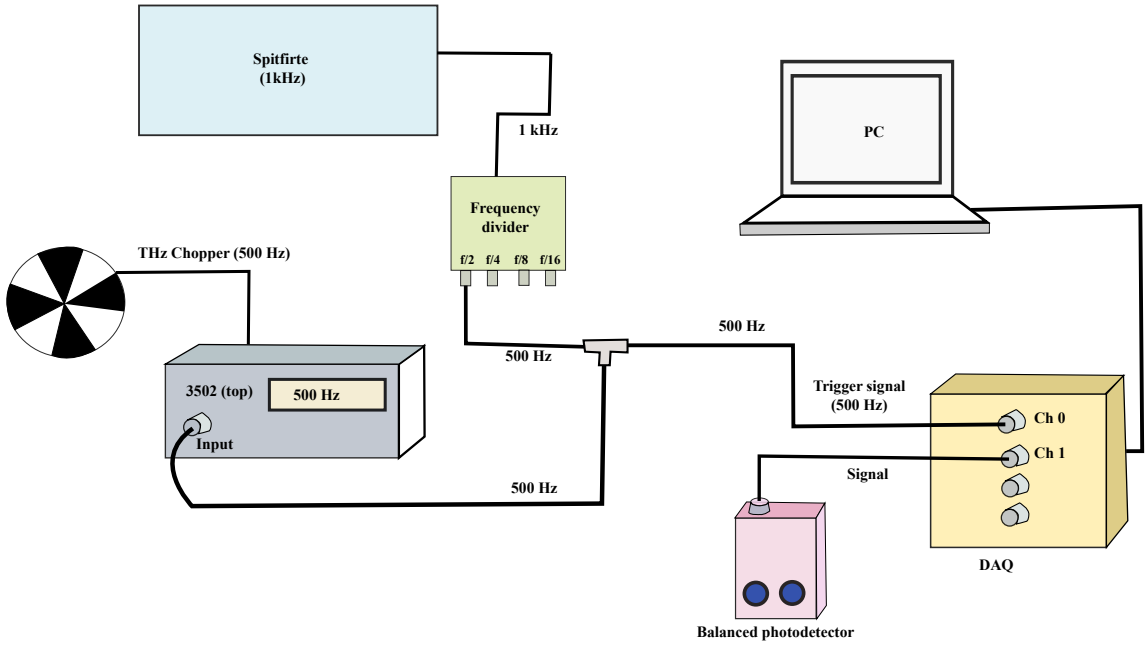

Figure 2.15: The connection diagram of DAQ for THz-TDS experiment.

2.5.2 DAQ for pump-THz probe

By adding an appropriate pump beam into the THz-TDS set-up, we can perform a pump-THz probe experiment. In this case, we use the differential chopping technique, where the DAQ is triggered by 250 Hz TTL signal, and the THz and pump beams are chopped by 500 Hz and 250 Hz, respectively. The temporal sequence is shown in Fig.(2.16). The DAQ treats four milliseconds as a period since it's triggered by 250 Hz:

1. Gate, THz probe and pump beams are all allowed. The signal on the balanced signal consists of the pumped THz probe signal $E_{probe\,w/\,pump}$, background E_{bkg}, and pump scattering signal δE_{pump}[4]. The integrated signal is $A_1 = E_{probe\,w/\,pump} + E_{bkg} + \delta E_{pump}$.

[4]For THz pump, light scattered into the EOS crystal will yield a big signal, so it's crucial to subtract it from the main signal. For pump wavelength that cannot be detected by the EOS crystal, the scattering is negligible.

2. THz probe is blocked by the optical chopper. The signal consists of the pump scattering and background: $A_2 = E_{bkg} + \delta E_{pump}$.

3. The pump beam is blocked by the optical chopper. The signal consists of the unpumped THz probe and background. Integrated signal $A_3 = E_{probe\,w/o\,pump} + E_{bkg}$.

4. Both the THz probe and pump beams are blocked. The signal is the balanced output from the photodetector. Integrated signal $A_4 = E_{bkg}$.

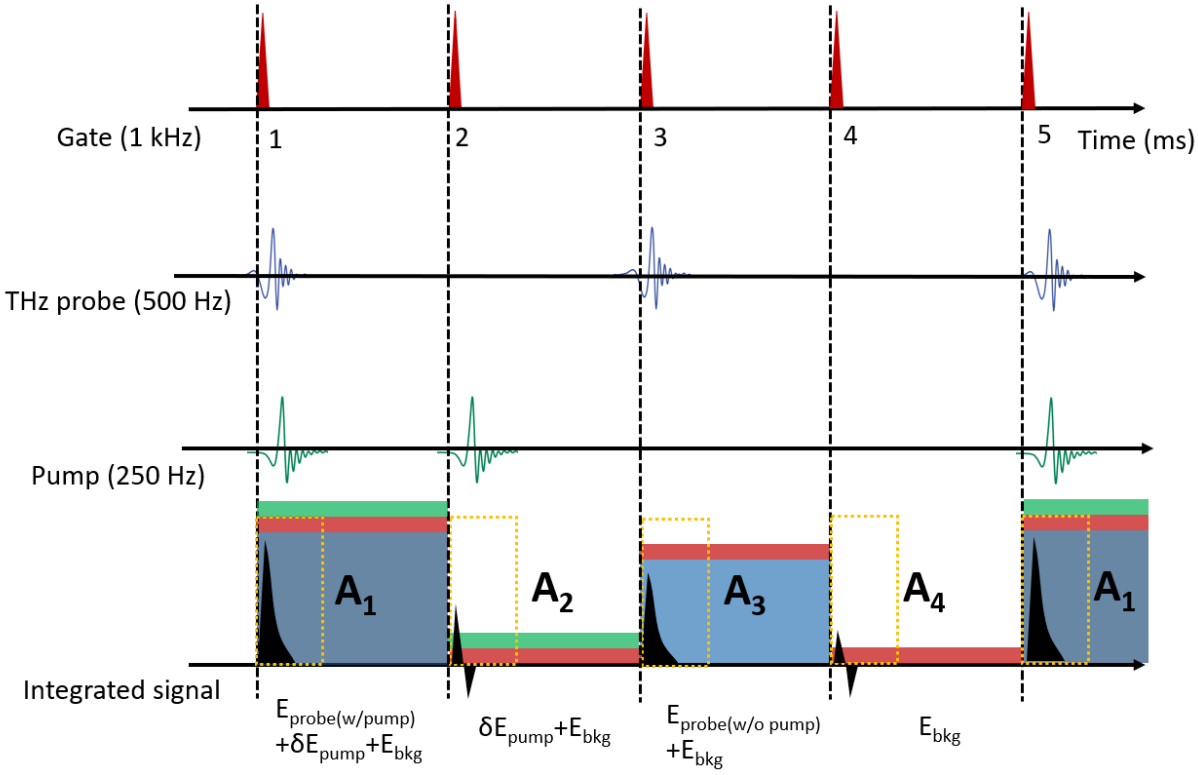

Figure 2.16: Temporal sequence of data taking for pump-THz-probe experiments using DAQ. Red pulse: gate beam, 1 kHz; blue pulse: THz probe, 500 Hz; green pulse: pump pulse, 250 Hz. The black signal at the last row is the balanced photodetector signal digitized by DAQ. The orange rectangle shows the boxcar window that sums over the desired data points to get the integrated signal for each millisecond. Shaded areas show the integrated signal: dark blue: the pumped THz probe signal; red: background; green: pump scattering; light blue: unpumped THz probe.

We can obtain all of the information for the pump-probe measurement by doing simple algebra of the four integrated signals. The unpumped THz probe signal: $E_{probe\,w/o\,pump} = A_3 - A_4$;

the pumped-THz probe signal: $E_{probe\,w\,pump} = A_1 - A_2$. So the pump-induced change of the THz probe:

$$dE_{pump-probe} = E_{probe\,w/\,pump} - E_{probe\,w/o\,pump} = A_1 - A_2 - A_3 + A_4 \tag{2.19}$$

and the pump-probe signal

$$\frac{dE_{pump-probe}}{E_{probe}} = \frac{A_1 - A_2 - A_3 + A_4}{A_3 - A_4}. \tag{2.20}$$

The DAQ has the advantage over a single lock-in amplifier in that pulse by pulse pump-probe signal is recorded. Any short or long term drift of the signal will be corrected. For THz-pump-THz-probe experiment, intense THz pump scattered into the EOS crystal can overwhelm the THz probe. With the help of DAQ and differential choppping, a weak THz probe signal can be extracted (Eq.(2.20)).

The connection diagram of DAQ for pump-THz probe is shown in Fig.(2.17).

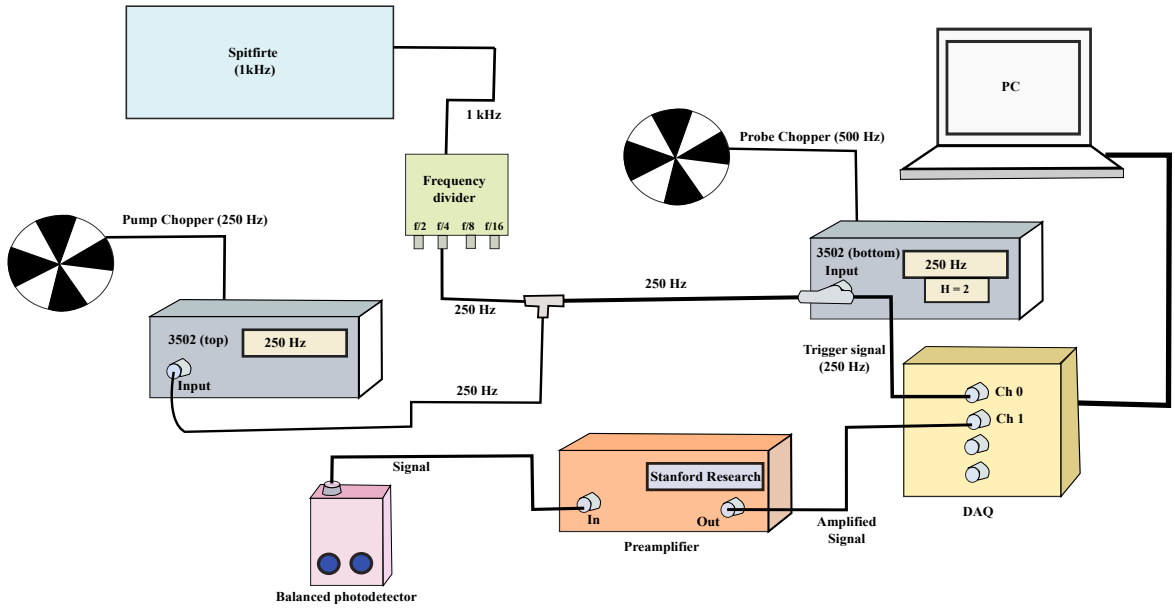

Figure 2.17: The connection diagram of DAQ for THz-TDS experiment.

Chapter 3

Background of Sr_2IrO_4

3.1 Mott-Hubbard model

The band theory is very successful in explaining the electronic properties of insulators, metals and semiconductors. In band theory, band width W is quite large, or in other words, electrons can easily hop between atoms due to the dominance of kinetic energy over Coulomb repulsion. However, in many transition-metal oxides, although d-electrons are partially filled, they are poor conductors [69]. In this case, electrons in neighboring sites are further away, causing on-site Coulomb repulsion to be comparable with or even larger than the kinetic energy. It is not energetically favorable for electrons to hop to another occupied site due to the large Coulomb repulsion. The competing physics between electron itinerancy (hopping) and localization (Coulomb repulsion) leads to rich condensed matter phenomena like metal-insulator transition [70]. A simplified mode to solve this is the Hubbard model with the following Hamiltonian:

$$H = \sum_{i,j;\alpha\beta} t_{ij,\alpha\beta} c^{\dagger}_{i\alpha} c_{j\beta} + h.c. + U \sum_{i,\alpha} n_{i\alpha}(n_{i\alpha} - 1) \tag{3.1}$$

where t is the hopping amplitude, $c_{i\alpha}$ is the annihilation operator for electron in orbital α at site i, $n_{i\alpha} = c^{\dagger}_{i\alpha} c_{i\alpha}$ is the corresponding occupation number, and U is the on-site Coulomb repulsion.

The Hubbard model has successfully explained the metal-insulator transition in 3d transition-metal oxide (TMO) including nickelates, mangnites, vanadium oxides. In those systems, 3d electrons form a strongly correlated narrow band with bandwidth W smaller than strong Coulomb repulsion U [70]. As shown in Fig.(3.1), with a large enough Coulomb repulsion U, the electronic band is split into an upper Hubbard band and lower Hubbard band with a Mott gap of energy U.

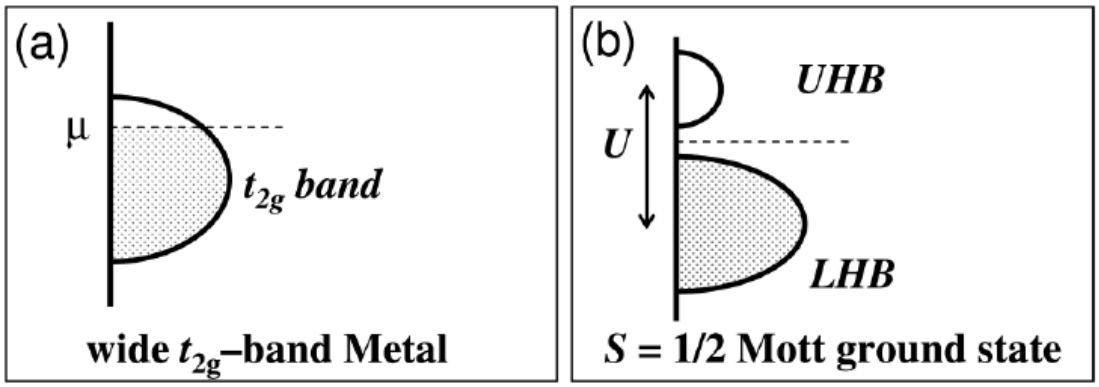

Figure 3.1: From Ref.[71]. Schematic diagram of energy levels of (a) t_{2g} band and (b) t_{2g} band with extremely large Hubbard U.

3.2 Spin-orbit coupled Mott insulator

Recent decades have witnessed nontrivial physics from spin-orbit coupling (SOC), including spintronics [72] and topological insulators (TIs) [73, 74]. SOC is a relativistic interaction of a particle's spin with its motion inside a potential. In semiconductors, SOC allows one to control spins differently. Recently in the fast-growing field of topological materials, SOC plays an essential role. For example, a small gap that protected by time-reversal symmetry is open due to the SOC [75, 76, 77]. Electrons are predicted to transport without back-scattering along edges/surfaces from the spin-momentum locking mechanism. However, most studies are focused on non-interacting systems where the electron-electron correlation is negligible compared with hopping amplitude t and SOC strength λ [73, 74].

Going down the periodic table from 3d to 4d, 5d series, orbitals are more extended, so the Coulomb repulsion U is weaker, leading to less electron-electron correlation. At the same time, with heavier atoms, SOC λ increases dramatically, to an energy scale that is comparable with Coulomb repulsion U.

In this case, an SOC term needs to be included in the Hubbard model (Eq.(3.1)):

$$H = \sum_{i,j;\alpha\beta} t_{ij,\alpha\beta} c^{\dagger}_{i\alpha} c_{j\beta} + h.c. + U \sum_{i,\alpha} n_{i\alpha}(n_{i\alpha} - 1) + \lambda \sum_{i} \mathbf{L}_i \cdot \mathbf{S}_i \tag{3.2}$$

where λ is the atomic SOC strength of spin $\mathbf{S}_i$ and orbital $\mathbf{L}_i$. There are three degrees of freedom in the spin-orbit coupled Hubbard model (Eq.(3.2)): electron hopping amplitude t, Coulomb repulsion U, and SOC strength λ.

The schematic phase diagram of relative interaction as a function of Coulomb repulsion U/t and SOC λ/t is shown in Fig.(3.2). The simple metal or band insulator that is explained well by band theory falls in the left corner of the phase diagram with $U/t \ll 1$ and $\lambda/t \ll 1$. With the increase of relative Coulomb repulsion U/t, we move upwards on the phase diagram and enter the regime of Mott insulator (Sec. 3.1). On the other hand along the x-axis, with the increase of related SOC strength λ/t but at small U/t, we can expect topological insulator/metal states. Interesting phenomena emerge for comparable U/t and λ/t, where the SOC and electron-electron correlation work in a cooperative way. The name coined for materials in this regime are *spin-orbit coupled Mott insulator*. A lot of interesting phases are predicted in this phase including chiral spin liquid [79], axion insulator [80, 81], Weyl semimetal [80, 82, 83], topological Mott insulator [84, 85], quadrupolar [86].

3.3 Iridates: Ruddlesden-Popper series $Sr_{n+1}Ir_nO_{3n+1}$

In 5d-electron systems, iridates are the perfect platform to study the competition between electron-electron correlation and SOC. The SOC strength of 5d TMOs is $\sim$ 0.3-0.4 eV [88], much

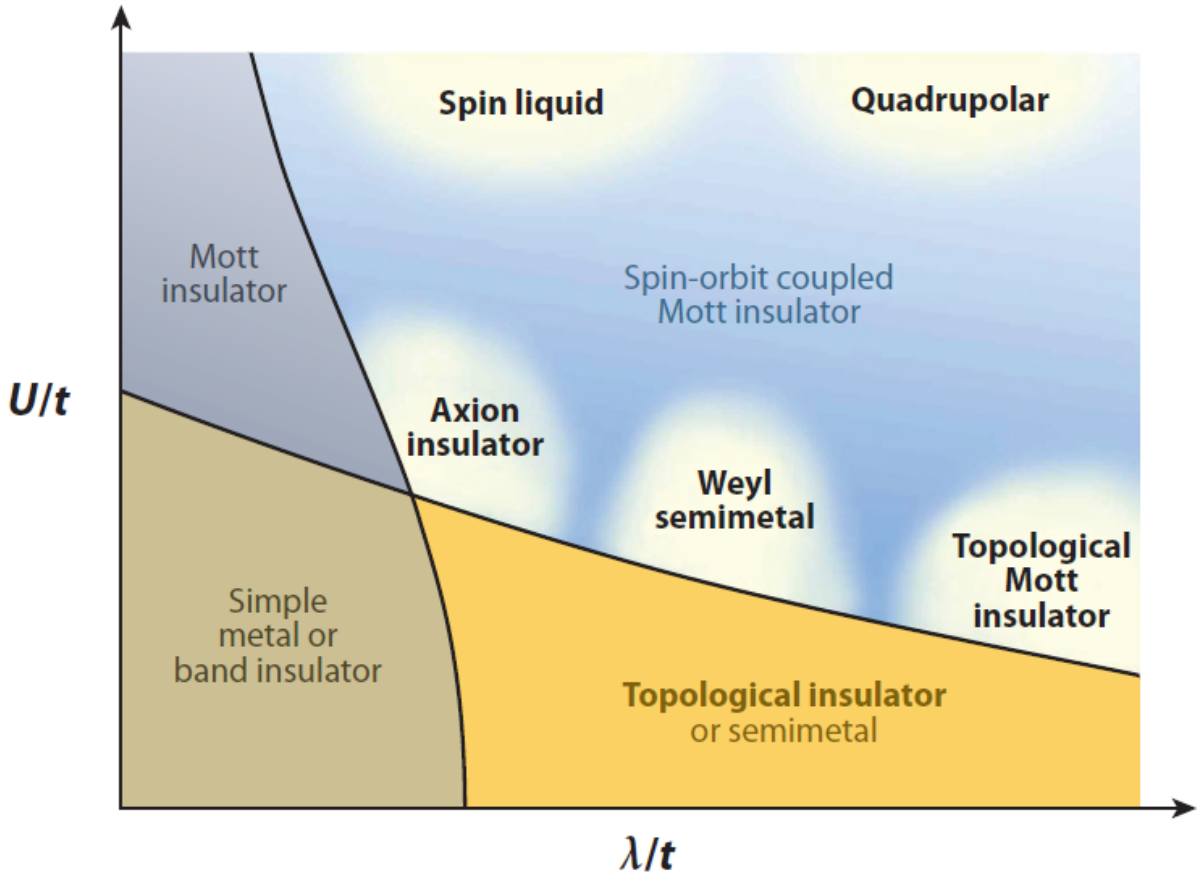

Figure 3.2: From Ref.[78]. Cartoon of phase diagram for electronic materials with respect to interaction strength U/t and spin-orbit coupling λ/t, where t is the hopping amplitude.

larger than that of 3d TMOs (on the order of meV). The Coulomb repulsion U in 5d TMOs is $\sim$ 0.5 - several eV, comparable with the SOC strength, leading to cooperative behavior in 5d TMOs' electronic properties.

For partially filled 5d electrons in TMOs, the atomic energy levels are split by octahedral crystal field into e_g and t_{2g} orbital levels with energy difference 10 Dq. (Fig.(3.3)). We are mostly interested in iridates, where the t_{2g} levels are partially filled with the t_{2g}^5 low-spin configuration. We ignore the e_g level since it is with sufficiently higher energy. The t_{2g} band is further split into pseudo-spin $J_{eff} = 1/2$ doublet and $J_{eff} = 3/2$ quartet bands with SOC taken into consideration. The lower-energy $J_{eff} = 3/2$ state is fully filled with four electrons, while the $J_{eff} = 1/2$ state which is $3\lambda/2$ energy higher than the $J_{eff} = 3/2$ state is partially filled with one electron.

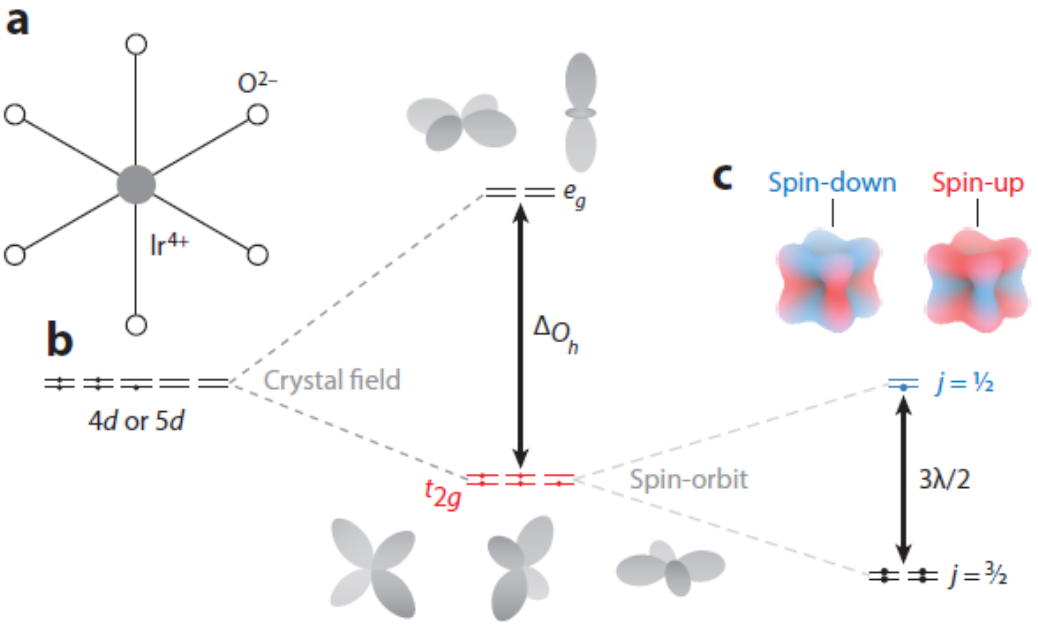

Figure 3.3: From Ref.[87]. (a), octahedral geometry of iridates. (b), Crystal field splitting of 4d or 5d electrons into e_g and t_{2g} levels. (c), Energy splitting and atomic wave functions of t_{2g} into j=1/2 and j=3/2 levels induced SOC λ.

We focus on the 5d Ruddlesden-Popper series $Sr_{n+1}Ir_nO_{3n+1}$ (n = 1, 2, ∞) because it's a perfect platform to study the spin-orbit coupled correlated physics [89]. Assuming z is the number of neighboring Ir atoms, we have z=4, 5, 6 for Sr_2IrO_4, $Sr_3Ir_2O_7$, $SrIrO_3$, respectively. With more neighboring atoms z, the bandwidth W increases, and Coulomb repulsion U decreases. As shown in Fig.(3.4), the strong SOC pseudo-spin model describes the electronic properties of iridates well. However, the $Sr_{n+1}Ir_nO_{3n+1}$ compounds undergo a insulator-to-metal transition as the bandwidth W increases, from Mott insulator Sr_2IrO_4 to barely insulator $Sr_3Ir_2O_7$ to correlated metal $SrIrO_3$.

3.4 Electronic properties of Sr_2IrO_4

Specifically for the spin-orbit coupled Mott insulator Sr_2IrO_4, the electronic properties and optical conductivity are shown in Fig.(3.5). The atomic SOC for Ir atom is $\sim$ 0.4 eV, by

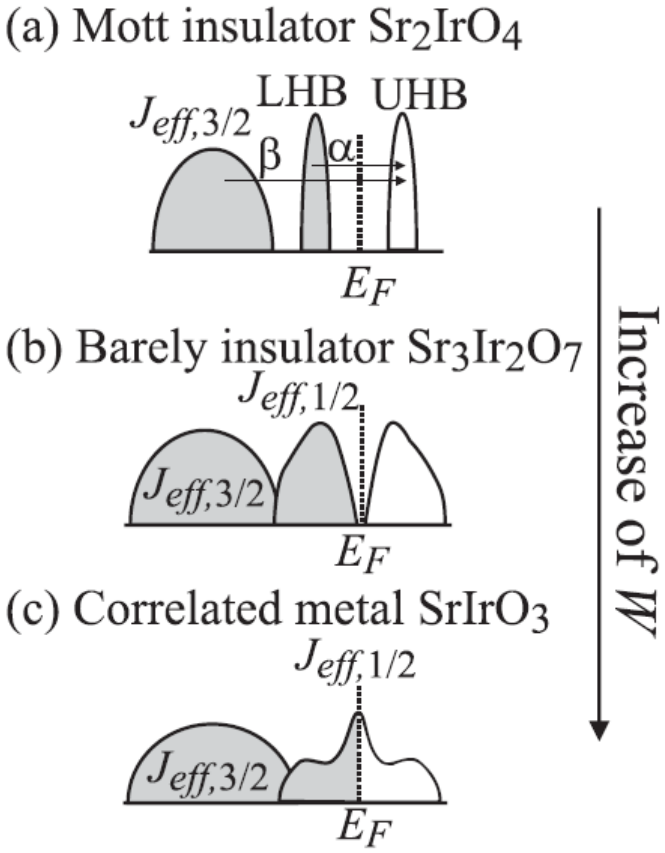

Figure 3.4: From Ref.[89]. Band diagrams of 5d Ruddlesden-Popper series $Sr_{n+1}Ir_nO_{3n+1}$ compounds described by pesudo-spin J_{eff}. (a) Mott insulator Sr_2IrO_4, (b) Barely insulator $Sr_3Ir_2O_7$, (c) Correlated metal $SrIrO_3$.

which the band splits to a narrow band near the Fermi level (see LDA+SOC calculation result [90]). In this case a moderate Coulomb repulsion U $\sim$ 2 eV is big enough to open a charge gap. Without the SOC, the required U would be much bigger $\sim$ 5 eV.

The optical conductivity of Sr_2IrO_4 [91, 92, 93] is shown in the right panel of Fig.(3.5). The α peak corresponds to the transition from $J_{eff} = 1/2$ lower Hubbard band (LHB) to $J_{eff} = 1/2$ upper Hubbard band (UHB), and the β peak corresponds to the transition from $J_{eff} = 3/2$ to $J_{eff} = 1/2$ UHB. The energy of α peak decreases from 0.54 eV at 10 K to 0.44 at 500 K and broadens. The β peak is at $\sim$ 0.93 eV, and does not change too much at different temperatures. The optical gap Δ_{opt} is estimated to be 0.41 eV at 10 K. There are optical phonons below the band gap energy, with the highest phonon energy $\sim$ 82 meV.

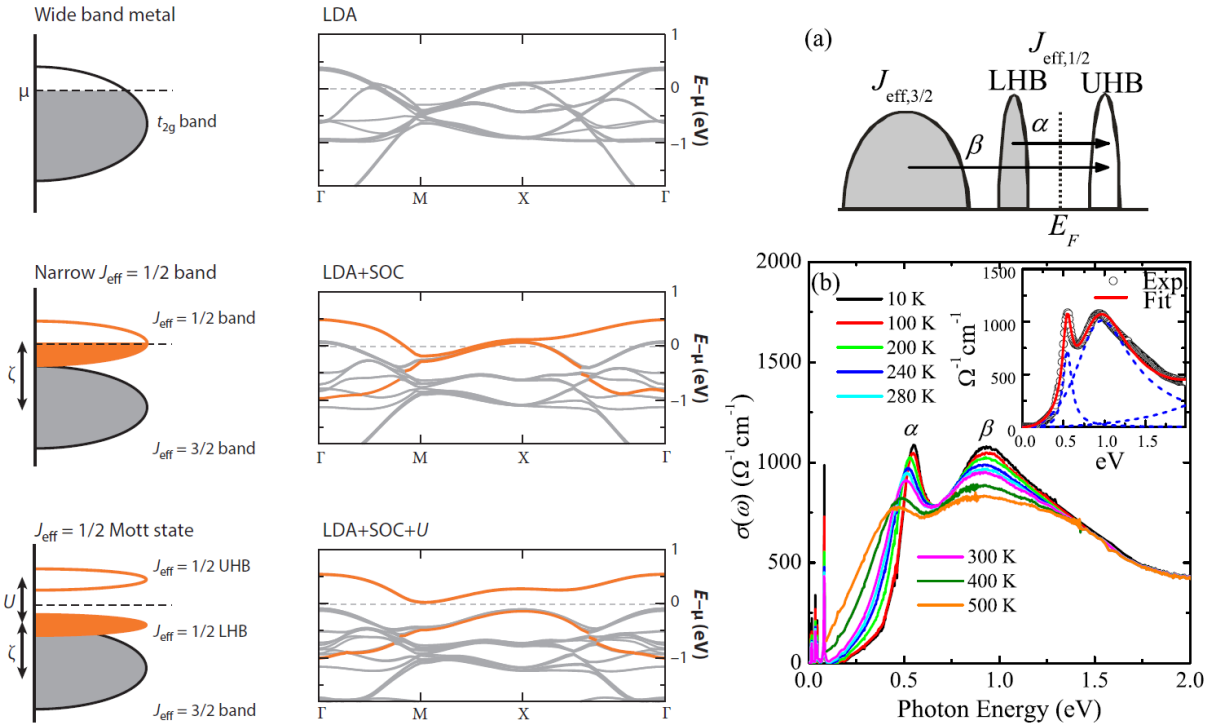

Figure 3.5: From Ref.[90, 91]. Electronic band structure (left and middle figures) and optical conductivity (right figures) of Sr_2IrO_4. Left figures: schematic of SOC-induced Mott insulator. Middle figures: first-principle calculation of band structure of Sr_2IrO_4 with only LDA (local density approximation), LDA+SOC and LDA+SOC+U. Right figures: optical conductivity of Sr_2IrO_4 below 2 eV at different temperatures.

3.5 Magnetic properties of Sr_2IrO_4

Sr_2IrO_4 is the most intensively studied system among the Ruddlesden-Popper series $Sr_{n+1}Ir_nO_{3n+1}$ due to its structural and magnetic similarity to the undoped parent compounds of the high-T_c cuprates such as La_2CuO_4. The cuprate physics can be described as single band spin-1/2 Heisenberg antiferromagnet on a quasi-2D sqaure lattice with strong exchange coupling of J $\sim$ 130 meV [94]. In cuprate, the orbital degeneracy is lifted by Jahn-Teller effect, while for Sr_2IrO_4 it is SOC. Nevertheless they can both be described by an effective spin-1/2 model.

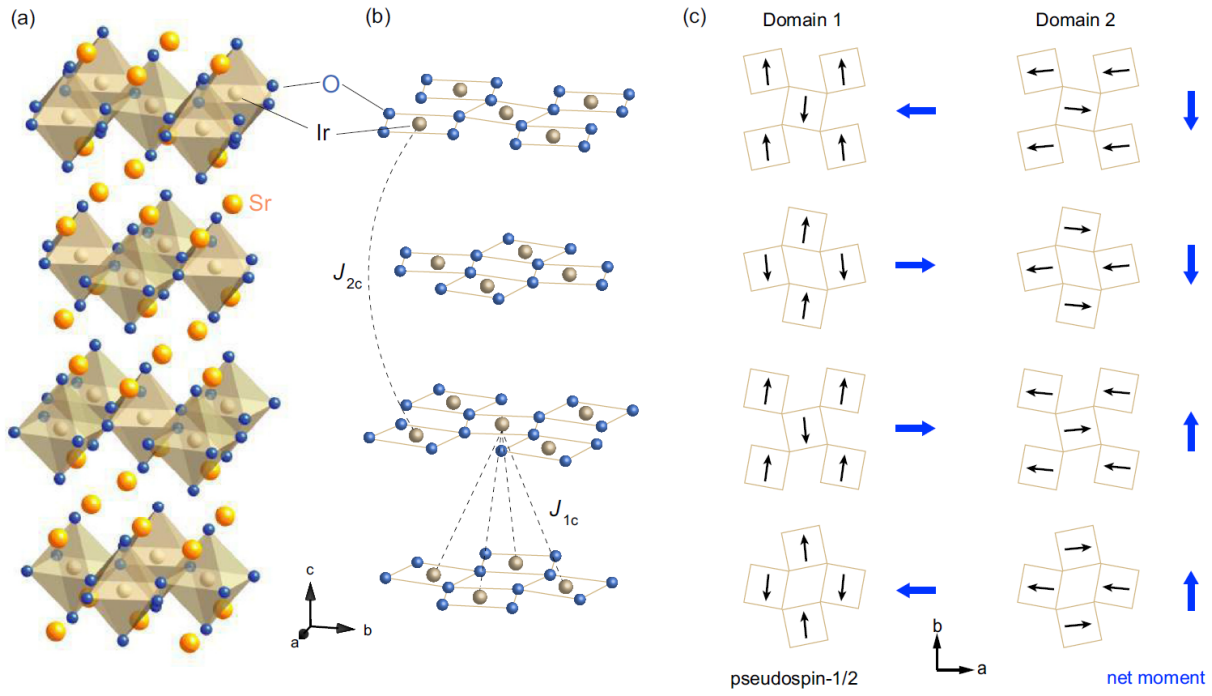

Figure 3.6: From Ref. [95]. Crystal and magnetic structure of Sr_2IrO_4 (a) The crystal structure of Sr_2IrO_4 whose space group is $I4_1/acd$. Each octahedron is rotated by 11.8° about the c axis. (b) The spins of Ir atom are aligned in-plane with the octahedron. Interlayer pseudospin coupling is J_{1c} for nearest layers and J_{2c} for next-nearest layers. (c) The projection of pseudospins on the ab plane. Blue arrows indicate the net moment.

Sr_2IrO_4 undergoes an AFM transition at $\sim$ 230 K. The crystal structure of Sr_2IrO_4 is shown in Fig.(3.6)(a). Its space group is $I4_1/acd$ with each octahedron rotated by 11.8° about the c axis. In the AFM phase, the spins are aligned in ab-plane and titled with the octahedron. There is net ferromagnetic moment in-plane with "left-right-right-left" ($lrrl$) or "down-down-up-

up" (*dduu*) staggered patterns. From resonant magnetic x-ray scattering (RMXS) results [95], the population of two different domains *uddu* and *uudd* are evenly distributed. With external magnetic field of $H_c > 0.2$ T, there is a metamagnetic transition that aligns in-plane moments with the field (stack pattern *uuuu*).

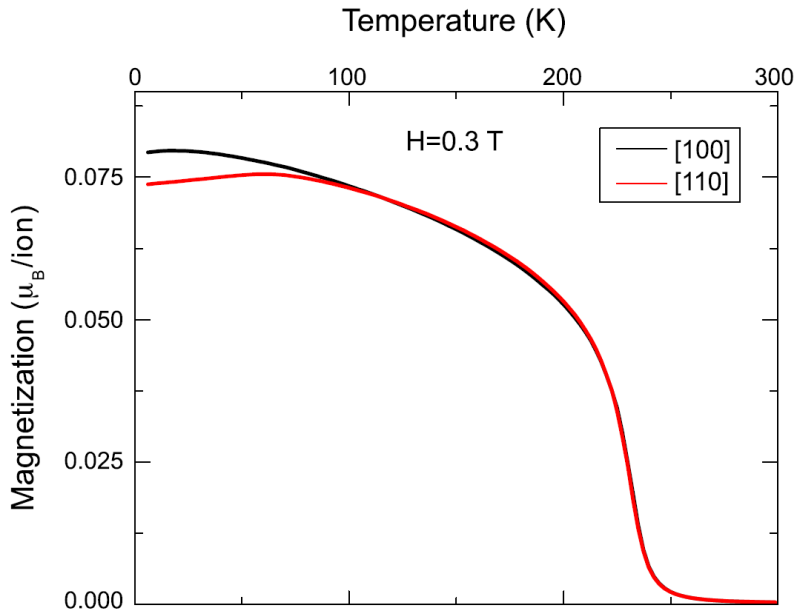

Figure 3.7: From Ref. [95]. Magnetization of Sr_2IrO_4 as a function of temperature along [100] (black) and [110] (red) as external magnetic field of 0.3 T taken at 5 K.

The magnetism along [100] and [110] with an external magnetic field of 0.3 T as a function of temperature is shown in Fig.(3.7). The magnetic phase transition occurs at $T_N \sim 230$ K, showing an order-parameter-like upturn. The magnetization keeps increasing as the external magnetic field is strong enough to fully align the spins along [100], consistent with weakly ferromagnetic behavior that magnetization at low temperature keeps increasing. The decrease of the magnetization at low temperature along [110] indicates a temperature-dependent magnetic anisotropy, which is crucial in understanding the magnetic excitation in Sr_2IrO_4. A measurement using optical second-harmonic generation also observed a hidden non-dipolar magnetic order, whose transition temperature is similar as the AFM transition in the parent compound Sr_2IrO_4, but higher for hole-doped $Sr_2Ir_{1-x}Rh_xO_4$ [96].

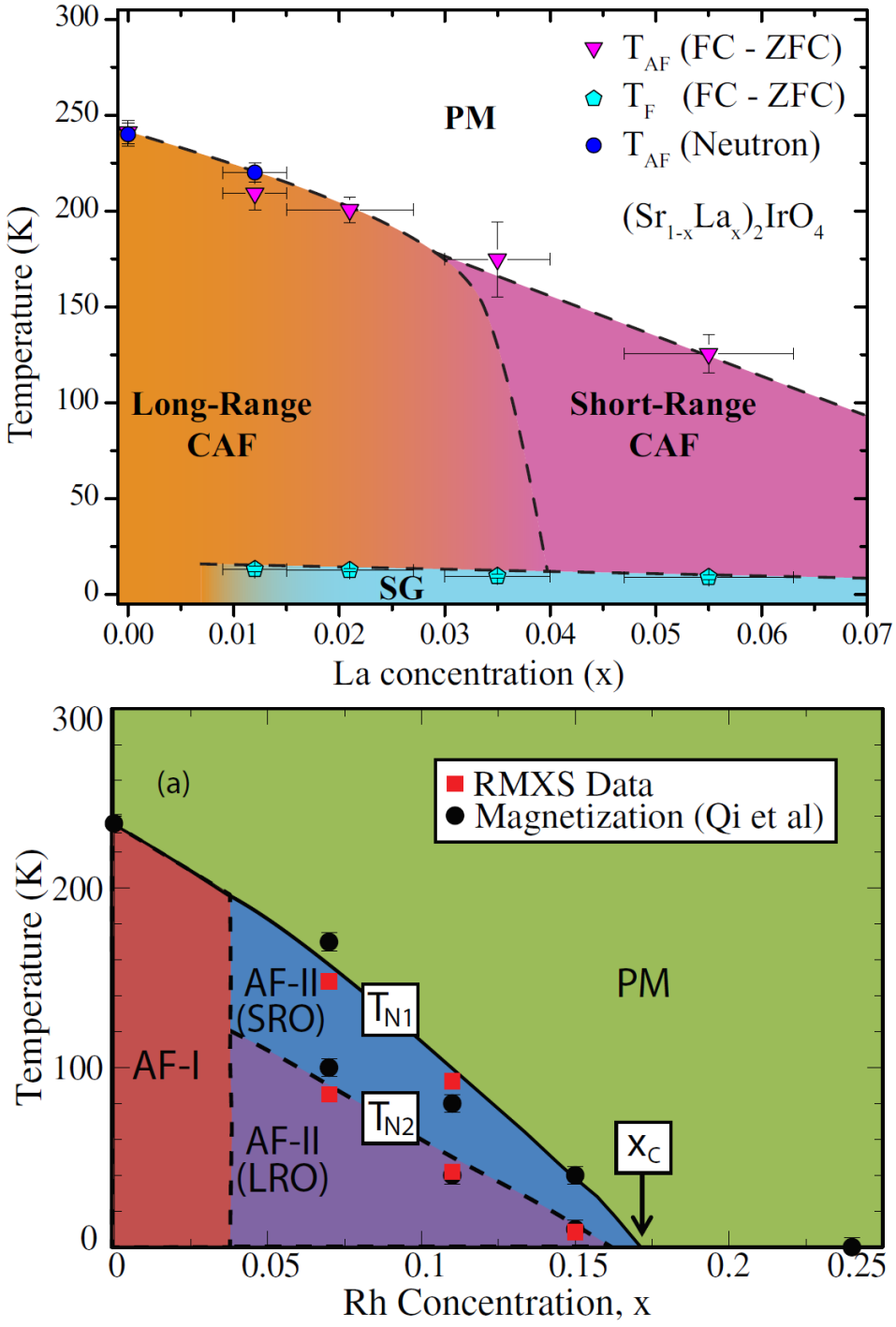

Figure 3.8: Magnetic phase diagram of electron (La) doped- (top figure) [97] and hole (Rh) doped- (bottom figure) [98] Sr_2IrO_4.

Besides the parent compound Sr_2IrO_4, the magnetic properties of hole-doped $Sr_2Ir_{1-x}Rh_xO_4$ and electron-doped $(Sr_{1-x}La_x)_2IrO_4$ have been studied extensively. For electron-doped $(Sr_{1-x}La_x)_2IrO_4$ (Fig.(3.8) top figure), neutron scattering and magnetization measurements [97] show that long-range AFM magnetic order is suppressed beyond $x \approx 0.2$, while persistent short-range AFM magnetism survives up to the La doping limit $x \approx 0.6$. The electronic ground state exists as an inhomogeneous separated phase. At low temperature, a spin glasslike state is observed. For hole-doped $Sr_2Ir_{1-x}Rh_xO_4$, there are three magnetic phases: AF-I, AF-II (short-range-ordered), and AF-II (long-range-ordered) characterized by transition temperatures T_{N1}, T_{N2}. The magnetic order totally disappears at Rh doping $x_c \sim 0.17$.

3.6 Resonant inelastic X-ray scattering (RIXS)

Resonant inelastic X-ray scattering (RIXS) is a fast growing spectroscopic technique that uses high energy X-ray inelastic scattering from a material [99]. This photon-in photon-out spectroscopy measures the energy/momentum change of the scattered X-ray which is transferred into the intrinsic excitations of the material. Beyond other condensed matter experimental techniques like neutron scattering, Raman spectrosopy, in RIXS both the energy and momentum information of elementary excitations (phonons, magnons, excitons, charge transitions etc.) is obtained. Also one can utilize the polarization of the photon to allow various selection rules of transitions. RIXS is a resonant technique in that the energy of the X-ray is chosen to be resonant to one of the atomic X-ray absorption edges in order to enhance the inelastic scattering cross section.

The RIXS process can be classified as direct or indirect. A direct process is dominant when it's allowed, while the indirect process is higher-order [99]. In the direct process (Fig.(3.9)(a)), an incoming photon excites core-electron into valence band. An electron from a *different* state decays and recombines with the hole, emitting a photon with different momentum and energy.

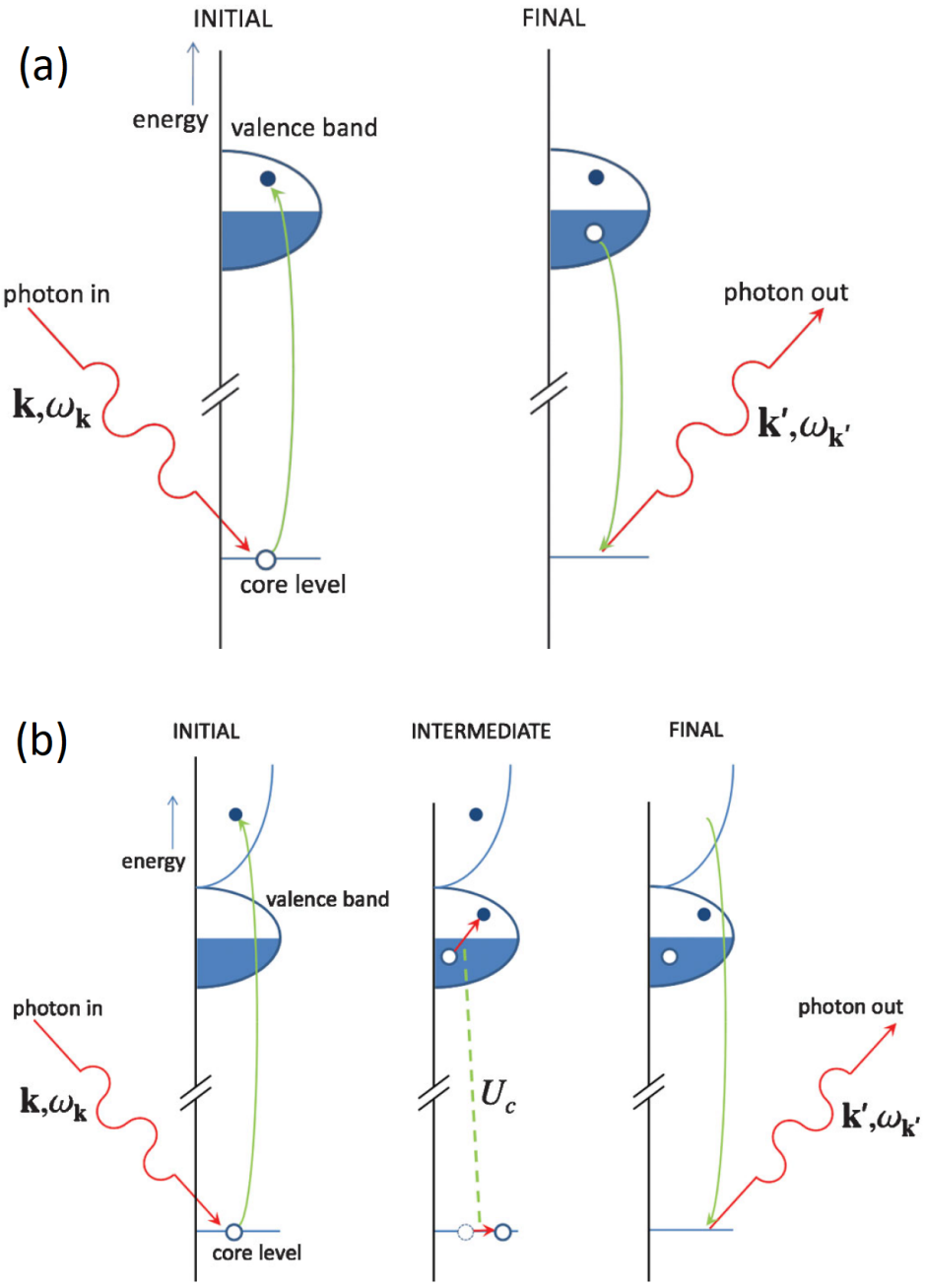

Figure 3.9: Figure adapted from [99]. Incoming x rays with momentum **k** and energy $\omega_{\mathbf{k}}$ incident to excite core electrons. (a) direct RIXS process (b) indirect RIXS process.

In the indirect process (Fig.(3.9)(b)), the incoming photon excites a core-electron to an itinerant state. Excitations are are created through the Coulomb interaction between the core hole and valence electrons. The decay of photo-electrons filling the core-hole and emit photon with energy and momentum difference corresponding to the intermediate excitations.

3.7 Magnetic excitations of Sr_2IrO_4

The magnetic excitation of Sr_2IrO_4 can be revealed by RIXS spectroscopy, where both energy and momentum can be resolved. There are three major features (Fig.(3.10)): magnons with a bandwidth of $\sim$ 200 meV, dispersing from magnetic zone center (π,π); optically forbidden spin-orbit exciton from 0.4 eV - 0.8 eV; electron-hole continuum above 0.4 eV.

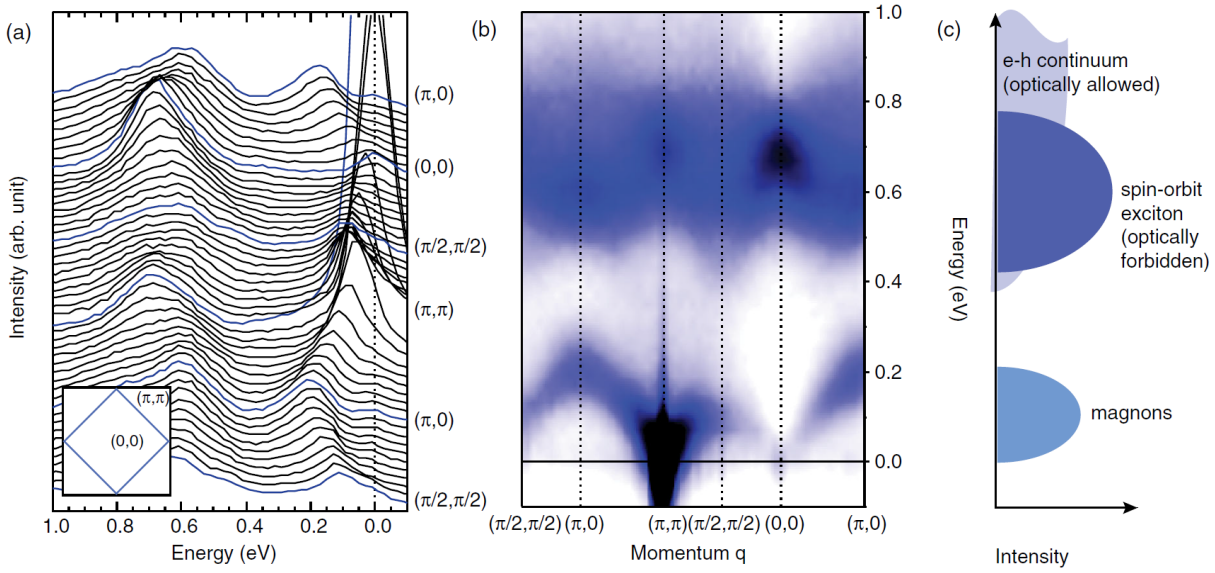

Figure 3.10: From [100]. RIXS spectrum of Sr_2IrO_4 (a) Energy loss spectra of Sr_2IrO_4 at 15 K. (b) Density plot of spin spectra. (c) Schematic of the three different excitations.

The Heisenberg-like magnon band of Sr_2IrO_4 is very similar to that of La_2CuO_4 in terms of dispersion and intensity (see Fig.(3.11)). This can be phenomenologically fitted by $J-J'-J''-J_c$ model, where J, J', J'', J_c corresponds to first-, second-, third-nearest neighbor isotropic exchange interaction and four-spin ring exchange interaction. J_c is not considered in Sr_2IrO_4 because

magnons cannot distinguish between ferromagnetic J' and J_c [1]. The energy scale of J, J', J'', J_c for Sr_2IrO_4 and La_2CuO_4 is shown in table 3.1. The downturn of the dispersion along the magnetic Brillouin from $(\pi,0)$ to $(\pi/2, \pi/2)$ in Sr_2IrO_4 is a signature of ferromagnetic J' interaction (negative sign) compared with La_2CuO_4 which is antiferromagnetic. The magnon bandwidth of Sr_2IrO_4 is $\sim$ 200 meV compared with $\sim$ 300 meV [101, 2] in La_2CuO_4 due to the smaller energy scale of hopping t and Coulomb repulsion U. At higher energy using RIXS with better energy resolution, excitonic quasiparticles are observed: excitons dressed with magnons are observed with higher energy-resolution RIXS [102].

Table 3.1: Comparison of energy scale of isotropic exchange interaction between Sr_2IrO_4 [1] and La_2CuO_4 [2].

Energy (meV) / Material	J	J'	J''	J_c
Sr_2IrO_4	60	-20	15	0
La_2CuO_4	143	2.9	2.9	58

In the case of electron doping $(Sr_{1-x}La_x)_2IrO_4$, the 2D short-range paramagnon excitations revealed by RIXS persist well into metallic phase ($\sim$ 10% electron doping), while the long-range 3D magnetic order is rapidly suppressed with increasing x [103, 104, 105].

3.8 Magnetic anisotropy and spin model

Low-energy spin dynamics are crucial to understand the nature of the magnetic anisotropy of Sr_2IrO_4. Magnetic X-ray scattering experiments have contradictory stories: Sr_2IrO_4 can be well described by a 2D isotropic Heisenberg model [106] or anisotropy in Sr_2IrO_4 causes deviations from the Heisenberg model [107]. To directly measure the spin gap, RIXS experiments with better energy resolution discovered spin gaps of $\sim$ 19 meV [105] or $\sim$ 30 meV [102] at $(0,0)$ and $\sim$ 16 meV at $(0,0)$ and (π,π). In electron-doped $(Sr_{1-x}La_x)_2IrO_4$, the energy of both spin gaps are robust upon electron doping up to 10% [105]. However, in Raman experiments, a spin wave

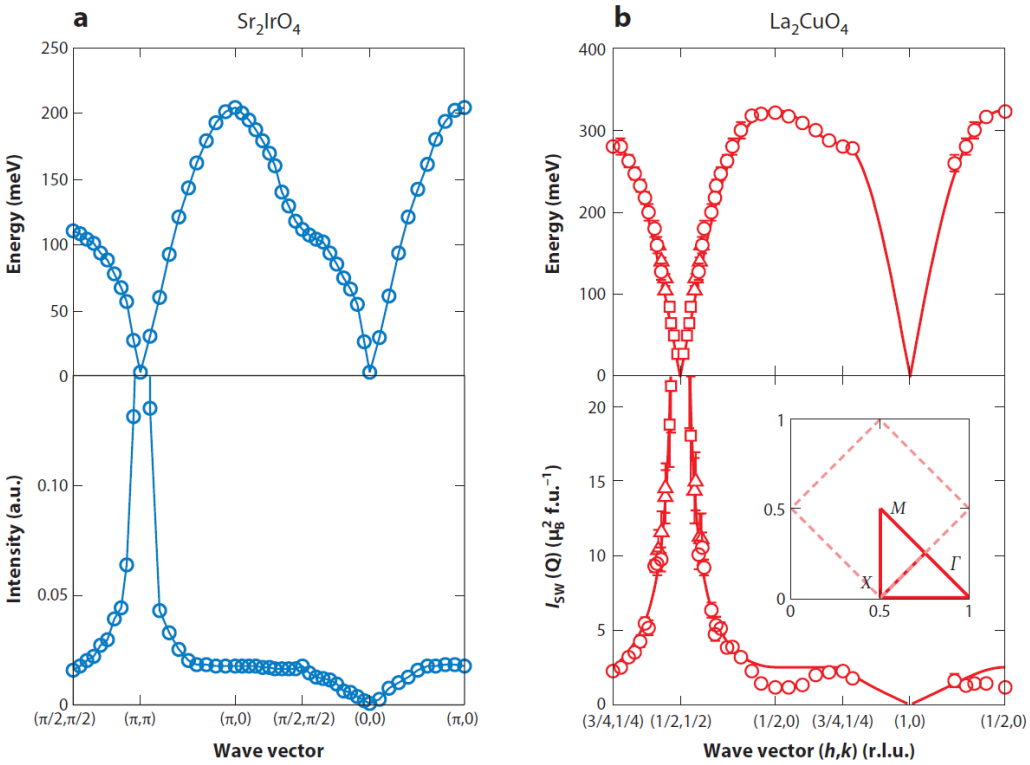

Figure 3.11: RIXS spectra of the magnon dispersion in Sr_2IrO_4 and La_2CuO_4 from [90]. Magnon dispersion and intensity in (a) Sr_2IrO_4 and (b) La_2CuO_4 measured with RIXS.

with energy of ~ 2.4 meV was observed [108, 109]. As shown in Fig.(3.12) top figure, the energy of the magnon moves to lower energy then to higher energy while the in-plane external magnetic field increases, which is consistent with the weak ferromagnetic meta-magnetic transition [108]. For electron-doped $(Sr_{1-x}La_x)_2IrO_4$ (Fig.(3.12) bottom), the magnon peak broadens and the onset temperature of is lower than T_N in undoped samples.

It is known from later theoretical studies [110] and inelastic neutron scattering/RIXS measurements [95] that the spin gap at $(0,0)$ is ~ 40 meV and out-of-plane, while the one at (π,π) is ~ 2 meV and in-plane. However in La_2CuO_4, the out-of-plane spin gap is much smaller ~ 2.5 meV and the in-plane gap is comparable ~ 1 meV.

In the following, we provide a detailed spin model of Sr_2IrO_4 to explain various magnetic phenomena. The energy hierarchy and magnetic anisotropy in Sr_2IrO_4 determine its quasi-2D nature and in-plane, out-of-plane low-energy spin gaps. The dominant magnetic interactions in

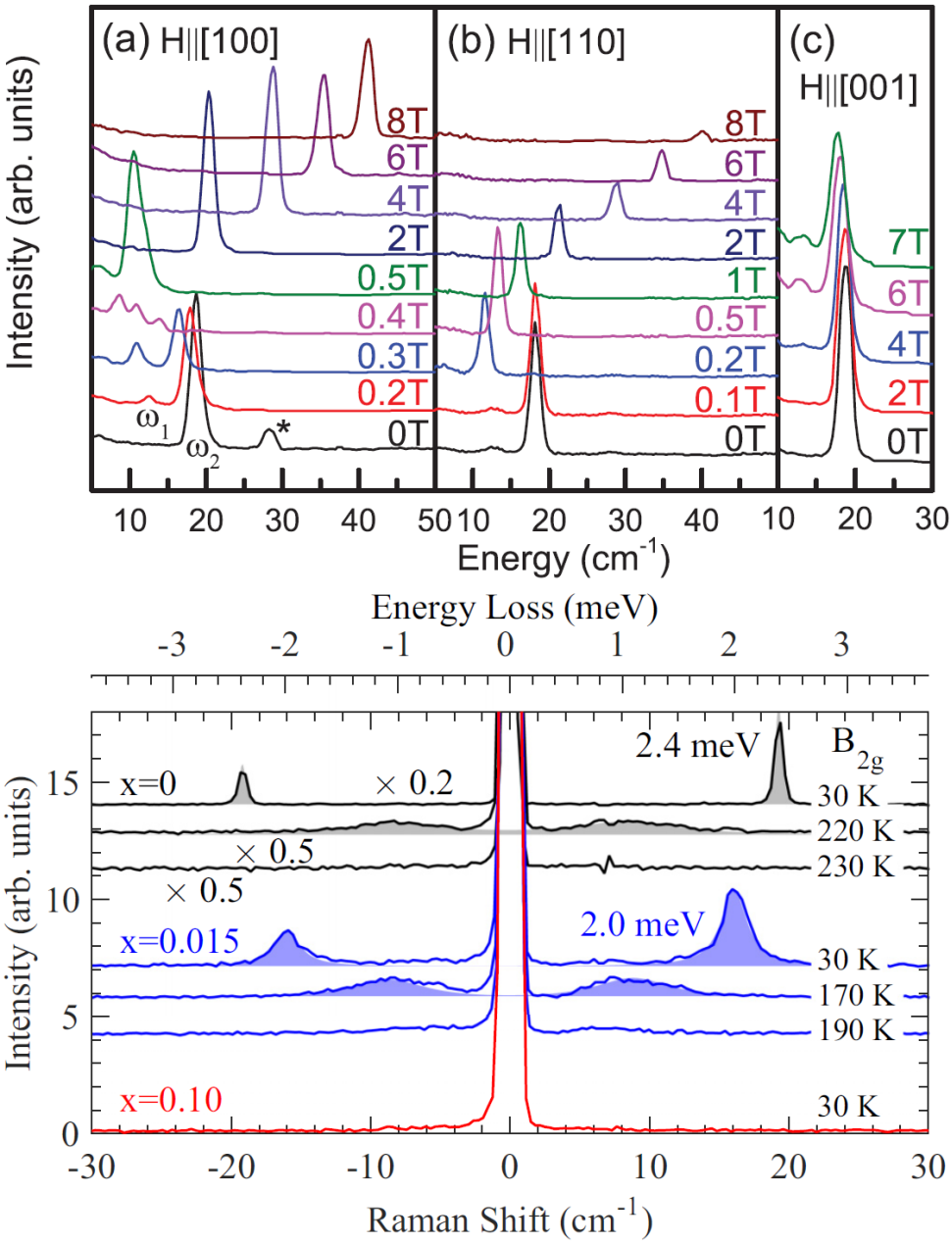

Figure 3.12: Figure on top: from Ref.[108], magnetic field dependence of the Raman spectra of the B_{2g} magnon measured at 3 K of Sr_2IrO_4 for (a) H ∥ [100], (b) H ∥ [110] and (c) H ∥ [001]. Figure at bottom: from Ref.[109], Raman spectra of the B_{2g} magnon in $Sr_{2-x}La_xIrO_4$ at selected temperatures.

Sr_2IrO_4 are isotropic Heisenberg interactions:

$$H_{iso} = \sum_{\langle ij \rangle} J_{ij}\vec{S}_i \cdot \vec{S}_j + J_{1c}\vec{S}_i \cdot \vec{S}_j + J_{2c}\vec{S}_i \cdot \vec{S}_j \tag{3.3}$$

where $\vec{S}_i$ is the pseudospin at site i, J_{ij} consists of first-(J), second-(J'), third-(J'') in-plane nearest neighbor interactions. J_{1c} and J_{2c} are the first- and second-nearest interlayer coupling. J_{2c} is responsible for the staggered pattern formed out-of-plane in Sr_2IrO_4.

Further, there are symmetric and Dzyaloshinsky-Moriya (DM) antisymmetric interactions introduced by tetragonal distortion and octahedra rotation:

$$H_{ani} = \sum_{\langle ij \rangle} J_z S_i^z S_j^z + \vec{D} \cdot (\vec{S}_i \times \vec{S}_j) \tag{3.4}$$

where J_z is the Ising interaction, $\vec{D}$ is the DM vector along c-axis. The DM interaction gives rise a spin canting angle $\phi \approx 13°$. The anisotropic interaction Eq.(3.4) locks the pseudospin in-plane and induces the out-of-plane gap [111] $\Delta_{out} \simeq 4S\sqrt{2J(D\tan\phi - J_z)}$.

To explain the in-plane spin gap, one needs to include the pseudospin-lattice coupling [110]:

$$H_{sp-lat} = \sum_{\langle ij \rangle} \Gamma_1 \cos 2\theta (S_i^x S_j^y + S_i^y S_j^x) - \Gamma_2 \sin 2\theta (S_i^x S_j^x - S_i^y S_j^y) \tag{3.5}$$

where x, y are the directions along the Ir-O bonds and Γ_1, Γ_2 are the energy of pseudospin-lattice coupling to distortion along the [100] and [110] directions. This Hamiltonian gives rise to the in-plane gap of ~ 2 meV. The pseudospin-lattice coupling is induced by pseudo-Jahn-Teller (JT) effect [110]. The JT effect couples the orbital degrees of freedom with the lattice (orbital-lattice coupling), lifting the degeneracy of electronic ground state by a geometrical distortion. It is an important mechanism of spontaneous symmetry breaking in molecular and solid-state systems [112]. In spin-orbit coupled Mott insulator Sr_2IrO_4, orbitals couple strongly with spins, so the pseudospin $J_{eff} = 1/2$ needs to be considered, leading to the pseudo-JT effect. It is predicted that

the pseudo-JT effect induces the tetragonal-to-orthorhombic structural transition, and is crucial in understanding the metamagnetic transitions and the in-plane magnon gaps in Sr_2IrO_4. The pseudospin-lattice coupling (Eq.(3.5)) opens an in-plane spin gap of $\Delta_{in} \simeq 8S\sqrt{J\Gamma_1}$, with the estimation of $\Gamma_1 \sim 2.7\mu eV$ [95, 110].

Table 3.2 summarizes the interaction strength of the spin model. The fact that the in-plane isotropic interactions (J, J', J'') are much stronger than the interlayer coupling (J_{1c}, J_{2c}) is consistent with the quasi-2D magnetic behavior of Sr_2IrO_4. Although the pseudospin-lattice coupling strength is very small, it is crucial in understanding the low-energy magnetic dynamics.

Table 3.2: Spin model parameters of Sr_2IrO_4.

Parameters	J	J'	J''	J_{1c}	J_{2c}	J_z	D	Γ_1
Energy (meV)	57	-16.5	12.4	16.4×10^{-3}	-6.2×10^{-3}	2.9	28	2.7×10^{-3}

3.9 Ultrafast dynamics of magnetic correlations in the photo-doped Mott insulator Sr_2IrO_4: time-resolved magnetic resonant inelastic X-ray scattering

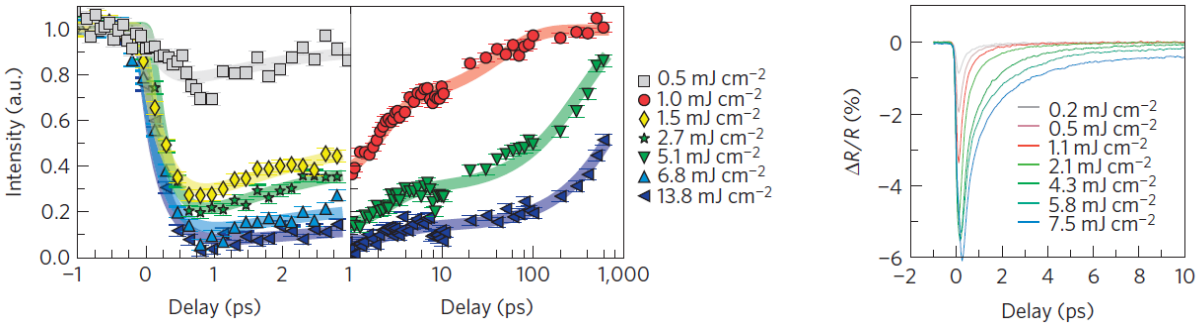

Figure 3.13: From Ref.[113]. 3D magnetic and charge recovery dynamics in Sr_2IrO_4 after 2 μm excitation. Left: dynamics of the intensity of the magnetic Bragg peak (-3, -2, 28) at different pump fluences. Right: 800 nm optical reflectively change ($\Delta R/R$) at different pump fluences.

The study of how magnetic correlation dynamics evolve after photo-doping is crucial

to understand ultrafast magnetism in Sr_2IrO_4. Thanks to the development of time-resolved magnetic resonant inelastic X-ray scattering (tr-RIXS), energy- and momentum-resolved magnetic dynamics across the entire Brillouin zone can be measured. The work by M.P.M. Dean et al. [113] reveals distinct recovery timescales between the two-dimensional (2D) in-plane Néel correlation and three-dimensional (3D) long-range magnetic correlation, which indicates that the dimensionality of magnetism is very important to understand ultrafast magnetic dynamics.

The pump wavelength used to excite quasiparticles is 2 μm, which corresponds to the transition from $J_{eff,1/2}$ band to upper Hubbard band (Fig.(4.1)). Different probing wavelength and techniques were used to monitor different dynamics after the excitation:

- X-ray scattering of the (-3, -2, 28) magnetic Bragg peak: 3D magnetic order dynamics
- 800 nm optical reflectively ($\Delta R/R$): charge dynamics
- tr-RIXS: 2D magnetic correlation dynamics

The results of 3D magnetic dynamics and charge dynamics are shown in Fig.(3.13). The 3D magnetic order is destroyed at fluences $\geq$ 5 mJ cm^{-2}, and recovers on the order of hundreds of picoseconds, while charge recovery is much faster, on the order of several picoseconds. It suggests that 3D magnetic order is independent of the charge dynamics.

The tr-RIXS technique allows the detection of the dynamics of the magnetic quasiparticle spectrum across the entire Brillouin zone. Beyond the 3D magnetic order measured by techniques like X-ray Bragg scattering, X-ray magnetic dichroism, etc., RIXS is able to capture the 2D short-range magnetic correlations. The equilibrium spin spectrum of Sr_2IrO_4 is shown in Fig.(3.14)(a). The $\mathbf{Q}$-points of interest are $(0,\pi)$ and (π,π). The dynamics after the pump at equilibrium and 2 ps after the pump at $(\pi,0)$ is shown in Fig.(3.14)(b). Although the 3D magnetic order is totally destroyed at this pump fluence, the magnon spectra remain well-defined after the pump. Due to the relatively weak c-axis exchange interaction, the magnons are mostly sensitive to the 2D Néel correlations. For magnons at $\mathbf{Q} = (\pi,0)$, there is no change in terms of the dispersion between the

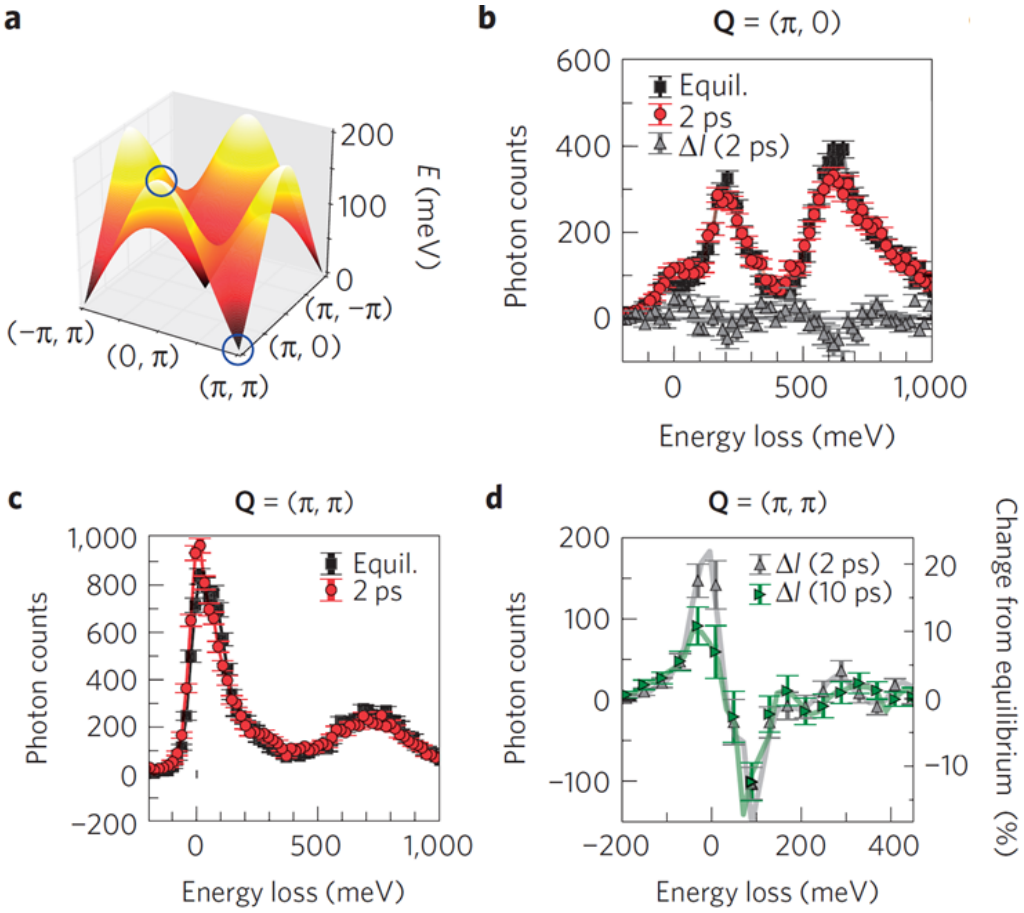

Figure 3.14: From Ref.[113]. (a), Equilibrium spin spectrum of Sr_2IrO_4. (b)(c), tr-RIXS spectra at $\mathbf{Q} = (\pi, 0)$ and $\mathbf{Q} = (\pi, \pi)$ in equilibrium (50 ps after the photo-exictation) and 2 ps after the photo-excitation of 6 mJ cm^{-2}. (d), Intensity difference spectra ΔI between the equilibrium state and 2 ps, equilibrium state and 10 ps after the photo-excitation.

equilibrium and 2 ps after the pump. On the other hand, there is a noticeable change at $\mathbf{Q} = (\pi, \pi)$ after the pump (see Fig.(3.14)(d)), with the decrease of intensity around $\sim$ 100 meV and increase of intensity at very low energy. The recovery time scale of the increase around low energy is faster than at 100 meV. This suggests the high-energy magnon around 200 meV at $(0, \pi)$ is more robust towards than the lower-energy magnon at (π, π). This can be explained by the fact that higher-energy magnons can decay into the lower-energy magnons via multi-magnon emission.

Further analysis shows that the 2D magnetic recovery time scale is similar to the decay time of the charge dynamics. This distinct difference of time scale for 2D and 3D magnetic correlations shows the intrinsic magnetic dimensionality nature of the Sr_2IrO_4. The dynamics of 2D magnetic correlation is closely tied to charge excitation and relaxation, while the 3D magnetic order is more about how the energy dissipates from the spin system to environment (lattice).

Chapter 4

Ultrafast magnetic control in Sr_2IrO_4

4.1 Introduction

The spin-orbit coupled Mott insulator Sr_2IrO_4 has attracted considerable attention because of its exotic $J_{eff} = 1/2$ Mott state due to the interplay of the on-site Coulomb U interaction and strong spin-orbit coupling. It is especially important to investigate how the magnetic ground states evolve following excitation with ultrafast photoexcitation.

In strongly correlated materials, both the Coulomb interaction and spin-orbit coupling play important roles in determining their electronic and magnetic properties. Recently, 5d transition metal oxide iridium oxides (iridates) have attracted a lot of attention because of the comparably strong Coulomb interaction and spin-orbit coupling [87, 78, 114]. Among them, Sr_2IrO_4 as a prototype iridate is very similar to the high-T_c cuprate La_2CuO_4 in structural, electronic, and magnetic properties [71, 115, 116]. The resemblance of exotic phenomena like d-wave gap [117, 118], the emergence of pseudogap [119, 120, 121] upon doping, suggests the possibility of obtaining superconductivity in this compound [122, 123]. The crystal field splits the 5d electron states into t_{2g} and e_g orbitals, then the strong spin-orbit coupling further splits the t_{2g} band to $J_{eff} = 1/2$ and $J_{eff} = 1/2$ bands, leading to a $J_{eff} = 1/2$ Mott insulator with band gap

of 0.5 eV [91]. The magnetic correlation is particularly crucial in forming these exotic states. Sr_2IrO_4 undergoes a paramagnetic (PM) to antiferromagnetic (AFM) transition around $T_N \approx 230$ K [116]. In the AFM phase, the system forms a staggered AFM order with the pattern along c-axis (-++-). The spins are canted in-plane associated with the IrO_6 octahedral rotation, due to the Dzyaloshinsky-Moriya (DM) interaction. With an external in-plane magnetic field of $H_c \approx 0.2$ T, the transition from AFM (-++-) to weakly FM state (++++) occurs. Besides the AFM order, people have found an odd-parity magnetic hidden order in both the undoped Sr_2IrO_4 and the hole-doped Sr_2IrO_4, with the onset temperature monotonically suppressed upon doping level [96, 124, 125].

Using the ultrafast lasers to study and manipulate magnetism on a femtosecond timescale has been very successful [126, 127]. The electromagnetic wave can couple to the spin channel in the material system via its magnetic field [18, 128], modification of the exchange interactions [129, 130], or magnetooptically effect including the inverse Faraday effect (IFE) and inverse Cotton-Mouton effect (ICME) [131, 132, 133, 134, 135, 136, 137]. AFM materials are particularly interesting because the spins dynamics occur on a much faster timescale due to the lack of a net magnetization [138, 139]. However, the lack of microscopic descriptions of the magnetooptical effect limits the potential to effectively generate and control magnetism. Sr_2IrO_4, a typical spin-orbit coupled Heisenberg AFM Mott insulator with a very small in-plane spin gap [108, 109, 95, 110] is a perfect platform to investigate photon-magnon coupling mechanisms and ultrafast manipulation of the magnetic order.

4.2 Ultrafast magnetic control in Sr_2IrO_4: experimental setup

We study the magnetic dynamics of the $J_{eff} = 1/2$ Mott state by time-resolved magneto-optical Kerr effect (tr-MOKE). Circularly polarized pump of two different wavelength are used: mid-Infrared 9 μm (below the charge gap), and near-Infrared 1.3 μm (above the charge gap), as

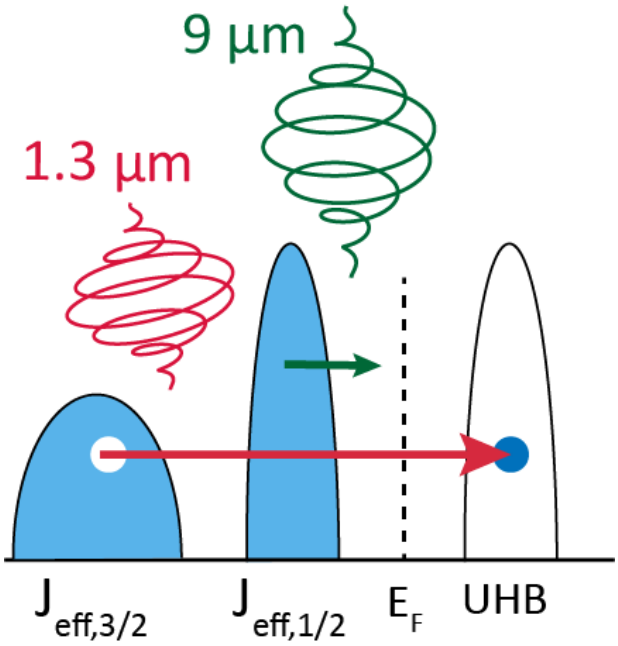

Figure 4.1: Schematic of the experimental configuration. 9 μm pump is non-resonant below the band gap, and above the highest optical phonon. 1.3 μm pump resonantly excites the electrons from $J_{eff,3/2}$ to upper Hubbard band.

depicted in Fig.(4.1)). The resulting magnetization dynamics are monitored using Kerr rotation at 800 nm.

The experimental scheme of how the pump and probe beams impinge upon the sample is shown in Fig.(4.2). Circularly polarized light of opposite helicities are used to pump the Sr_2IrO_4. We use 1.3 μm and 9 μm as the pump wavelength. The 9 μm mid-Infrared beam is generated by mixing two near-infrared beams (1.1 to 2 μm tunable) from the output of a TOPAs-twins in a GaSe crystal. The TOPAs-twins consists of two independently tunable two-stage optical parametric amplifier (OPA) that share the same white light source. It is seeded by 3.5 mJ 800 nm pulses from a Ti: sapphire laser amplifier (total pulse energy, 6 mJ; repetition rate, 1 kHz). The 1.3 μm pump pulses are directly from one of the outputs of the TOPAs-twins. The pump and probe pulses incident on the sample at $\sim 20°$and $10°$. The magnetic dynamics after pump excitation is characterized by the Kerr rotation θ of the 800 nm p-polarized probe along the a-axis of Sr_2IrO_4. The reflected probe pulse propagates through an half-wave plate and a Wollaston

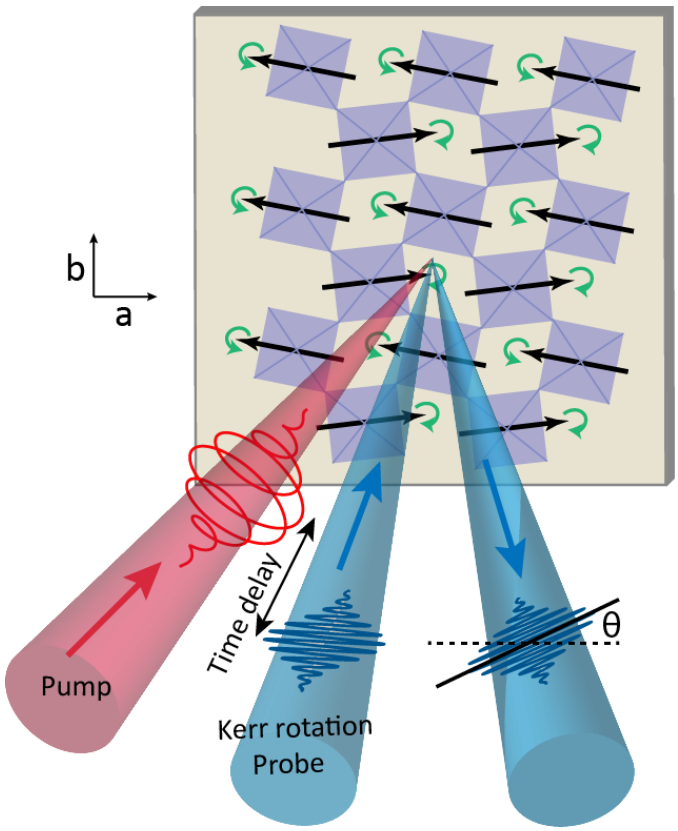

Figure 4.2: Schematic of the experimental configuration. Circularly polarized pump pulse of 9 μm or 1.3 μm (shown in red) are incident on the ab-plane of Sr_2IrO_4 single crystal. Horizontally polarized 800 nm probe pulse (shown in blue) is reflected from the sample, and the time-resolved magneto-optical Kerr effect is measured by the polarization rotation θ of the probe pulse.

prism, hitting on two identical photodiodes. The pump-induced polarization rotation can be measured by the imbalance photocurrent ΔI of the two photodiodes, and the magneto-optical Kerr signal $\Delta I/2I$ ($2I$ is the summation of the photocurrents) is recorded at different time delay between the pump and probe pulses. The Sr_2IrO_4 single crystal is obtained from Prof. Stephen Wilson's group at UCSB. To obtain a fresh and flat surface, we cleaved the sample using ceramic rod and silver epoxy (Fig.4.3). A ceramic rod is glued to the top surface of the sample with silver expoxy. The bottom surface of the sample is similarly glued to the holder. For layered materials with weak van der Waals interlayer coupling, the bonding force of silver epoxy is much stronger, so the sample can be cleaved by hitting the ceramic rod with mechanical force.

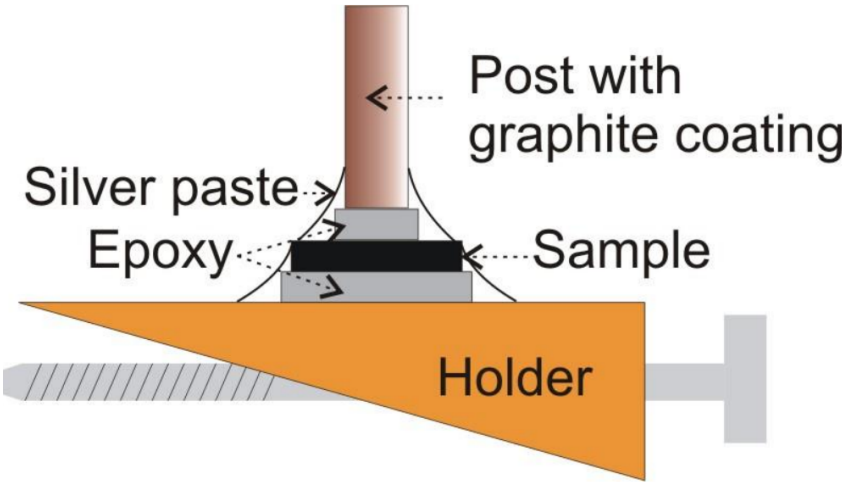

Figure 4.3: From [140]. Sample preparation for cleaving. The sample is sandwiched in between a ceramic rod and the holder by silver epoxy. Hitting the ceramic rod with mechanical force can peel off top layers of the sample, leaving fresh surface.

4.3 Ultrafast magnetic control in Sr_2IrO_4: experimental results

A brief summary of the experimental results are in the following: for both pump wavelength, the 2D in-plane B_{2g} coherent magnon oscillation of frequency 0.5 THz was observed in the pump-induced Kerr rotation signal. The circularly polarized 9 μm pumps of opposite helicities excite oscillations of opposite phase, while 1.3 μm pumps excite oscillations of same phase. The quadratically scaling of the fluence dependent magnon amplitude for the 9 μm pump indicates a novel photon-two-magnon coupling mechanism for the magnon generation. The direct excitation (9 μm) of the spin spectrum without photo-doping electrons allows highly efficient magnon generation, which is almost 10 times better than the resonant 1.3 μm pump. This will be discussed in detail in the following sections.

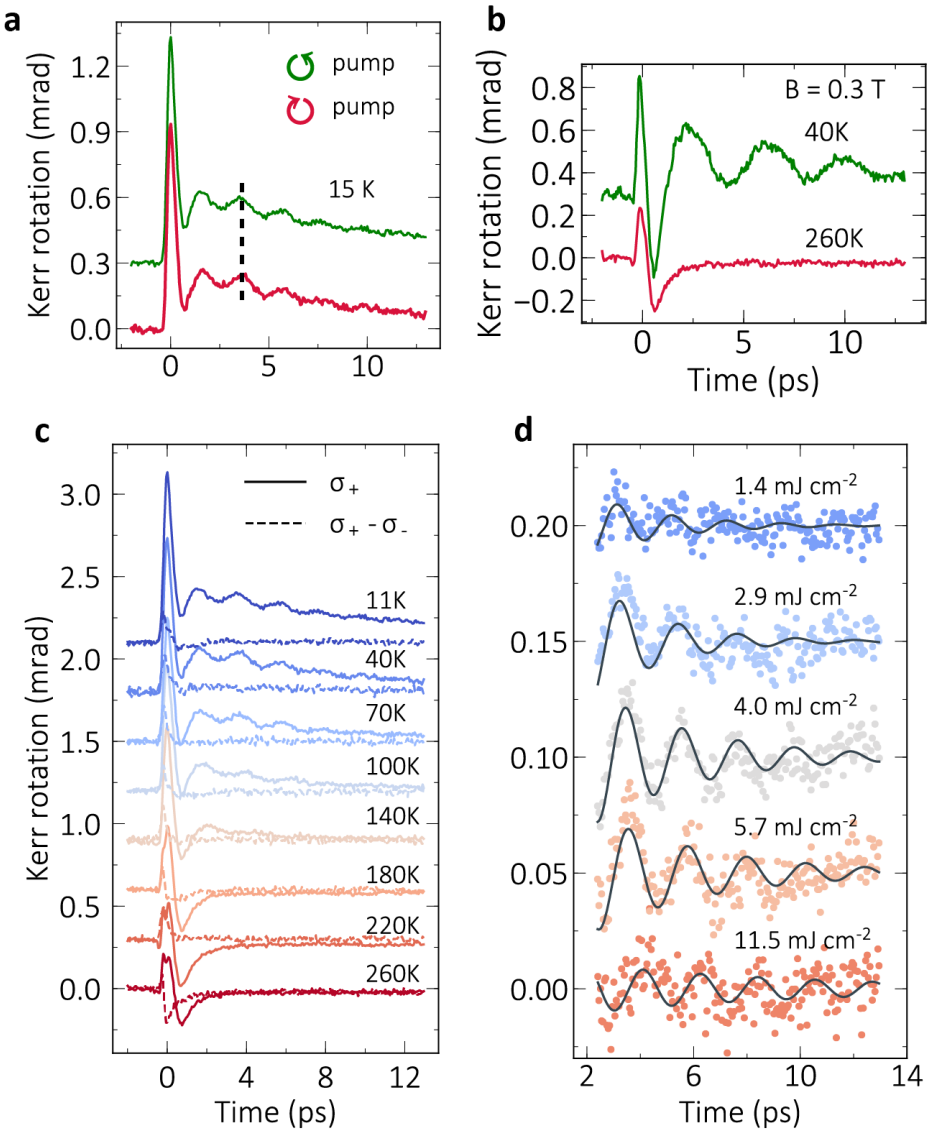

Figure 4.4: The pump fluence is 5.73 mJ cm^{-2} for (a), (b), and (c). (a) Kerr rotation dynamics after the opposite helicities pump (σ_+ and σ_-) at 15 K. Dashed line is the guide to the eye, showing that the phase of the magnon oscillation is in-phase. The baseline of the σ_- pump trace is shifted for clarity. (b) σ_+ pump dynamics at 40 K, 260 K with 0.3 T magnetic field applied along a-axis. (c) Temperature-dependent Kerr rotation dynamics after σ_+ pump (solid lines), and the subtraction of the Kerr rotation dynamics of σ_+ and σ_- pump (σ_+ - σ_-) (dashed lines). (d) Fluence-dependent σ_+ pump magnon dynamics. Solid lines show the result of the fitting of the damped oscillation model.

4.3.1 Magnon dynamics with 1.3 μm pump

We first use circularly polarized 1.3 μm pump pulses, which resonantly excites electrons from the $J_{eff,3/2}$ band to the upper Hubbard band (Fig.(4.2)(b)). The Kerr rotation dynamics at 15 K following pump excitation with left-hand (σ_+) and right-hand (σ_-) circularly polarized pump pulses is shown in Fig.(4.4)(a). We observed a coherent oscillation for both helicities of the pump. The frequency of the oscillation is $\sim$ 0.5 THz, corresponding to a 2 meV B_{2g} single magnon mode reported in Raman measurements [108, 109]. We subtract σ_- from σ_+ to eliminate nonmagnetic contribution in the Kerr rotation signal. We note that the magnon oscillation is in-phase for the σ_+ and σ_- pump, indicated by the vertical dashed line in Fig.(4.4)(a). The temperature-dependent magnon oscillation after the σ_+ pump and the subtraction of σ_+, σ_- pump traces (σ_+ - σ_-) is shown by the solid and dashed lines in Fig.(4.4)(c), respectively. There is no oscillation for the σ_+ - σ_- dynamics for all the temperatures, whereas the coherent magnon oscillation of the σ_+ pump persists up to 180 K. This is consistent with the fact that the B_{2g} single magnon only appears in the AFM phase below the Néel temperature $T_N \sim 230$ K. Fig.(4.4)(d) plots the fluence dependent σ_+ pump dynamics measured at 80 K. The magnon oscillation survives up to 11.45 mJ cm^{-2}, which is high enough to destroy the 3D magnetic order [113], but not the 2D magnetic correlation. This uncovers the in-plane 2D nature of the B_{2g} magnon. We have confirmed that linearly polarized 2 μm pump, which excites electron from the $J_{eff,1/2}$ band to the upper Hubbard band, can also drive the same magnon oscillation. We further applied an in-plane external field of 0.3 T along the a-axis on the sample (Fig.(4.4)(b)), which makes the magnon oscillation slower to $\sim$ 0.26 THz. Since the Sr_2IrO_4 goes through a transition from an AFM phase with staggered pattern (-++-) to a weakly ferromagnetic (++++) phase [115], such FM mode has lower energy than the AFM mode [108].

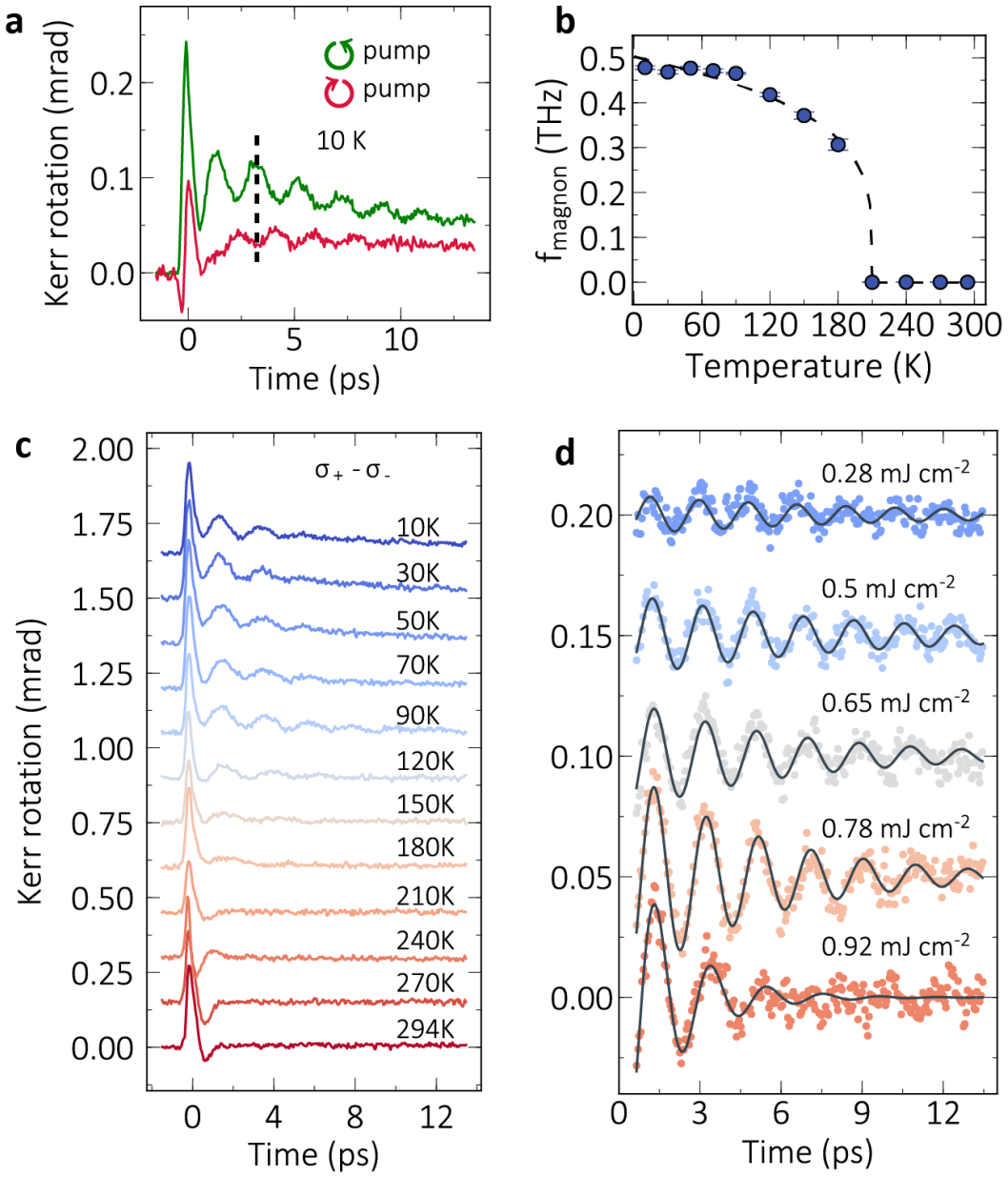

Figure 4.5: Kerr rotation dynamics following 9 μm circularly polarized pump excitation. Pump fluence is 0.92 mJ cm^{-2} for (a) and (b). (a) The Kerr rotation dynamics with the opposite pump helicities (σ_+ and σ_-) at 10K. The vertical dashed line is the guide to the eye, showing that the phase of the magnon oscillation is out-of-phase. (b) Temperature dependence of the magnon oscillation frequency f_{magnon}. The dashed line fits the magnon frequency to the power law scaling $|(1-T/T_N)^{2\beta}|$. (c) The subtraction of Kerr rotation dynamics of σ_+ and σ_- pump (σ_+ - σ_-) at different temperatures. (d) Kerr rotation dynamics after σ_+ - σ_- pump at different fluences. Data are taken at 10K. Solid lines show the result of the fitting of the damped oscillation model.

4.3.2 Magnon dynamics with 9 μm pump

To further investigate the microscopic mechanism of the coherent magnon generation, we use 9 μm (138 meV) circularly polarized pump pulses. Different from 1.3 μm which directly excites charges across the Mott gap, the 9 μm excitation is nonresonant below the Mott gap ($\sim$ 0.5 eV) and above the highest energy of the optical phonons ($\sim$ 82 meV) [91] (Fig.(4.2)(b)). Fig.(4.5)(a) shows the time-dependent Kerr rotation dynamics after 9 μm circularly polarized pump excitation with the opposite helicities (σ_+ and σ_-). The experiment was performed at 10 K with a pump fluence of 0.92 mJ cm^{-2}. The same 0.5 THz B_{2g} single magnon is generated for both helicities as for the 1.3 μm pump, but the phase of the magnon oscillation is the opposite, as shown by the vertical dashed line in Fig.(4.5)(a). We subtract the σ_- pump dynamics from σ_+ to obtain the purely magnetic response. The temperature dependence of the subtracted σ_+ - σ_- dynamics are shown in Fig.(4.5)(c). The coherent magnon oscillation persists up to $\sim$ 210 K. The temperature- dependent magnon frequency is shown in Fig.(4.5)(b), where the order parameter-like power-law scaling behavior of the magnon frequency further demonstrates that the magnon corresponds to AFM magnetic order.

4.4 The origin of the B_{2g} magnon

The dielectric permittivity tensor of a material $\varepsilon_{ij} = \varepsilon_{ij}^{(a)} + \varepsilon_{ij}^{(s)}$ consists of antisymmetric $\varepsilon_{ij}^{(a)}$ and symmetric $\varepsilon_{ij}^{(s)}$ parts, where $\varepsilon_{ij}^{(a)}$ is an odd function of magnetic vectors. Phenomenologically, the magnon oscillation after the 1.3 μm pump is the response of only the symmetric part of the dielectric permittivity tensor $\varepsilon_{ij}^{(s)}$, while the 9 μm pump corresponds to the antisymmetric one $\varepsilon_{ij}^{(a)}$. As a result, even a linearly polarized 1.3 μm pump can drive the same magnon, although it does not carry angular momentum like the circularly polarized one, known as the inverse Cotton-Mouton effect (ICME) [135, 136]. On the other hand, the 9 μm pump dynamics is due to the inverse Faraday effect (IFE): $\vec{M}(0) = \vec{E}(\omega) \times \vec{E}^*(\omega)$ [131]. The circularly polarized pulse

can be treated as an effective out-of-plane magnetic field. The instantaneous spin deflection from the effective magnetic field of σ_+ and σ_- pump pulses will be in the opposite direction, leading to the opposite oscillation phase.

The B_{2g} coherent magnon mode that can be excited by both the 9 μm and 1.3 μm light indicates that there is a small magnon gap. Previous studies of magnetic excitations on Sr_2IrO_4 and its doped compounds ($Sr_{2-x}La_xIrO_4$, $Sr_2Ir_{1-x}Rh_xO_4$) using RIXS, inelastic neutron scattering (INS), and neutron diffraction [1, 102, 103, 104, 105, 116, 141, 142], mainly focused on the higher energy spin-orbit exciton and the magnon dispersion because of limited energy resolution. Such a small spin gap of $\sim$ 2 meV is reported by two Raman experiments [108, 109] (Fig.(3.12)) and recent high-resolution INS and RIXS [95] experiments.

The low-energy in-plane spin gap is from strong pseudospin-lattice coupling (pseudo-Jahn-Taller (JT) effect) [110]. The original form of JT effect arises from the coupling between the orbital degrees of freedom and lattice. Due to the strong spin-orbit coupling in Sr_2IrO_4, its magnetism is described by an effective pseudospin J_{eff} corresponding to the total angular momentum. Thus for JT physics, the pseudospin-lattice coupling has to be considered. The corresponding Hamiltonian is:

$$H_{sp-lat} = \sum_{\langle i,j \rangle} \Gamma (S_i^x S_j^y + S_i^y S_j^x) \tag{4.1}$$

where the interaction strength Γ is estimated to be $\sim$ 3 μeV [95, 110]. From the RIXS measurement [95], this spin gap is located at (π, π) in the two-dimensional Brillouin zone, which is consistent with the 2D nature that we have observed. The details of the spin model of Sr_2IrO_4 are shown in Section 3.8.

4.5 Fitting of the magnon oscillation

The decay dynamics of magnon oscillation for 1.3 μmu and 9 μm excitations consist of a damped oscillator on top of a two-exponential decay. The details of fitting of the two-exponential decay are in Appendix B. The purely magnon oscillation is obtained by subtracting the two-exponential decay fitting from the raw data (Fig.(4.4)(d), (4.5)(d)).

We fit the oscillation part in Fig.(4.4)(d),(4.5)(d) using a damped oscillator function:

$$f = A_{magnon}\, e^{-t/\tau_{magnon}} \sin\left(2\pi f t + \phi\right) \tag{4.2}$$

where A_{magnon} is the magnon amplitude, τ_{magnon} is the time constant, f is the frequency, and ϕ is the oscillation phase. The fitting results are shown as solid curves.

4.6 Microscopic mechanism of magnon excitation

To understand the microscopic mechanism of the magnon generation better, we focus on the fluence-dependence of the coherent magnon dynamics. The fitting results of magnon amplitude A_{magnon} and the damping time constant τ_{magnon} are shown in Fig.(4.6)(a)(b). Remarkably, A_{magnon} and τ_{magnon} of 1.3 μm (red squares) and 9 μm pump (blue circles) scale very differently with fluence. For the 1.3 μm pump, A_{magnon} increases in the low fluence regime then decrease monotonically, while for the 9 μm, it scales quadratically with the pump fluence. The fitted quadratic function is shown as the shaded area in Fig.(4.6)(a). On the other hand, τ_{magnon} decreases (more damped) with higher fluence of 9 μm pump, but it increases with 1.3 μm pump, shown in grey lines as guide to the eye. We suggest that the magnon generation mechanism is totally different between the 1.3 μm and 9 μm pump due to the strikingly opposite fluence-dependent behavior.

For the resonant 1.3 μm pump, since charge excitation is the dominant effect, it is more

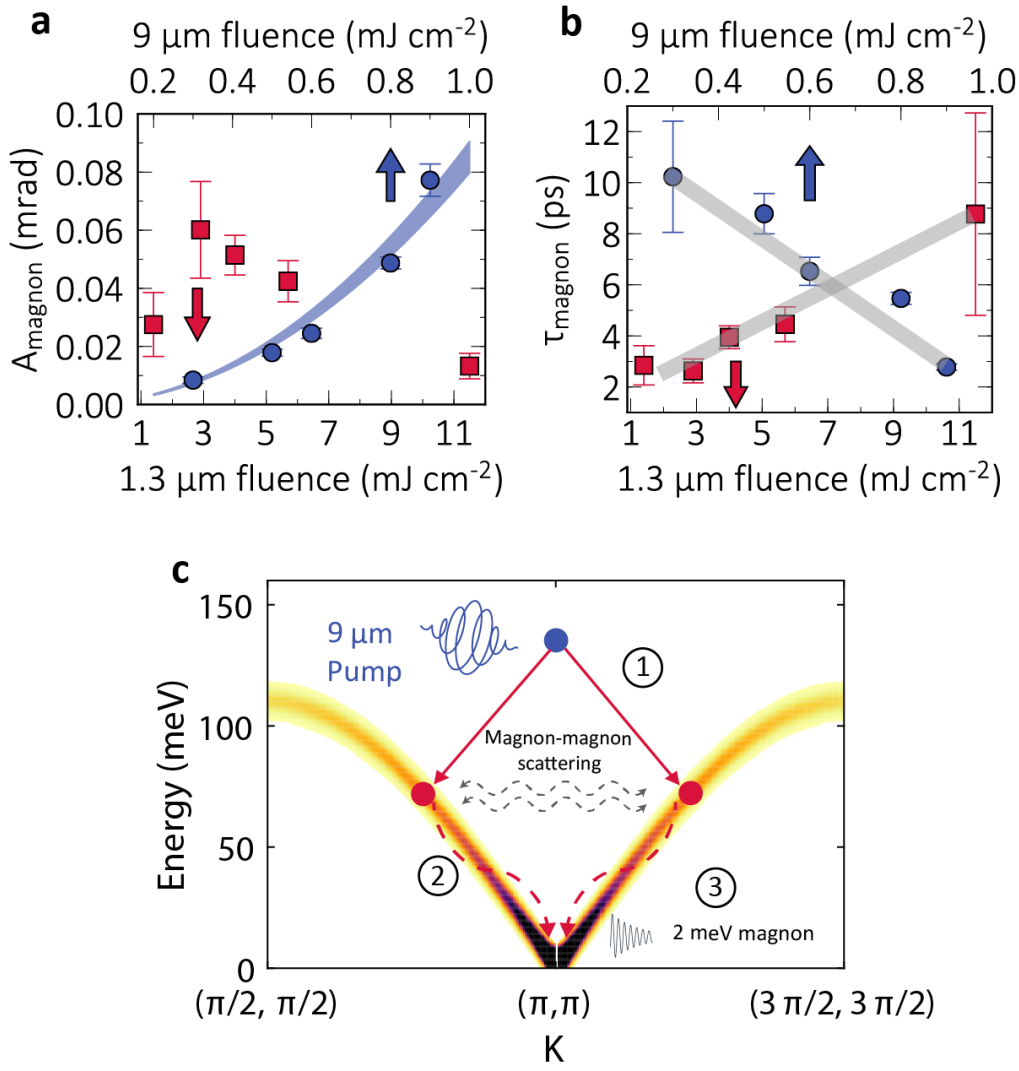

Figure 4.6: Fluence dependent of the magnon amplitude and damping time constant after 1.3 μm and 9 μm pumping and the schematic of the magnon generation mechanism after the 9 μm pump. (a) Magnon oscillation amplitude A_{magnon} shows opposite fluence dependent trend for the 9 μm and 1.3 μm pump. A_{magnon} scales quadratically (fitting result shown in the shaded area) for the 9 μm pump, while it decreases with higher fluence ($>$ 3 mJ cm^{-2}) for the 1.3 μm pump. (b) Magnon oscillation damping time constant τ_{magnon} shows the opposite fluence dependent trend for 9 μm and 1.3 μm pump. It decreases for 9 μm pump while increases for 1.3 μm pump as the fluence increases. Grey lines are guide to the eye. (c) Schematic of the 9 μm magnon generation mechanism. The 9 μm (138 meV) photon couples to two 69 meV magnons of the opposite momentum and then decays to the low-energy 2 meV magnon via magnon-magnon scattering.

challenging to extract the pure spin contribution that for the 9 μm pump. The charge recovery time is typically $\sim$ 2 ps for photodoping the Sr_2IrO_4 [113, 143, 144], similar to 2D magnetic recovery time scale according to the time-resolved RIXS experiment, while the 3D magnetic recovery time is on the order of hundreds of picoseconds. It is also observed that the spectral intensity of low-energy magnon at (π,π) increases after the 2 μm excitation [113]. It is attributed to the fact that the relaxation of high energy magnons via the emission of lower energy magnons as is not to occur as an important relaxation channel following excitation across a correlation gap. The low-energy magnon oscillation after the 1.3 μm pump in our experiment is a very similar story. Since both charge and spin channels are involved in the process, the analysis of the magnon generation mechanism after the 1.3 μm excitation is beyond the scope of current work. We will mainly focus on the 9 μm pump in the following.

Since the energy of the 9 μm (138 meV) pump is non-resonant below the band gap, we consider it to be purely magnon excitation. The quadratic scaling of the fluence dependence of the magnon amplitude indicates that the electric field of the pump couples to bilinear spin operator [145]. Fig.(4.6)(c) shows one of the possibilities of the magnon generation process (known as two-magnon generation): (1) the pump photon excites magnon pairs of opposite momenta from (π,π) at half the photon energy (69 meV); (2) These magnon pairs then decay to the lowest energy B_{2g} in-plane magnon mode via magnon-magnon scattering on a short timescale; (3) The B_{2g} magnon starts to oscillate and is detected by time-domain Kerr rotation signal as described above. With more magnon modes generated by higher pump fluence, the initial density of the B_{2g} magnon is larger, thus leading to stronger damping of the oscillation (Fig.(4.6)(b). The fully microscopic theoretical treatment of the optical excitation of magnons in Sr_2IrO_4 has detailed analysis of all the possibilities of the magnon generation including virtual process of interaction between electric field and magnons [145]. Such a pure magnon generation mechanism by the 9 μm pump leads to a markedly high generation efficiency: 0.24 mrad mJ^{-1} cm^2, almost ten times more efficient than that for the 1.3 μm pump (0.029 mrad mJ^{-1} cm^2). The generation

efficiency is determined by the two-magnon density of states. The effective field induced by the light is predicted to peak at twice the bandwidth energy due to the nesting of the maxima of the dispersion at Brillion zone boundary.

4.7 Outlook

Our findings propose and demonstrate a novel mechanism to control and generate magnons in a spin-orbit coupled Mott insulator Sr_2IrO_4 using ultrafast pulse. The direct excitation of the spin degree of freedom with light leads to highly efficient magnon generation. It sheds light on understanding the magnetic dynamics for the 2D AFM order in Sr_2IrO_4, and paves ways of ultrafast magnetic control and spintronics by efficient magnon generation.

There remains a great deal to explore about this novel magnon excitation mechanism in Sr_2IrO_4. For future direction, one can tune the pump wavelength to the two-magnon peak to maximize the magnon generation efficiency [145, 146]. Further theoretical model is needed to better understand the fluence-dependent magnon decay time for 9 μm pump (Fig.(4.6)(b)).

To generalize this idea, other material platforms may host similar magnon generation mechanism. For example, antiferromagnets with strong spin-orbit coupling and magnetic anisotropies like NiO and $DyFeO_3$, other iridates ($Sr_3Ir_2O_7$), and cuprates. Another interesting direction is to use light to excite magnons that are topologically nontrivial [147, 148], which can lead to topologically protected edge states.

Chapter 4 is about a paper in preparation, discussing about ultrafast magnetic control in Sr_2IrO_4. Authors include Gufeng Zhang, Xiang Chen, Urban F.P. Seifert, Jingdi Zhang, Kevin Cremin, Leon Balents, Stephen D. Wilson and Richard D. Averitt. The thesis author is the primary author of this chapter.

Appendix A

THz-TDS on V_2O_3 thin film

Elaborate upon the data analysis process of THz-TDS experiments, I take the V_2O_3 thin film data as an example. V_2O_3 is a Mott-Hubbard insulator, with high-temperature paramagnetic metal (PM) phase and low-temperature antiferromagnetic insulating (AI) phase (< 150 K). It is an ideal platform to study metal-insulator transition, and its phase diagram, electronic properties, optical properties and dynamics are studied comprehensively [149, 150, 151, 152].

In our experiment, a 75 nm V_2O_3 thin film is grown on sapphire substrate, and we use a bare sapphire substrate as reference. Using THz-TDS we can extract the temperature-dependent THz conducitivity. Fig.A.1, A.2 show (a) the THz-TDS temporal scan, (b) the Fourier transform spectrum and (c) the complex transmission coefficient $T(\omega) = E_{sig}(\omega)/E_{ref}(\omega)$ at 80 K and 293 K. At 80 K, V_2O_3 is in antiferromagnetic insulating phase, and THz transmitted through the sample and reference are almost identical, so the transmission coefficient is almost 1, yielding zero conductivity. At higher temperature 293 K, the THz signal transmitted through the sample is much smaller than the substrate. The corresponding transmission coefficient is calculated by dividing the signal spectrum by the reference spectrum. As shown in Fig. A.2 (c), the transmission $T(\omega)$ is 0.34, and is pretty flat in the THz detection range, corresponding to a Drude response with a short scattering time. We choose the transmission at 1 THz to calculate the conductivity.

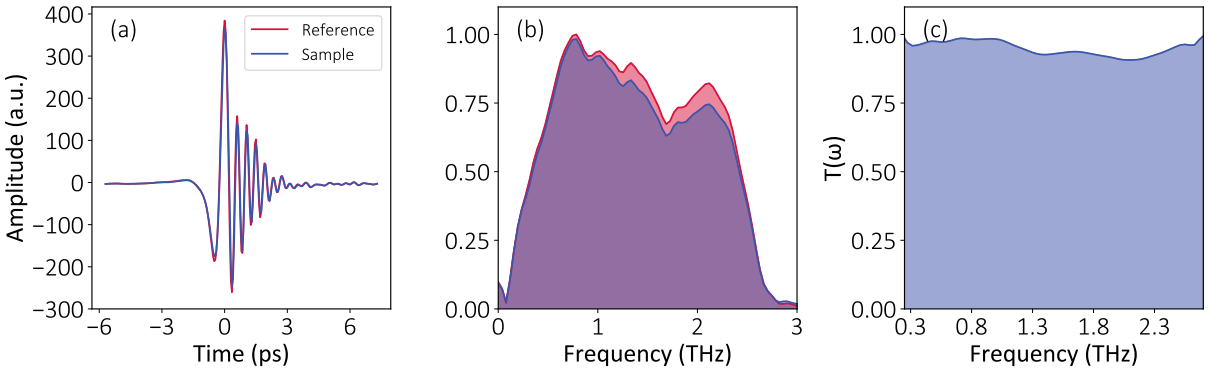

Figure A.1: (a) 80 K THz-TDS temporal profile of sample (V_2O_3 thin film on sapphire substrate), reference (bare sapphire substrate) and (b) their corresponding spectrum, (c) Transmission coefficient.

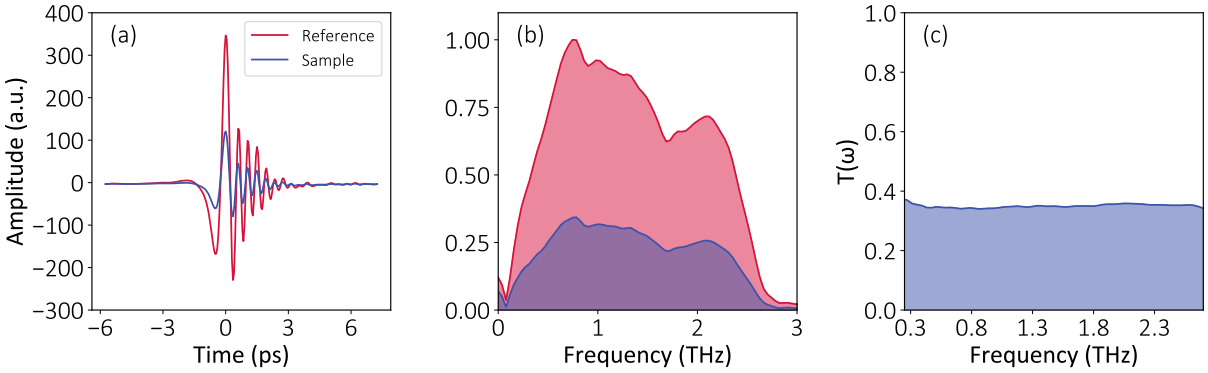

Figure A.2: (a) 293 K THz-TDS temporal profile of sample (V_2O_3 thin film on sapphire substrate), reference (bare sapphire substrate) and (b) their corresponding spectrum, (c) Transmission coefficient.

With the help of Eq.2.13 we can extract the conductivity at different temperatures while warming and cooling the sample. The result is shown in Fig.A.3. The sample is an insulator below 140 K, and starts to be more metallic for higher temperatures, reaching the maximum conductivity of $\sim 2800\ \Omega^{-1}cm^{-1}$ at 180 K. The narrow hysteresis is due to the first order nature of the transition [153]. The fact that the conductivity extracted from the THz-TDS measurement is consistent with conventional conductivity measurement proves that this is a very useful method.

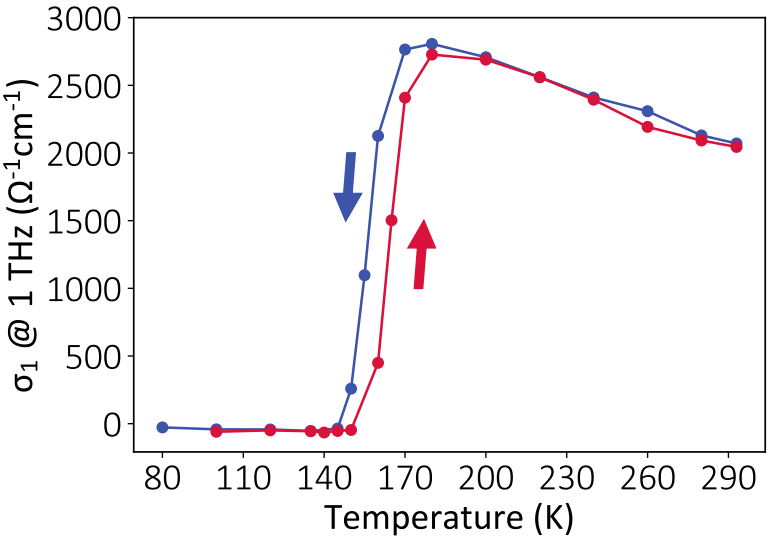

Figure A.3: Temperature dependent V_2O_3 thin film conductivity at 1 THz extracted from THz-TDS experiment. Measurement taken while cooling down (blue) and warming up (red) the sample.

Appendix B

Fitting of the Kerr rotation dynamics of Sr_2IrO_4

We use an error function convoluted with a two-exponential decay function to fit the non-oscillatory part of the Kerr rotation dynamics:

$$f_{non-osc} = a\,[erf(bt)+1](e^{-t/t_s} + c\,e^{-t/t_f}) \tag{B.1}$$

where the error function

$$erf(x) = \frac{2}{\sqrt{\pi}} \int_0^x e^{-t^2} dt \tag{B.2}$$

describes the rising dynamics from the convolution of the pump and probe pulses. Fitting parameters include t_s, slow decay dynamics; t_f, fast decay dynamics; a, amplitude; b, corresponds to the rising time scale; c, relative amplitude of fast dynamics compared with slow dynamics.

B.1 The fitting of fluence-dependent 9 μm pump Kerr rotation probe

The fitting of fluence-dependent of 9 μm pump Kerr rotation probe is shown in Fig.B.1. Blue points are experimental data and red lines are the fitting curves (Eq.B.1). The fitting curves follow the non-oscillatory part very well. The results of the fitting parameters a, t_s and t_f are shown in Fig. B.2.

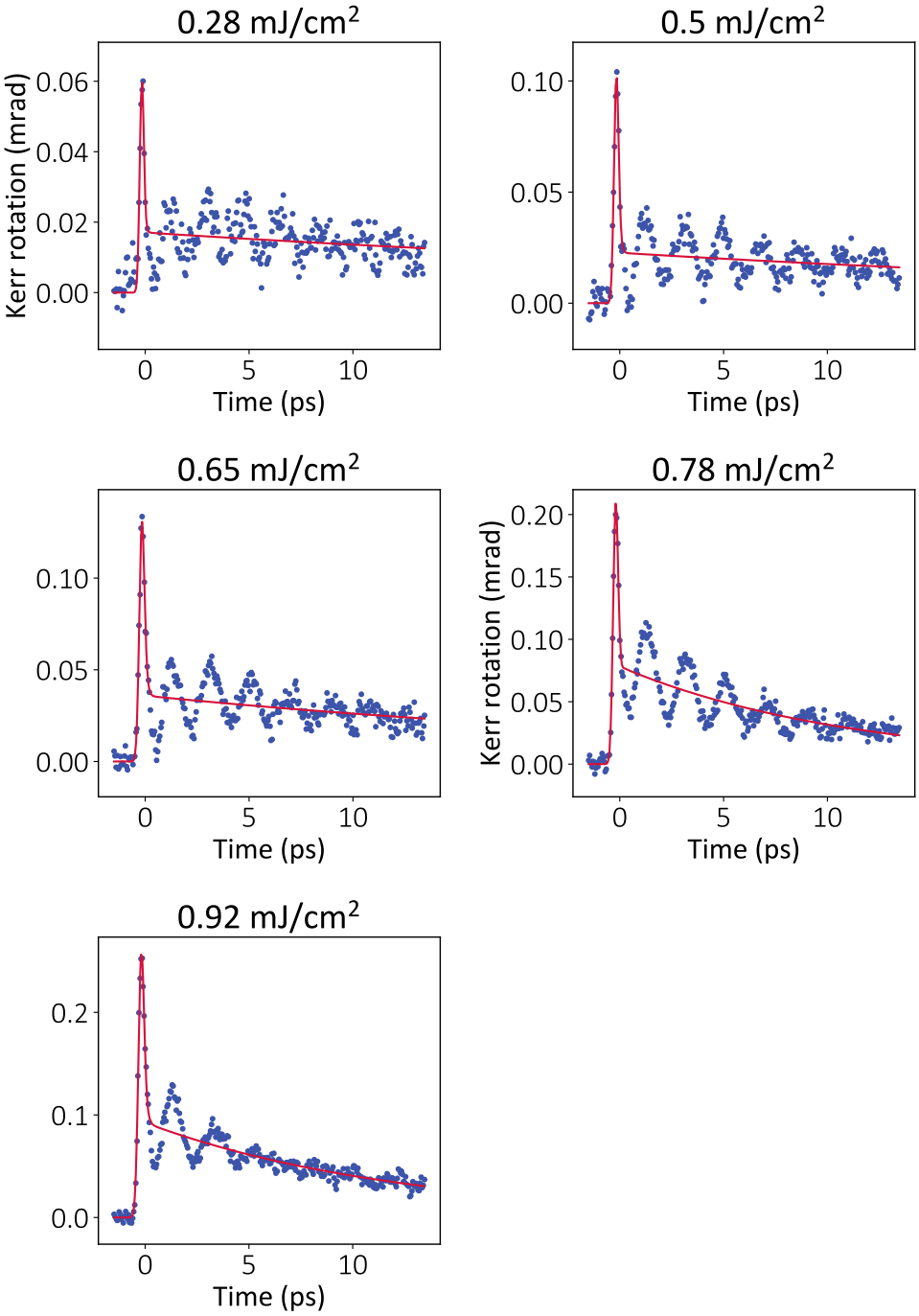

Figure B.1: The fitting of the non-oscillatory part of the fluence-dependent of 9 μm pump Kerr rotation probe dynamics. Blue points are the experiment data points, red lines are the fits.

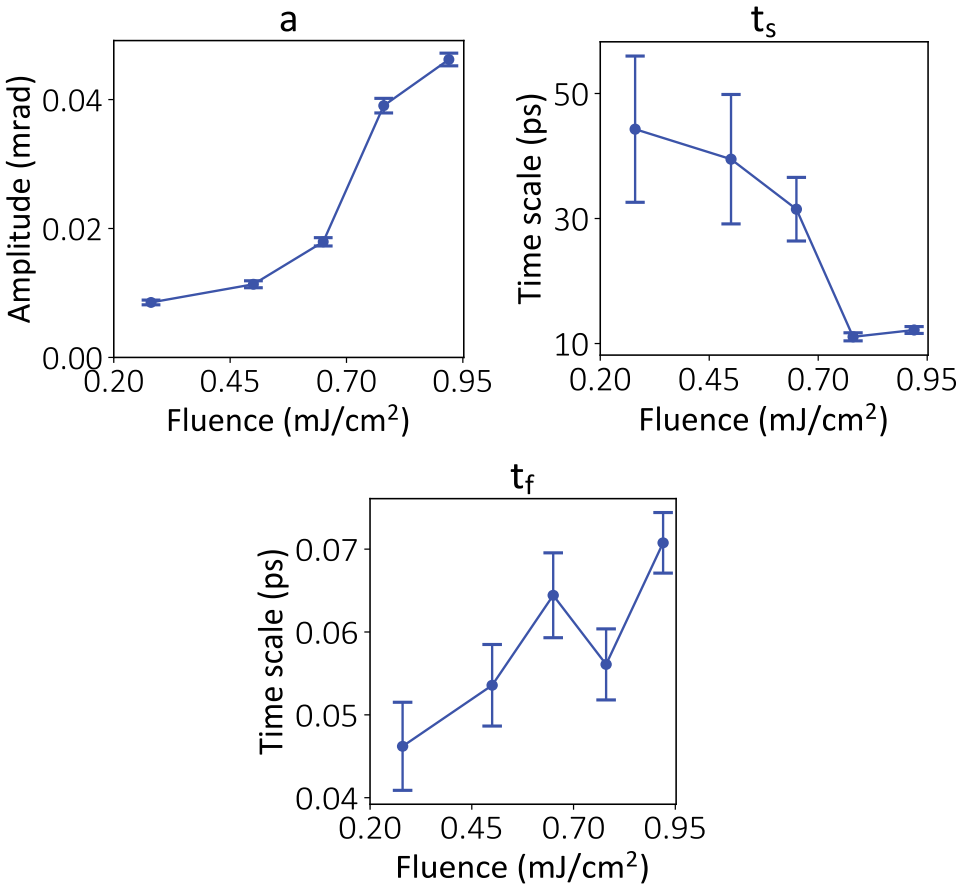

Figure B.2: The fluence-dependent fitting parameters for 9 μm pump: amplitude a, slow decay t_s, fast decay t_f.

B.2 The fitting of temperature dependent 9 μm pump Kerr rotation probe

The fitting of temperature-dependent of 9 μm pump Kerr rotation probe is shown in Fig.B.1. Blue points are experiment data and red lines are the fitting curves (Eq.B.1). The fitting curves follow the non-oscillatory part very well. The results of the fitting parameters a, t_s and t_f are shown in Fig. B.3.

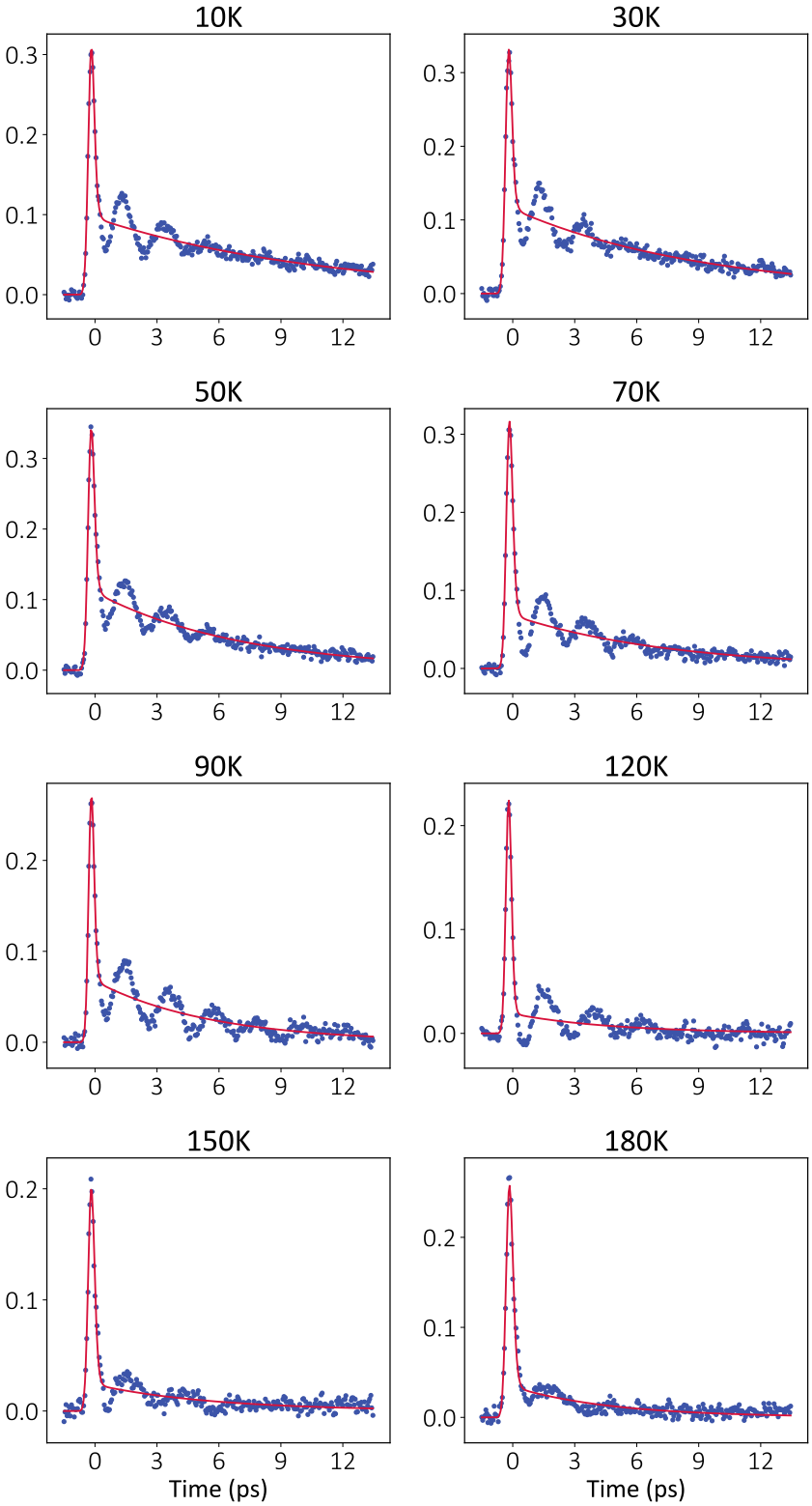

Figure B.3: The fitting of the non-oscillatory part of the temperature-dependent of 9 μm pump Kerr rotation probe dynamics. Blue points are the experiment data points, red lines are the fits.

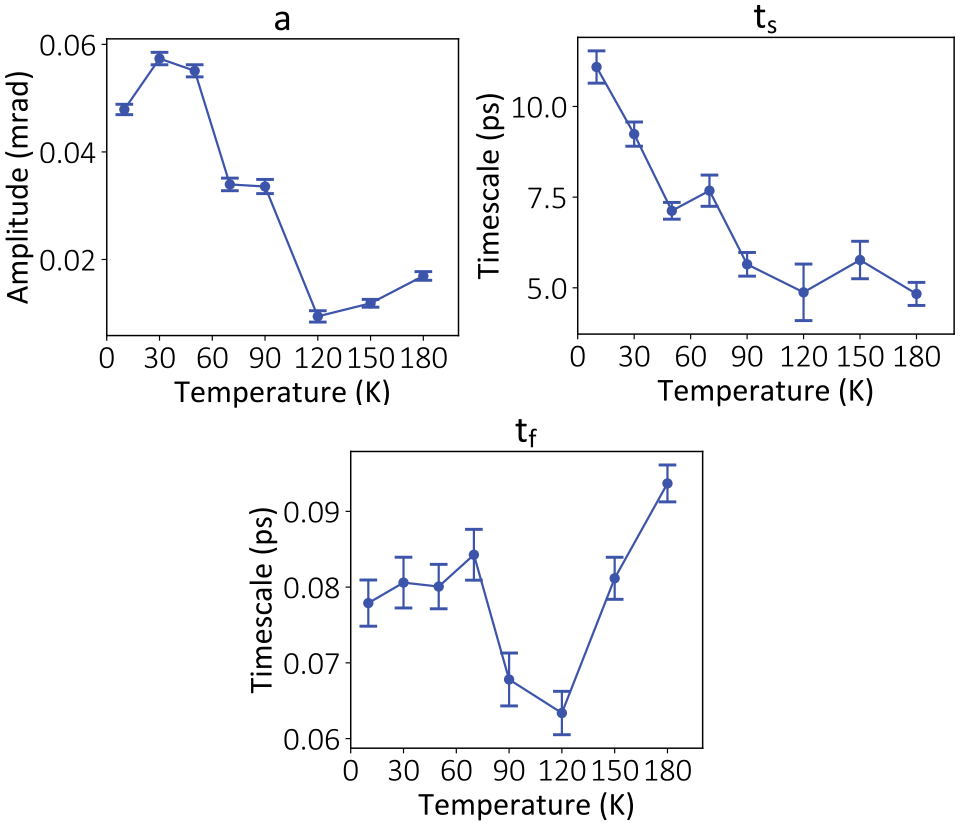

Figure B.4: The temperature dependent fitting parameters: amplitude a, slow decay t_s, fast decay t_f.

B.3 The fitting of fluence dependent 1.3 μm pump Kerr rotation probe

The fitting of the non-oscillatory part of the fluence-dependent of 1.3 μm pump Kerr rotation probe dynamics is shown in Fig. B.5, where blue points are experimental data and the red curves are fits. Different from the one for 9 μm pump (Fig. B.1), there is a second rise dynamics around 1 ps, which is hard to fit using eq. B.1. So we only fit the decay dynamics after 1 ps.

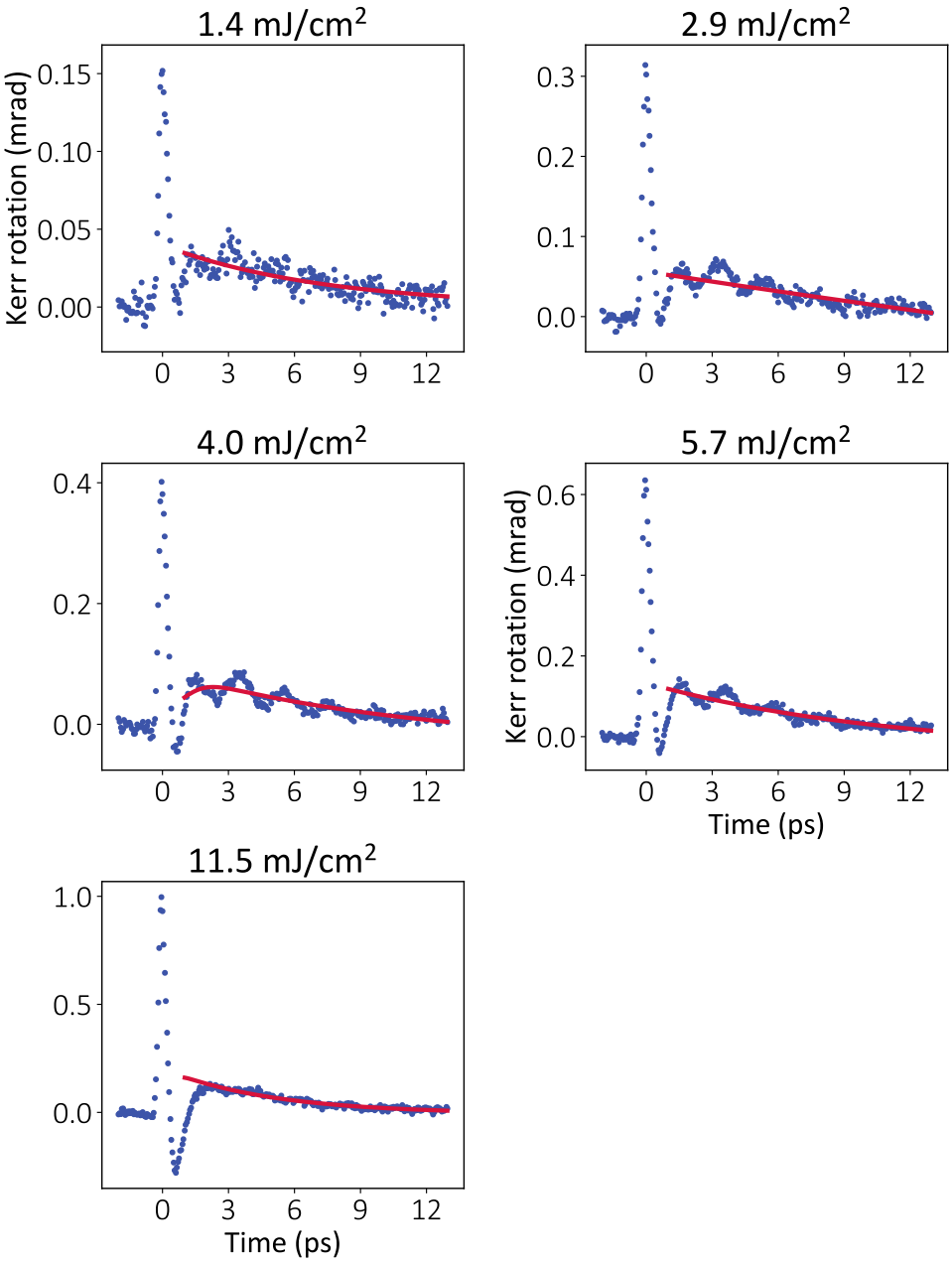

Figure B.5: The fitting of the non-oscillatory part of the fluence-dependent of 1.3 μm pump Kerr rotation probe dynamics. Blue points are the experiment data points, red lines are the fits.

Bibliography

[1] J. Kim, D. Casa, M. H. Upton, T. Gog, Y.-J. Kim, J. F. Mitchell, M. van Veenendaal, M. Daghofer, J. van den Brink, G. Khaliullin, and B. J. Kim, "Magnetic Excitation Spectra of Sr_2IrO_4 Probed by Resonant Inelastic X-Ray Scattering: Establishing Links to Cuprate Superconductors," *Physical Review Letters*, vol. 108, p. 177003, apr 2012.

[2] N. S. Headings, S. M. Hayden, R. Coldea, and T. G. Perring, "Anomalous High-Energy Spin Excitations in the High-T_c Superconductor-Parent Antiferromagnet La_2CuO_4," *Physical Review Letters*, vol. 105, p. 247001, dec 2010.

[3] D. N. Basov, R. Averitt, D. van der Marel, M. Dressel, and K. Haule, "Electrodynamics of correlated electron materials," *Reviews of Modern Physics*, vol. 83, pp. 471–542, jun 2011.

[4] D. N. Basov, R. D. Averitt, and D. Hsieh, "Towards properties on demand in quantum materials," *Nature Materials*, vol. 16, no. 11, pp. 1077–1088, 2017.

[5] L. Stojchevska, I. Vaskivskyi, T. Mertelj, P. Kusar, D. Svetin, S. Brazovskii, and D. Mihailovic, "Ultrafast Switching to a Stable Hidden Quantum State in an Electronic Crystal," *Science*, vol. 344, pp. 177–180, apr 2014.

[6] J. Zhang, X. Tan, M. Liu, S. W. Teitelbaum, K. W. Post, F. Jin, K. A. Nelson, D. N. Basov, W. Wu, and R. D. Averitt, "Cooperative photoinduced metastable phase control in strained manganite films," *Nature Materials*, vol. 15, pp. 956–960, sep 2016.

[7] R. W. Boyd, *Nonlinear optics*. Academic press, 2019.

[8] P. A. Franken, A. E. Hill, C. W. Peters, and G. Weinreich, "Generation of Optical Harmonics," *Physical Review Letters*, vol. 7, pp. 118–119, aug 1961.

[9] A. J. Prasankumar, Rohit P and Taylor, *Optical techniques for solid-state materials characterization*. CRC Press, 2016.

[10] A. Kotov, V.A, and Zvezdin, *Modern Magnetooptics and Magnetooptical Materials*. CRC Press, 1997.

[11] B. Koopmans, M. van Kampen, J. T. Kohlhepp, and W. J. M. de Jonge, "Ultrafast Magneto-Optics in Nickel: Magnetism or Optics?," *Physical Review Letters*, vol. 85, pp. 844–847, jul 2000.

[12] P. W. Anderson, "More Is Different," *Science*, vol. 177, pp. 393–396, aug 1972.

[13] M. Mitrano, A. Cantaluppi, D. Nicoletti, S. Kaiser, A. Perucchi, S. Lupi, P. Di Pietro, D. Pontiroli, M. Riccò, S. R. Clark, D. Jaksch, and A. Cavalleri, "Possible light-induced superconductivity in K_3C_{60} at high temperature," *Nature*, vol. 530, pp. 461–464, feb 2016.

[14] O. Schubert, M. Hohenleutner, F. Langer, B. Urbanek, C. Lange, U. Huttner, D. Golde, T. Meier, M. Kira, S. W. Koch, and R. Huber, "Sub-cycle control of terahertz high-harmonic generation by dynamical Bloch oscillations," *Nature Photonics*, vol. 8, pp. 119–123, feb 2014.

[15] J. Zhang and R. Averitt, "Dynamics and Control in Complex Transition Metal Oxides," *Annual Review of Materials Research*, vol. 44, pp. 19–43, jul 2014.

[16] D. B. Tanner, *Optical Effects in Solids*. Cambridge University Press, may 2019.

[17] A. H. Zewail, "Laser Femtochemistry," *Science*, vol. 242, pp. 1645–1653, dec 1988.

[18] T. Kampfrath, A. Sell, G. Klatt, A. Pashkin, S. Mährlein, T. Dekorsy, M. Wolf, M. Fiebig, A. Leitenstorfer, and R. Huber, "Coherent terahertz control of antiferromagnetic spin waves," *Nature Photonics*, vol. 5, pp. 31–34, jan 2011.

[19] R. Huber, A. Brodschelm, F. Tauser, and A. Leitenstorfer, "Generation and field-resolved detection of femtosecond electromagnetic pulses tunable up to 41 THz," *Applied Physics Letters*, vol. 76, pp. 3191–3193, may 2000.

[20] D. J. Cook and R. M. Hochstrasser, "Intense terahertz pulses by four-wave rectification in air," *Optics Letters*, vol. 25, p. 1210, aug 2000.

[21] M. Hangyo, M. Tani, and T. Nagashima, "Terahertz Time-Domain Spectroscopy of Solids: A Review," *International Journal of Infrared and Millimeter Waves*, vol. 26, pp. 1661–1690, dec 2005.

[22] D. H. Auston, K. P. Cheung, and P. R. Smith, "Picosecond photoconducting Hertzian dipoles," *Applied Physics Letters*, vol. 45, pp. 284–286, aug 1984.

[23] P. Smith, D. Auston, and M. Nuss, "Subpicosecond photoconducting dipole antennas," *IEEE Journal of Quantum Electronics*, vol. 24, pp. 255–260, feb 1988.

[24] Q. Wu and X. Zhang, "Free-space electro-optic sampling of terahertz beams," *Applied Physics Letters*, vol. 67, pp. 3523–3525, dec 1995.

[25] Q. Wu and X. Zhang, "Ultrafast electro-optic field sensors," *Applied Physics Letters*, vol. 68, pp. 1604–1606, mar 1996.

[26] Q. Wu and X.-C. Zhang, "7 terahertz broadband GaP electro-optic sensor," *Applied Physics Letters*, vol. 70, pp. 1784–1786, apr 1997.

[27] M. Kress, T. Löffler, S. Eden, M. Thomson, and H. G. Roskos, "Terahertz-pulse generation by photoionization of air with laser pulses composed of both fundamental and second-harmonic waves," *Optics Letters*, vol. 29, no. 10, p. 1120, 2004.

[28] Y.-S. Lee, *Principles of terahertz science and technology*. Springer Science & Business Media, 2009.

[29] V. K. Thorsmølle, *Terahertz Time-Domain Spectroscopy of High-T_c Superconductors*. PhD thesis, 2001.

[30] H. Hirori, A. Doi, F. Blanchard, and K. Tanaka, "Single-cycle terahertz pulses with amplitudes exceeding 1 MV/cm generated by optical rectification in $LiNbO_3$," *Applied Physics Letters*, vol. 98, no. 9, 2011.

[31] J. Hebling, K.-L. Yeh, M. C. Hoffmann, B. Bartal, and K. A. Nelson, "Generation of high-power terahertz pulses by tilted-pulse-front excitation and their application possibilities," *Journal of the Optical Society of America B*, vol. 25, no. 7, p. B6, 2008.

[32] J. A. Fülöp, L. Pálfalvi, S. Klingebiel, G. Almási, F. Krausz, S. Karsch, and J. Hebling, "Generation of sub-mJ terahertz pulses by optical rectification," *Optics Letters*, vol. 37, no. 4, p. 557, 2012.

[33] F. D. J. Brunner, O.-P. Kwon, S.-J. Kwon, M. Jazbinšek, A. Schneider, and P. Günter, "A hydrogen-bonded organic nonlinear optical crystal for high-efficiency terahertz generation and detection," *Optics Express*, vol. 16, no. 21, p. 16496, 2008.

[34] C. Ruchert, C. Vicario, and C. P. Hauri, "Scaling submillimeter single-cycle transients toward megavolts per centimeter field strength via optical rectification in the organic crystal OH1," *Optics Letters*, vol. 37, no. 5, p. 899, 2012.

[35] L. Mutter, F. D. Brunner, Z. Yang, M. Jazbinšek, and P. Günter, "Linear and nonlinear optical properties of the organic crystal DSTMS," *Journal of the Optical Society of America B*, vol. 24, no. 9, p. 2556, 2007.

[36] Z. Yang, L. Mutter, M. Stillhart, B. Ruiz, S. Aravazhi, M. Jazbinsek, A. Schneider, V. Gramlich, and P. Günter, "Large-size bulk and thin-film stilbazolium-salt single crystals for nonlinear optics and THz generation," *Advanced Functional Materials*, vol. 17, no. 13, pp. 2018–2023, 2007.

[37] M. Stillhart, A. Schneider, and P. Günter, "Optical properties of 4-N,N-dimethylamino-4′-N′-methyl-stilbazolium 2,4,6-trimethylbenzenesulfonate crystals at terahertz frequencies," *Journal of the Optical Society of America B*, vol. 25, p. 1914, nov 2008.

[38] A. Schneider, I. Biaggio, and P. Günter, "Optimized generation of THz pulses via optical rectification in the organic salt DAST," *Optics Communications*, vol. 224, no. 4-6, pp. 337–341, 2003.

[39] T. Kampfrath, K. Tanaka, and K. A. Nelson, "Resonant and nonresonant control over matter and light by intense terahertz transients," *Nature Photonics*, vol. 7, pp. 680–690, sep 2013.

[40] T. Bartel, P. Gaal, K. Reimann, M. Woerner, and T. Elsaesser, "Generation of single-cycle THz transients with high electric-field amplitudes," *Optics Letters*, vol. 30, no. 20, p. 2805, 2005.

[41] J. Liu and X. C. Zhang, "Terahertz-radiation-enhanced emission of fluorescence from gas plasma," *Physical Review Letters*, vol. 103, no. 23, pp. 1–4, 2009.

[42] J. Liu, J. Dai, S. L. Chin, and X. C. Zhang, "Broadband terahertz wave remote sensing using coherent manipulation of fluorescence from asymmetrically ionized gases," *Nature Photonics*, vol. 4, no. 9, pp. 627–631, 2010.

[43] H. Wen and A. M. Lindenberg, "Coherent Terahertz Polarization Control through Manipulation of Electron Trajectories," *Physical Review Letters*, vol. 103, no. 2, pp. 2–5, 2009.

[44] Z. Z. Zhang, Y. Chen, S. Cui, F. He, M. Chen, Z. Z. Zhang, J. Yu, L. Chen, Z. Sheng, and J. Zhang, "Manipulation of polarizations for broadband terahertz waves emitted from laser plasma filaments," *Nature Photonics*, vol. 12, no. 9, pp. 554–559, 2018.

[45] J. Dai, N. Karpowicz, and X. C. Zhang, "Coherent polarization control of terahertz waves generated from two-color laser-induced gas plasma," *Physical Review Letters*, vol. 103, no. 2, pp. 1–4, 2009.

[46] J. Dai and X. C. Zhang, "Terahertz wave generation from gas plasma using a phase compensator with attosecond phase-control accuracy," *Applied Physics Letters*, vol. 94, no. 2, pp. 92–95, 2009.

[47] J. Dai, X. Xie, and X.-C. Zhang, "Detection of Broadband Terahertz Waves with a Laser-Induced Plasma in Gases," *Physical Review Letters*, vol. 97, p. 103903, sep 2006.

[48] N. Karpowicz, J. Dai, X. Lu, Y. Chen, M. Yamaguchi, H. Zhao, X. C. Zhang, L. Zhang, C. Zhang, M. Price-Gallagher, C. Fletcher, O. Mamer, A. Lesimple, and K. Johnson, "Coherent heterodyne time-domain spectrometry covering the entire "terahertz gap"," *Applied Physics Letters*, vol. 92, no. 1, pp. 1–4, 2008.

[49] X. Xie, J. Dai, and X. C. Zhang, "Coherent control of THz wave generation in ambient air," *Physical Review Letters*, vol. 96, no. 7, pp. 1–4, 2006.

[50] K.-Y. Kim, J. H. Glownia, A. J. Taylor, and G. Rodriguez, "Terahertz emission from ultrafast ionizing air in symmetry-broken laser fields," *Optics Express*, vol. 15, no. 8, p. 4577, 2007.

[51] V. A. Kostin, I. D. Laryushin, A. A. Silaev, and N. V. Vvedenskii, "Ionization-Induced Multiwave Mixing: Terahertz Generation with Two-Color Laser Pulses of Various Frequency Ratios," *Physical Review Letters*, vol. 117, no. 3, pp. 19–21, 2016.

[52] L. L. Zhang, W. M. Wang, T. Wu, R. Zhang, S. J. Zhang, C. L. Zhang, Y. Zhang, Z. M. Sheng, and X. C. Zhang, "Observation of Terahertz Radiation via the Two-Color Laser Scheme with Uncommon Frequency Ratios," *Physical Review Letters*, vol. 119, no. 23, pp. 1–6, 2017.

[53] Y. S. You, T. I. Oh, and K. Y. Kim, "Off-axis phase-matched terahertz emission from two-color laser-induced plasma filaments," *Physical Review Letters*, vol. 109, no. 18, pp. 1–5, 2012.

[54] W. M. Wang, Z. M. Sheng, Y. T. Li, Y. Zhang, and J. Zhang, "Terahertz emission driven by two-color laser pulses at various frequency ratios," *Physical Review A*, vol. 96, no. 2, pp. 1–8, 2017.

[55] M. Clerici, M. Peccianti, B. E. Schmidt, L. Caspani, M. Shalaby, M. Giguère, A. Lotti, A. Couairon, F. Légaré, T. Ozaki, D. Faccio, and R. Morandotti, "Wavelength scaling of terahertz generation by gas ionization," *Physical Review Letters*, vol. 110, no. 25, pp. 1–5, 2013.

[56] K. Y. Kim, A. J. Taylor, J. H. Glownia, and G. Rodriguez, "Coherent control of terahertz supercontinuum generation in ultrafast laser-gas interactions," *Nature Photonics*, vol. 2, no. 10, pp. 605–609, 2008.

[57] H. Wen, M. Wiczer, and A. M. Lindenberg, "Ultrafast electron cascades in semiconductors driven by intense femtosecond terahertz pulses," *Physical Review B*, vol. 78, p. 125203, sep 2008.

[58] I.-C. Ho, X. Guo, and X.-C. Zhang, "Design and performance of reflective terahertz air-biased-coherent-detection for time-domain spectroscopy," *Optics Express*, vol. 18, p. 2872, feb 2010.

[59] W. Hu, S. Catalano, M. Gibert, J. M. Triscone, and A. Cavalleri, "Broadband terahertz spectroscopy of the insulator-metal transition driven by coherent lattice deformation at the $SmNiO_3/LaAlO_3$ interface," *Physical Review B*, vol. 93, no. 16, pp. 1–4, 2016.

[60] A. Sell, A. Leitenstorfer, and R. Huber, "Phase-locked generation and field-resolved detection of widely tunable terahertz pulses with amplitudes exceeding 100 MV/cm," *Optics Letters*, vol. 33, p. 2767, dec 2008.

[61] M. Hohenleutner, F. Langer, O. Schubert, M. Knorr, U. Huttner, S. W. Koch, M. Kira, and R. Huber, "Real-time observation of interfering crystal electrons in high-harmonic generation," *Nature*, vol. 523, pp. 572–575, jul 2015.

[62] F. Langer, M. Hohenleutner, C. P. Schmid, C. Poellmann, P. Nagler, T. Korn, C. Schüller, M. S. Sherwin, U. Huttner, J. T. Steiner, S. W. Koch, M. Kira, and R. Huber, "Lightwave-driven quasiparticle collisions on a subcycle timescale," *Nature*, vol. 533, pp. 225–229, may 2016.

[63] H. Liu, Y. Li, Y. S. You, S. Ghimire, T. F. Heinz, and D. A. Reis, "High-harmonic generation from an atomically thin semiconductor," *Nature Physics*, vol. 13, pp. 262–265, mar 2017.

[64] F. Langer, M. Hohenleutner, U. Huttner, S. W. Koch, M. Kira, and R. Huber, "Symmetry-controlled temporal structure of high-harmonic carrier fields from a bulk crystal," *Nature Photonics*, vol. 11, pp. 227–231, apr 2017.

[65] N. Yoshikawa, T. Tamaya, and K. Tanaka, "High-harmonic generation in graphene enhanced by elliptically polarized light excitation," *Science*, vol. 356, pp. 736–738, may 2017.

[66] M. Rini, R. Tobey, N. Dean, J. Itatani, Y. Tomioka, Y. Tokura, R. W. Schoenlein, and A. Cavalleri, "Control of the electronic phase of a manganite by mode-selective vibrational excitation," *Nature*, vol. 449, pp. 72–74, sep 2007.

[67] R. Mankowsky, A. Subedi, M. Först, S. O. Mariager, M. Chollet, H. T. Lemke, J. S. Robinson, J. M. Glownia, M. P. Minitti, A. Frano, M. Fechner, N. A. Spaldin, T. Loew, B. Keimer, A. Georges, and A. Cavalleri, "Nonlinear lattice dynamics as a basis for enhanced superconductivity in $YBa_2Cu_3O_{6.5}$," *Nature*, vol. 516, pp. 71–73, dec 2014.

[68] C. A. Werley, S. M. Teo, and K. A. Nelson, "Pulsed laser noise analysis and pump-probe signal detection with a data acquisition card," *Review of Scientific Instruments*, vol. 82, p. 123108, dec 2011.

[69] N. F. Mott and R. Peierls, "Discussion of the paper by de Boer and Verwey," *Proceedings of the Physical Society*, vol. 49, pp. 72–73, aug 1937.

[70] M. Imada, A. Fujimori, and Y. Tokura, "Metal-insulator transitions," *Reviews of Modern Physics*, vol. 70, pp. 1039–1263, oct 1998.

[71] B. J. Kim, H. Jin, S. J. Moon, J.-Y. Kim, B.-G. Park, C. S. Leem, J. Yu, T. W. Noh, C. Kim, S.-J. Oh, J.-H. Park, V. Durairaj, G. Cao, and E. Rotenberg, "Novel $J_{eff} = 1/2$ Mott State Induced by Relativistic Spin-Orbit Coupling in Sr_2IrO_4," *Physical Review Letters*, vol. 101, p. 076402, aug 2008.

[72] I. Žutić, J. Fabian, and S. Das Sarma, "Spintronics: Fundamentals and applications," *Reviews of Modern Physics*, vol. 76, pp. 323–410, apr 2004.

[73] M. Z. Hasan and C. L. Kane, "Colloquium : Topological insulators," *Reviews of Modern Physics*, vol. 82, pp. 3045–3067, nov 2010.

[74] X.-L. Qi and S.-C. Zhang, "Topological insulators and superconductors," *Reviews of Modern Physics*, vol. 83, pp. 1057–1110, oct 2011.

[75] C. L. Kane and E. J. Mele, "Z_2 Topological Order and the Quantum Spin Hall Effect," *Physical Review Letters*, vol. 95, p. 146802, sep 2005.

[76] C. L. Kane and E. J. Mele, "Quantum Spin Hall Effect in Graphene," *Physical Review Letters*, vol. 95, p. 226801, nov 2005.

[77] L. Fu, C. L. Kane, and E. J. Mele, "Topological Insulators in Three Dimensions," *Physical review letters*, vol. 98, no. March, p. 106803, 2007.

[78] W. Witczak-Krempa, G. Chen, Y. B. Kim, and L. Balents, "Correlated Quantum Phenomena in the Strong Spin-Orbit Regime," *Annual Review of Condensed Matter Physics*, vol. 5, pp. 57–82, mar 2014.

[79] Y. Machida, S. Nakatsuji, S. Onoda, T. Tayama, and T. Sakakibara, "Time-reversal symmetry breaking and spontaneous Hall effect without magnetic dipole order," *Nature*, vol. 463, pp. 210–213, jan 2010.

[80] X. Wan, A. M. Turner, A. Vishwanath, and S. Y. Savrasov, "Topological semimetal and Fermi-arc surface states in the electronic structure of pyrochlore iridates," *Physical Review B*, vol. 83, p. 205101, may 2011.

[81] A. M. Turner, Y. Zhang, R. S. K. Mong, and A. Vishwanath, "Quantized response and topology of magnetic insulators with inversion symmetry," *Physical Review B*, vol. 85, p. 165120, apr 2012.

[82] W. Witczak-Krempa and Y. B. Kim, "Topological and magnetic phases of interacting electrons in the pyrochlore iridates," *Physical Review B*, vol. 85, p. 045124, jan 2012.

[83] A. A. Burkov and L. Balents, "Weyl Semimetal in a Topological Insulator Multilayer," *Physical Review Letters*, vol. 107, p. 127205, sep 2011.

[84] S. Raghu, X.-L. Qi, C. Honerkamp, and S.-C. Zhang, "Topological Mott Insulators," *Physical Review Letters*, vol. 100, pp. 1–4, apr 2008.

[85] D. Pesin and L. Balents, "Mott physics and band topology in materials with strong spin–orbit interaction," *Nature Physics*, vol. 6, pp. 376–381, mar 2010.

[86] G. Chen, R. Pereira, and L. Balents, "Exotic phases induced by strong spin-orbit coupling in ordered double perovskites," *Physical Review B*, vol. 82, p. 174440, nov 2010.

[87] J. G. Rau, E. K.-H. Lee, and H.-Y. Kee, "Spin-Orbit Physics Giving Rise to Novel Phases in Correlated Systems: Iridates and Related Materials," *Annual Review of Condensed Matter Physics*, vol. 7, pp. 195–221, mar 2016.

[88] L. F. Mattheiss, "Electronic structure of RuO_2, OsO_2, and IrO_2," *Physical Review B*, vol. 13, pp. 2433–2450, mar 1976.

[89] S. J. Moon, H. Jin, K. W. Kim, W. S. Choi, Y. S. Lee, J. Yu, G. Cao, A. Sumi, H. Funakubo, C. Bernhard, and T. W. Noh, "Dimensionality-Controlled Insulator-Metal Transition and Correlated Metallic State in 5d Transition Metal Oxides Srn+1IrnO3n+1 (n=1, 2, and inf)," *Physical Review Letters*, vol. 101, p. 226402, nov 2008.

[90] J. Bertinshaw, Y. Kim, G. Khaliullin, and B. Kim, "Square Lattice Iridates," *Annual Review of Condensed Matter Physics*, vol. 10, no. 1, pp. 315–336, 2019.

[91] S. J. Moon, H. Jin, W. S. Choi, J. S. Lee, S. S. A. Seo, J. Yu, G. Cao, T. W. Noh, and Y. S. Lee, "Temperature dependence of the electronic structure of the $J_{eff} = 1/2$ Mott insulator Sr_2IrO_4 studied by optical spectroscopy," *Physical Review B*, vol. 80, p. 195110, nov 2009.

[92] C. H. Sohn, M.-C. Lee, H. J. Park, K. J. Noh, H. K. Yoo, S. J. Moon, K. W. Kim, T. F. Qi, G. Cao, D.-Y. Cho, and T. W. Noh, "Orbital-dependent polaron formation in the relativistic Mott insulator Sr_2IrO_4," *Physical Review B*, vol. 90, p. 041105, jul 2014.

[93] D. Pröpper, A. N. Yaresko, M. Höppner, Y. Matiks, Y.-L. Mathis, T. Takayama, A. Matsumoto, H. Takagi, B. Keimer, and A. V. Boris, "Optical anisotropy of the J_{eff} = 1/2 Mott insulator Sr_2IrO_4," *Physical Review B*, vol. 94, p. 035158, jul 2016.

[94] P. A. Lee, N. Nagaosa, and X.-G. Wen, "Doping a Mott insulator: Physics of high-temperature superconductivity," *Reviews of Modern Physics*, vol. 78, pp. 17–85, jan 2006.

[95] J. Porras, J. Bertinshaw, H. Liu, G. Khaliullin, N. H. Sung, J.-W. W. Kim, S. Francoual, P. Steffens, G. Deng, M. M. Sala, A. Efimenko, A. Said, D. Casa, X. Huang, T. Gog, J.-W. W. Kim, B. Keimer, and B. J. Kim, "Pseudospin-lattice coupling in the spin-orbit Mott insulator Sr_2IrO_4," *Physical Review B*, vol. 99, p. 085125, feb 2019.

[96] L. Zhao, D. H. Torchinsky, H. Chu, V. Ivanov, R. Lifshitz, R. Flint, T. Qi, G. Cao, and D. Hsieh, "Evidence of an odd-parity hidden order in a spin–orbit coupled correlated iridate," *Nature Physics*, vol. 12, pp. 32–36, jan 2016.

[97] X. Chen, T. Hogan, D. Walkup, W. Zhou, M. Pokharel, M. Yao, W. Tian, T. Z. Ward, Y. Zhao, D. Parshall, C. Opeil, J. W. Lynn, V. Madhavan, and S. D. Wilson, "Influence of electron doping on the ground state of $(Sr_{1-x}La_x)_2IrO_4$," *Physical Review B*, vol. 92, p. 075125, aug 2015.

[98] J. P. Clancy, A. Lupascu, H. Gretarsson, Z. Islam, Y. F. Hu, D. Casa, C. S. Nelson, S. C. LaMarra, G. Cao, and Y.-J. Kim, "Dilute magnetism and spin-orbital percolation effects in $Sr_2Ir_{1-x}Rh_xO_4$," *Physical Review B*, vol. 89, p. 054409, feb 2014.

[99] L. J. P. Ament, M. van Veenendaal, T. P. Devereaux, J. P. Hill, and J. van den Brink, "Resonant inelastic x-ray scattering studies of elementary excitations," *Reviews of Modern Physics*, vol. 83, pp. 705–767, jun 2011.

[100] J. Kim, A. H. Said, D. Casa, M. H. Upton, T. Gog, M. Daghofer, G. Jackeli, J. van den Brink, G. Khaliullin, and B. J. Kim, "Large Spin-Wave Energy Gap in the Bilayer Iridate $Sr_3Ir_2O_7$: Evidence for Enhanced Dipolar Interactions Near the Mott Metal-Insulator Transition," *Physical Review Letters*, vol. 109, p. 157402, oct 2012.

[101] R. Coldea, S. M. Hayden, G. Aeppli, T. G. Perring, C. D. Frost, T. E. Mason, S.-W. Cheong, and Z. Fisk, "Spin waves and electronic interactions in La_2CuO_4," *Physical Review Letters*, vol. 86, pp. 5377–5380, jun 2001.

[102] J. Kim, M. Daghofer, A. H. Said, T. Gog, J. van den Brink, G. Khaliullin, and B. J. Kim, "Excitonic quasiparticles in a spin–orbit Mott insulator," *Nature Communications*, vol. 5, p. 4453, dec 2014.

[103] H. Gretarsson, N. H. Sung, J. Porras, J. Bertinshaw, C. Dietl, J. A. Bruin, A. F. Bangura, Y. K. Kim, R. Dinnebier, J. Kim, A. Al-Zein, M. Moretti Sala, M. Krisch, M. Le Tacon, B. Keimer, and B. J. Kim, "Persistent Paramagnons Deep in the Metallic Phase of $Sr_{2-x}La_xIrO_4$," *Physical Review Letters*, vol. 117, p. 107001, sep 2016.

[104] X. Liu, M. P. M. Dean, Z. Y. Meng, M. H. Upton, T. Qi, T. Gog, Y. Cao, J. Q. Lin, D. Meyers, H. Ding, G. Cao, and J. P. Hill, "Anisotropic softening of magnetic excitations in lightly electron-doped Sr_2IrO_4," *Physical Review B*, vol. 93, p. 241102, jun 2016.

[105] D. Pincini, J. G. Vale, C. Donnerer, A. de la Torre, E. C. Hunter, R. Perry, M. Moretti Sala, F. Baumberger, and D. F. McMorrow, "Anisotropic exchange and spin-wave damping in pure and electron-doped Sr_2IrO_4," *Physical Review B*, vol. 96, p. 075162, aug 2017.

[106] S. Fujiyama, H. Ohsumi, T. Komesu, J. Matsuno, B. J. Kim, M. Takata, T. Arima, and H. Takagi, "Two-Dimensional Heisenberg Behavior of J_{eff} =1/2 Isospins in the Paramagnetic State of the Spin-Orbital Mott Insulator Sr_2IrO_4," *Physical Review Letters*, vol. 108, p. 247212, jun 2012.

[107] J. G. Vale, S. Boseggia, H. C. Walker, R. Springell, Z. Feng, E. C. Hunter, R. S. Perry, D. Prabhakaran, A. T. Boothroyd, S. P. Collins, H. M. Rønnow, and D. F. McMorrow, "Importance of XY anisotropy in Sr_2IrO_4 revealed by magnetic critical scattering experiments," *Physical Review B*, vol. 92, p. 020406, jul 2015.

[108] Y. Gim, A. Sethi, Q. Zhao, J. F. Mitchell, G. Cao, and S. L. Cooper, "Isotropic and anisotropic regimes of the field-dependent spin dynamics in Sr_2IrO_4: Raman scattering studies," *Physical Review B*, vol. 93, p. 024405, jan 2016.

[109] H. Gretarsson, J. Sauceda, N. H. Sung, M. Höppner, M. Minola, B. J. Kim, B. Keimer, and M. Le Tacon, "Raman scattering study of vibrational and magnetic excitations in $Sr_{2-x}La_xIrO_4$," *Physical Review B*, vol. 96, p. 115138, sep 2017.

[110] H. Liu and G. Khaliullin, "Pseudo-Jahn-Teller Effect and Magnetoelastic Coupling in Spin-Orbit Mott Insulators," *Physical Review Letters*, vol. 122, p. 057203, feb 2019.

[111] G. Jackeli and G. Khaliullin, "Mott Insulators in the Strong Spin-Orbit Coupling Limit: From Heisenberg to a Quantum Compass and Kitaev Models," *Physical Review Letters*, vol. 102, p. 017205, jan 2009.

[112] J. B. Goodenough, *Magnetism and the Chemical Bond*. Interscience Publishers, 1963.

[113] M. P. Dean, Y. Cao, X. Liu, S. Wall, D. Zhu, R. Mankowsky, V. Thampy, X. M. Chen, J. G. Vale, D. Casa, J. Kim, A. H. Said, P. Juhas, R. Alonso-Mori, J. M. Glownia, A. Robert, J. Robinson, M. Sikorski, S. Song, M. Kozina, H. Lemke, L. Patthey, S. Owada, T. Katayama, M. Yabashi, Y. Tanaka, T. Togashi, J. Liu, C. Rayan Serrao, B. J. Kim, L. Huber, C. L. Chang, D. F. McMorrow, M. Forst, and J. P. Hill, "Ultrafast energy-and momentum-resolved dynamics of magnetic correlations in the photo-doped Mott insulator Sr_2IrO_4," *Nature Materials*, vol. 15, no. 6, pp. 601–605, 2016.

[114] G. Cao and P. Schlottmann, "The challenge of spin–orbit-tuned ground states in iridates: a key issues review," *Reports on Progress in Physics*, vol. 81, p. 042502, apr 2018.

[115] B. J. Kim, H. Ohsumi, T. Komesu, S. Sakai, T. Morita, H. Takagi, and T. Arima, "Phase-Sensitive Observation of a Spin-Orbital Mott State in Sr_2IrO_4," *Science*, vol. 323, pp. 1329–1332, mar 2009.

[116] F. Ye, S. Chi, B. C. Chakoumakos, J. A. Fernandez-Baca, T. Qi, and G. Cao, "Magnetic and crystal structures of Sr_2IrO_4: A neutron diffraction study," *Physical Review B*, vol. 87, p. 140406, apr 2013.

[117] Y. K. Kim, N. H. Sung, J. D. Denlinger, and B. J. Kim, "Observation of a d-wave gap in electron-doped Sr_2IrO_4," *Nature Physics*, vol. 12, pp. 37–41, jan 2016.

[118] Y. J. Yan, M. Q. Ren, H. C. Xu, B. P. Xie, R. Tao, H. Y. Choi, N. Lee, Y. J. Choi, T. Zhang, and D. L. Feng, "Electron-Doped Sr_2IrO_4: An Analogue of Hole-Doped Cuprate Superconductors Demonstrated by Scanning Tunneling Microscopy," *Physical Review X*, vol. 5, p. 041018, nov 2015.

[119] Y. K. Kim, O. Krupin, J. D. Denlinger, A. Bostwick, E. Rotenberg, Q. Zhao, J. F. Mitchell, J. W. Allen, and B. J. Kim, "Fermi arcs in a doped pseudospin-1/2 Heisenberg antiferromagnet," *Science*, vol. 345, pp. 187–190, jul 2014.

[120] A. de la Torre, S. McKeown Walker, F. Y. Bruno, S. Riccó, Z. Wang, I. Gutierrez Lezama, G. Scheerer, G. Giriat, D. Jaccard, C. Berthod, T. K. Kim, M. Hoesch, E. C. Hunter, R. S. Perry, A. Tamai, and F. Baumberger, "Collapse of the Mott Gap and Emergence of a Nodal Liquid in Lightly Doped Sr_2IrO_4," *Physical Review Letters*, vol. 115, p. 176402, oct 2015.

[121] I. Battisti, K. M. Bastiaans, V. Fedoseev, A. De La Torre, N. Iliopoulos, A. Tamai, E. C. Hunter, R. S. Perry, J. Zaanen, F. Baumberger, and M. P. Allan, "Universality of pseudogap and emergent order in lightly doped Mott insulators," *Nature Physics*, vol. 13, no. 1, pp. 21–25, 2017.

[122] F. Wang and T. Senthil, "Twisted Hubbard Model for Sr_2IrO_4: Magnetism and Possible High Temperature Superconductivity," *Physical Review Letters*, vol. 106, p. 136402, mar 2011.

[123] S. Sumita, T. Nomoto, and Y. Yanase, "Multipole Superconductivity in Nonsymmorphic Sr_2IrO_4," *Physical Review Letters*, vol. 119, no. 2, pp. 1–6, 2017.

[124] J. Jeong, Y. Sidis, A. Louat, V. Brouet, and P. Bourges, "Time-reversal symmetry breaking hidden order in $Sr_2(Ir,Rh)O_4$," *Nature Communications*, vol. 8, p. 15119, apr 2017.

[125] S. Di Matteo and M. R. Norman, "Magnetic ground state of Sr_2IrO_4 and implications for second-harmonic generation," *Physical Review B*, vol. 94, p. 075148, aug 2016.

[126] A. Kirilyuk, A. V. Kimel, and T. Rasing, "Ultrafast optical manipulation of magnetic order," *Reviews of Modern Physics*, vol. 82, pp. 2731–2784, sep 2010.

[127] A. M. Kalashnikova, A. V. Kimel, and R. V. Pisarev, "Ultrafast opto-magnetism," *Physics-Uspekhi*, vol. 58, pp. 969–980, oct 2015.

[128] S. Baierl, J. H. Mentink, M. Hohenleutner, L. Braun, T.-M. Do, C. Lange, A. Sell, M. Fiebig, G. Woltersdorf, T. Kampfrath, and R. Huber, "Terahertz-Driven Nonlinear Spin Response of Antiferromagnetic Nickel Oxide," *Physical Review Letters*, vol. 117, p. 197201, nov 2016.

[129] R. Mikhaylovskiy, E. Hendry, A. Secchi, J. Mentink, M. Eckstein, A. Wu, R. Pisarev, V. Kruglyak, M. Katsnelson, T. Rasing, and A. Kimel, "Ultrafast optical modification of exchange interactions in iron oxides," *Nature Communications*, vol. 6, p. 8190, dec 2015.

[130] J. H. Mentink, K. Balzer, and M. Eckstein, "Ultrafast and reversible control of the exchange interaction in Mott insulators," *Nature Communications*, vol. 6, p. 6708, nov 2015.

[131] A. V. Kimel, A. Kirilyuk, P. A. Usachev, R. V. Pisarev, A. M. Balbashov, and T. Rasing, "Ultrafast non-thermal control of magnetization by instantaneous photomagnetic pulses," *Nature*, vol. 435, no. 7042, pp. 655–657, 2005.

[132] R. V. Mikhaylovskiy, E. Hendry, and V. V. Kruglyak, "Ultrafast inverse Faraday effect in a paramagnetic terbium gallium garnet crystal," *Physical Review B*, vol. 86, p. 100405, sep 2012.

[133] T. Satoh, S.-J. Cho, R. Iida, T. Shimura, K. Kuroda, H. Ueda, Y. Ueda, B. A. Ivanov, F. Nori, and M. Fiebig, "Spin Oscillations in Antiferromagnetic NiO Triggered by Circularly Polarized Light," *Physical Review Letters*, vol. 105, p. 077402, aug 2010.

[134] C. Tzschaschel, K. Otani, R. Iida, T. Shimura, H. Ueda, S. Günther, M. Fiebig, and T. Satoh, "Ultrafast optical excitation of coherent magnons in antiferromagnetic NiO," *Physical Review B*, vol. 95, p. 174407, may 2017.

[135] A. M. Kalashnikova, A. V. Kimel, R. V. Pisarev, V. N. Gridnev, A. Kirilyuk, and T. Rasing, "Impulsive Generation of Coherent Magnons by Linearly Polarized Light in the Easy-Plane Antiferromagnet $FeBO_3$," *Physical Review Letters*, vol. 99, p. 167205, oct 2007.

[136] A. M. Kalashnikova, A. V. Kimel, R. V. Pisarev, V. N. Gridnev, P. A. Usachev, A. Kirilyuk, and T. Rasing, "Impulsive excitation of coherent magnons and phonons by subpicosecond laser pulses in the weak ferromagnet $FeBO_3$," *Physical Review B*, vol. 78, p. 104301, sep 2008.

[137] D. Afanasiev, I. Razdolski, K. M. Skibinsky, D. Bolotin, S. V. Yagupov, M. B. Strugatsky, A. Kirilyuk, T. Rasing, and A. V. Kimel, "Laser Excitation of Lattice-Driven Anharmonic Magnetization Dynamics in Dielectric $FeBO_3$," *Physical Review Letters*, vol. 112, p. 147403, apr 2014.

[138] A. V. Kimel, B. A. Ivanov, R. V. Pisarev, P. A. Usachev, A. Kirilyuk, and T. Rasing, "Inertia-driven spin switching in antiferromagnets," *Nature Physics*, vol. 5, pp. 727–731, oct 2009.

[139] P. Němec, M. Fiebig, T. Kampfrath, and A. V. Kimel, "Antiferromagnetic opto-spintronics," *Nature Physics*, vol. 14, pp. 229–241, mar 2018.

[140] Y. Wang, *Laser-Based Angle-Resolved Photoemission Spectroscopy of Topological Insulators*. PhD thesis, 2012.

[141] Y. Cao, X. Liu, W. Xu, W.-G. Yin, D. Meyers, J. Kim, D. Casa, M. H. Upton, T. Gog, T. Berlijn, G. Alvarez, S. Yuan, J. Terzic, J. M. Tranquada, J. P. Hill, G. Cao, R. M. Konik, and M. P. M. Dean, "Giant spin gap and magnon localization in the disordered Heisenberg antiferromagnet $Sr_2Ir_{1-x}Ru_xO_4$," *Physical Review B*, vol. 95, p. 121103, mar 2017.

[142] Y. Cao, Q. Wang, J. A. Waugh, T. J. Reber, H. Li, X. Zhou, S. Parham, S.-R. Park, N. C. Plumb, E. Rotenberg, A. Bostwick, J. D. Denlinger, T. Qi, M. A. Hermele, G. Cao, and D. S. Dessau, "Hallmarks of the Mott-metal crossover in the hole-doped pseudospin-1/2 Mott insulator Sr_2IrO_4," *Nature Communications*, vol. 7, p. 11367, sep 2016.

[143] D. Hsieh, F. Mahmood, D. H. Torchinsky, G. Cao, and N. Gedik, "Observation of a metal-to-insulator transition with both Mott-Hubbard and Slater characteristics in Sr_2IrO_4 from time-resolved photocarrier dynamics," *Physical Review B*, vol. 86, p. 035128, jul 2012.

[144] D. Afanasiev, A. Gatilova, D. J. Groenendijk, B. A. Ivanov, M. Gibert, S. Gariglio, J. Mentink, J. Li, N. Dasari, M. Eckstein, T. Rasing, A. D. Caviglia, and A. V. Kimel, "Ultrafast Spin Dynamics in Photodoped Spin-Orbit Mott Insulator Sr_2IrO_4," *Physical Review X*, vol. 9, p. 021020, apr 2019.

[145] U. F. P. Seifert and L. Balents, "Optical excitation of magnons in an easy-plane antiferromagnet: Application to Sr_2IrO_4," *Physical Review B*, vol. 100, p. 125161, sep 2019.

[146] H. Gretarsson, N. H. Sung, M. Höppner, B. J. Kim, B. Keimer, and M. Le Tacon, "Two-Magnon Raman Scattering and Pseudospin-Lattice Interactions in Sr_2IrO_4 and $Sr_3Ir_2O_7$," *Physical Review Letters*, vol. 116, p. 136401, mar 2016.

[147] A. Mook, J. Henk, and I. Mertig, "Magnon Hall effect and topology in kagome lattices: A theoretical investigation," *Physical Review B*, vol. 89, p. 134409, apr 2014.

[148] R. Chisnell, J. S. Helton, D. E. Freedman, D. K. Singh, R. I. Bewley, D. G. Nocera, and Y. S. Lee, "Topological Magnon Bands in a Kagome Lattice Ferromagnet," *Physical Review Letters*, vol. 115, p. 147201, sep 2015.

[149] M. M. Qazilbash, A. A. Schafgans, K. S. Burch, S. J. Yun, B. G. Chae, B. J. Kim, H. T. Kim, and D. N. Basov, "Electrodynamics of the vanadium oxides VO_2 and V_2O_3," *Physical Review B*, vol. 77, p. 115121, mar 2008.

[150] M. K. Stewart, D. Brownstead, S. Wang, K. G. West, J. G. Ramirez, M. M. Qazilbash, N. B. Perkins, I. K. Schuller, and D. N. Basov, "Insulator-to-metal transition and correlated metallic state of V_2O_3 investigated by optical spectroscopy," *Physical Review B - Condensed Matter and Materials Physics*, vol. 85, no. 20, pp. 1–7, 2012.

[151] M. K. Liu, B. Pardo, J. Zhang, M. M. Qazilbash, S. J. Yun, Z. Fei, J. H. Shin, H. T. Kim, D. N. Basov, and R. D. Averitt, "Photoinduced phase transitions by time-resolved far-infrared spectroscopy in V_2O_3," *Physical Review Letters*, vol. 107, no. 6, pp. 2–6, 2011.

[152] E. Abreu, S. Wang, J. G. Ramírez, M. Liu, J. Zhang, K. Geng, I. K. Schuller, and R. D. Averitt, "Dynamic conductivity scaling in photoexcited V_2O_3 thin films," *Physical Review B - Condensed Matter and Materials Physics*, vol. 92, no. 8, pp. 1–6, 2015.

[153] J. G. Ramírez, A. Sharoni, Y. Dubi, M. E. Gómez, and I. K. Schuller, "First-order reversal curve measurements of the metal-insulator transition in VO_2: Signatures of persistent metallic domains," *Physical Review B - Condensed Matter and Materials Physics*, vol. 79, no. 23, pp. 1–7, 2009.